EPSILON-NEAR-ZERO METAMATERIALS FOR OPTOELECTRONIC APPLICATIONS

Xin Li

A Thesis Submitted for the Degree of PhD
at the
University of St Andrews

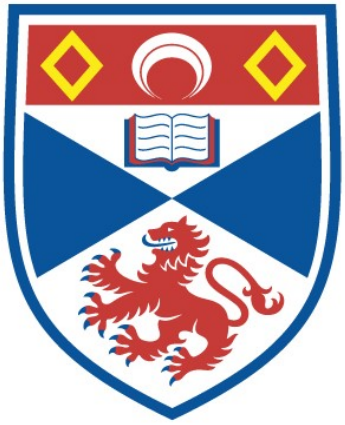

2019

Epsilon-Near-Zero Metamaterials for Optoelectronic Applications

Xin Li

This thesis is submitted in partial fulfilment for the degree of

Doctor of Philosophy

at the

University of St Andrews

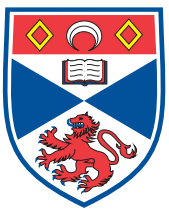

University
of
St Andrews

School of Physics and Astronomy

University of St Andrews

KY16 9SS

http://synthopt.wp.st-andrews.ac.uk/

2019-09-09

Abstract

My PhD is focused on the design, fabrication and optoelectronic applications of epsilon-near-zero (ENZ) metamaterials (MMs), which have vanishing real part of the permittivity and support fascinating optical effects, including light squeezing, sub-wavelength imaging, enhanced directive emission and enhanced non-resonant optical nonlinearity. Different approaches have been developed to realise ENZ media, such as tuning the modal dispersion in narrow plasmonic channels, exploiting the natural dispersion of transparent conductive oxides and creating composite structures with metals and dielectrics. As a platform with exotic physical properties, ENZ media also exhibit enormous potentials in combination with tunability and various nanofeatures in the photonic and plasmonic regimes.

This thesis demonstrates two approaches to achieve the ENZ condition. One method is to stack metal (Ag) and dielectric (SiO_2) layers periodically at sub-wavelength scales. The resulting material behaves as an effective medium with an average permittivity close to zero, and we show that this ENZ medium can enhance the emission of quantum dots. This approach generally requires nanofabrication techniques developed for flat and rigid substrates, for example, the electron beam evaporation, which are not always applicable to micro- and macroscopic devices with arbitrary shapes. To surpass these limitations, we design and experimentally demonstrate an optical free-standing and low-loss ENZ membrane in the visible range, by layering polymer (SU-8) and Ag nano-layers. Additionally, we propose a method to introduce both flexibility and electrical tunability into ENZ media by replacing the metal layer with a 2D material, graphene, in the multilayer model.

The other way to obtain an ENZ response is using natural materials which operate in proximity of their plasma frequency, typically here the indium tin oxide (ITO) at the near-infrared range. The ITO thin films are deposited using radio frequency magnetron sputtering, and their permittivities are manipulated via controlling fabrication parameters. We succeed in sweeping the zero-permittivity frequency of ITO media by controlling the gas recipe and deposition temperature during the sputtering process. To obtain specific optical responses, the ENZ ITO thin films are designed to be combined with different photonic features, including nanoantenna on microsphere and nanohelix, associated with a direct fabrication approach based on electron beam induced deposition (EBID).

Furthermore, this thesis extends the research range by realising the photonic trimming of quantum emitters via various metallic nanofeatures fabricated directly using EBID method. We believe that the interaction of ENZ MMs with EBID approach offers an opportunity to create hybrid ENZ platforms for optoelectronic applications.

Candidate's declarations:

I, Xin Li, do hereby certify that this thesis, submitted for the degree of PhD, which is approximately 50,000 words in length, has been written by me, and that it is the record of work carried out by me, or principally by myself in collaboration with others as acknowledged, and that it has not been submitted in any previous application for any degree.

I was admitted as a research student at the University of St Andrews in September 2015.

I received funding from an organisation or institution and have acknowledged the funder(s) in the full text of my thesis.

Date Signature of candidate

Supervisor's declaration:

I hereby certify that the candidate has fulfilled the conditions of the Resolution and Regulations appropriate for the degree of PhD in the University of St Andrews and that the candidate is qualified to submit this thesis in application for that degree.

Date Signature of supervisor

Permission for publication:

In submitting this thesis to the University of St Andrews we understand that we are giving permission for it to be made available for use in accordance with the regulations of the University Library for the time being in force, subject to any copyright vested in the work not being affected thereby. We also understand, unless exempt by an award of an embargo as requested below, that the title and the abstract will be published, and that a copy of the work may be made and supplied to any bona fide library or research worker, that this thesis will be electronically accessible for personal or research use and that the library has the right to migrate this thesis into new electronic forms as required to ensure continued access to the thesis.

I, Xin Li, confirm that my thesis does not contain any third-party material that requires copyright clearance.

The following is an agreed request by candidate and supervisor regarding the publication of this thesis:

PRINTED COPY
No embargo on print copy

ELECTRONIC COPY
No embargo on electronic copy

Date Signature of candidate

Date Signature of supervisor

Underpinning Research Data or Digital Outputs

Candidate's declarations:

I, Xin Li, understand that by declaring that I have original research data or digital outputs, I should make every effort in meeting the University's and research funders' requirements on the deposit and sharing of research data or research digital outputs.

Date Signature of candidate

Permission for publication of underpinning research data or digital outputs

We understand that for any original research data or digital outputs which are deposited, we are giving permission for them to be made available for use in accordance with the requirements of the University and research funders, for the time being in force.

We also understand that the title and the description will be published, and that the underpinning research data or digital outputs will be electronically accessible for use in accordance with the license specified at the point of deposit, unless exempt by award of an embargo as requested below.

The following is an agreed request by candidate and supervisor regarding the publication of underpinning research data or digital outputs:

No embargo on underpinning research data or digital outputs.

Date Signature of candidate

Date Signature of supervisor

Acknowledgements

The completion of my PhD work is attributed to the help and encouragement of many people, and thus here I would like to express my gratitude to all of them sincerely.

My biggest thanks go first and foremost to Dr Andrea Di Falco, my supervisor, for giving me the excellent opportunity to study at St Andrews. I do appreciate his consistent encouragement, expert guidance and meaningful inspirations, which help me understand my research better and produce this thesis. Without his support and constant feedback, my PhD would have never completed.

Next, I would like to thank Prof. Robert Thomson and Dr Liam O'Faolain for agreeing to be my examiners.

I greatly appreciate the support received from the members of the Synthetic Optics Group: Usenobong Akpan, Danielle Fraser, Sophie Varney, Yunli Qiu and Xiangkun Kong. Particularly, Adam Fleming, James Burch, Alasdair Fikouras and I started the PhD at the same time, and hopefully, we would finish our work at the same period. Special thanks go to Blair Kirkpatrick, Monika Pietrzyk and Aline Heyerick for training me various pieces of equipment in both cleanrooms and laboratories. I would also like to thank the members of the Nanophotonics Group in St Andrews, particularly Changyu Hu and Alexandros Liles for helping me understand the procedure of electron-beam lithography, and Dr Sebastian Schulz, who has shown me how to run FDTD simulations.

In the School of Physics and Astronomy more generally, I would like to extend my gratitude to Callum Smith, Chris Watson and Graeme Beaton, who have kept the cleanroom facilities working perfectly and assisted the modification of laboratory apparatus when necessary. Besides, I should particularly thank Scott Johnston, the Stores Manager of our school, for his great effort on ordering equipment and consumables. My faithful appreciation also goes to Lesley Aitken, Linda Cousins and Dimali Vithanage, the Secretaries of School, as well as Poppy Nicholson, the Finance Assistant,

for their help with arranging my postgraduate affairs smoothly.

Additionally, I am very thankful to some members from the School of Chemistry: David Miller, Aaron Naden and Richard Bailey, who have helped me about the fabrication and characterisation using focused ion beam system and atomic force microscope. I should also thank Dr Emanuele Pelucchi from Tyndall National Institute, University College Cork, Cork, Ireland, for providing me with the pyramid samples which are essential for the research of photonic trimming of quantum emitters.

Last but not least, I would like to express my sincere thanks to my parents, who supported me in all my pursuits and motivated me to confront any obstacles on my way to success. Notably, the deepest thanks of all must go to Jie, my girlfriend, for her accompanying and supporting without a word of complaint all the time.

Collaboration Statement

I would like to acknowledge Dr Zhang-Kai Zhou and Dr Ying Yu from the School of Physics and Engineering, Sun Yat-sen University, Guangzhou, China, for their collaboration with the work of photonic trimming of quantum emitters via direct fabrication of metallic nanofeatures. Their teams provided me with the samples of nanowires and micropillars that hosted quantum dots and performed emission analysis experiments. Their help was precious when I visited Guangzhou.

Acknowledgement of funding

This work was supported by the China Scholarship Council and the University of St Andrews (School of Physics and Astronomy).

Research Data access statement

Research data underpinning this thesis are available at https://doi.org/10.17630/c87e32ae-936d-43ba-ac9d-6877197e8342.

To Jie: Thanks to you, I never lost hope and went all the way through.

Publications and Conferences

Publications

- **Li, X.**, Su, R.L., Zhou, Z.K., Yu, Y. and Di Falco, A. "Photonic trimming of quantum emitters via direct fabrication of metallic nanofeatures." APL Photonics, 3(7), 071301(2018).
- Rizza, C., **Li, X.**, Di Falco, A., Palange, E., Marini, A. and Ciattoni, A. "Enhanced asymmetric transmission in hyperbolic epsilon-near-zero slabs." Journal of Optics, 20(8), 085001(2018).
- **Li, X.**, Rizza, C., Schulz, S. A., Ciattoni, A. and Di Falco, A. "Conformable optical coatings with epsilon near zero response." APL Photonics, 4(5), 056107(2019).

Conferences

- Pietrzyk, M., **Li, X.**, Rishad, K., Faccio, D., and Di Falco, A. "Epsilon Near Zero Metamaterials for Nonlinear Optics Applications." *ADVANCED MATERIALS CONFERENCE*, 2016. Poster, presented by Pietrzyk, M.
- **Li, X.**, Pietrzyk, M., Rizza, C., Scalora, M., Ciattoni, A., and Di Falco, A. "One-Dimensional Chirality: Strong Optical Activity in Epsilon-Near-Zero Metamaterials." *The 12th International Symposium on Photonic and Electromagnetic Crystal Structures (PECS-XII)*, 2016. Poster, presented by **Li, X.**.
- **Li, X.**, Pietrzyk, M., Faccio, D., Rizza, C., Ciattoni, A. and Di Falco, A. "Linear and nonlinear optical behavior of epsilon near zero metamaterials: opportunities and challenges." *Proc. SPIE 10111, Quantum Sensing and Nano Electronics and Photonics XIV*, Vol. 10111, p. 101111O, 2017. Talk, presented by Di Falco, A.

- **Li, X.**, Pietrzyk, M., Rizza, C., Scalora, M., Ciattoni, A., and Di Falco, A. "One-Dimensional Chirality: Strong Optical Activity in Epsilon-Near-Zero Metamaterials." *SU2P 8th Annual Symposium*, 2017. Poster, presented by **Li, X.**.

- **Li, X.**, Zhou, Z.K., Yu, Y., Gather, M. and Di Falco, A. "Nanophotonic enhanced quantum emitters." *Proc. SPIE 10359, Quantum Nanophotonics*, Vol. 10359, p. 103590A, 2017. Talk, presented by Di Falco, A.

- **Li, X.**, Rizza, C., Ciattoni, A., Faccio, D., and Di Falco, A. "Photonic Applications of Epsilon near Zero Metamaterials." *Progress in Electromagnetics Research Symposium (PIERS) 2018*, 2018. Talk, presented by Di Falco, A.

- Rizza, C., **Li, X.**, Di Falco, A., Palange, E., Marini, A. and Ciattoni, A. "Optical chiral effects in ENZ ultrathin slabs." *META 2018 , the 9th International Conference on Metamaterials, Photonic Crystals and Plasmonics*, 2018. Talk, presented by Rizza, C.

- **Li, X.**, Zhou, Z.K., Yu, Y., and Di Falco, A. "Nanoplasmonic enhancement of semiconductor quantum emitters." *The 18th IEEE International Conference on Nanotechnology*, 2018. Talk, presented by **Li, X.**.

- Rizza, C., **Li, X.**, Di Falco, A., Palange, E., Marini, A. and Ciattoni, A. "Diode-like asymmetric transmission in hyperbolic epsilon-near-zero media." *Nanophotonics and Micro/Nano Optics International Conference 2018*, 2018. Talk, presented by Rizza, C.

Contents

Chapter 1

Introduction

This chapter briefly introduces the main content of this thesis, addressing first the historical development of metamaterials (MMs) and epsilon-near-zero (ENZ) MMs, and types of ENZ structures, then the typical light propagation with no spatial dispersion through ENZ media. This part also shows specific applications of ENZ structures, such as non-diffraction imaging, enhanced directive emission and nonlocal enhancement in nonlinear optics. The final section outlines the structure of this thesis.

1.1 A historical overview of MMs and ENZ MMs

Photonic MMs are artificial materials typically consisting of sub-wavelength repeating patterns and exhibiting peculiar properties[1, 2]. The prefix "meta" means "beyond" in Greek[3], and it indicates that MMs exhibit physical properties which not present in natural materials. These unusual properties result from the homogenisation of component structures, which is also beyond the simple sum of every component. As the size of the component atoms is much smaller than the wavelength of probing electromagnetic wave, MMs exhibit macroscopic properties that are not shown in constituent materials. Particularly, in the visible and near-infrared (NIR) regime, the scale of unit structures in MMs goes down to tens of nanometres or less. Because of the shared scales, the field of MMs has involved in parallel with that of plasmonics[4].

The study of plasmonics and MMs first began thousands of years ago. For example, the Lycurgus Cup[5, 6] constructed with ruby glass in the 4th century shows different colours when light shines from inside and outside the cup. This phenomenon is caused by the nanoscale (5 - 60 nm) gold (Au) and silver (Ag) particles embedded in the ruby glass. The nanoparticles scatter light with high sensitivity to their sizes and exhibit dichroic characteristic due to the plasmon resonance[7]. Hence, dichroic ruby glass can be considered the first optical metamaterial (MM). Even if the scattering

mechanics of the Lycurgus Cup were not fully understood a thousand years ago, the manufacturing technique has been passed on and has motivated research into plasmonics[8] and MMs[6].

Classical electrodynamics shows that the electromagnetic properties of materials depend on their permittivity (ϵ) and permeability (μ). The refractive index (n) of a material is defined as

$$n = \sqrt{\epsilon\mu} \tag{1.1}$$

As ϵ and μ are determined by microscopic properties and distributions of atoms inside materials, the development of MMs permits to extend the optical properties beyond those enabled by these atomic configurations.

The theoretical research into plasmonic materials started from the study of negative refraction by Mandelshtam in the 1940s[9]. In 1968, an important step was made by Veselago who presented a theoretical work on the negative-index materials (NIMs) (also known as left-handed materials)[10] whose ϵ and μ are all negative. He predicted that negative refraction which is never seen in nature would exist inside this kind of material. However, the real investigation and design of NIMs did not begin in earliest until about 30 years later. In 1996, Pendry et al. proposed a structure that consisted of periodic aluminium (Al) microwires that could exhibit a negative ϵ at GHz range[11]. Three years later, Pendry et al. also proposed that a periodic split rings array made of nonmagnetic material could exhibit a negative μ[12]. Eventually, in 2000 and 2001, Smith et al. demonstrated the experimental realisation of the first one-dimensional (1D)[13] and two-dimensional (2D)[14] NIMs using a structure combining split ring resonators with wires. These studies of NIMs provided the possibility to modify the ϵ and μ of materials artificially and motivated the development of other MMs.

As mentioned above, the structural units of MMs usually have a size which is far smaller than the working wavelength. This is because the MMs typically have inhomogeneous structure and complex boundary conditions, and many physical properties of them (e.g. ϵ and μ) cannot be calculated precisely and easily. A common way to approximate the effective electromagnetic properties of these media in theory is using the effective medium theory (EMT)[15, 16]. The EMT can describe the macroscopic properties of composite materials (e.g. MMs) by averaging the related physical parameters of the composite materials, with the request of limiting the size of the structural units within the sub-wavelength scale. Therefore, here we use a common approach to design and characterise MMs using effective permittivity (ϵ_{eff}) and permeability (μ_{eff}) based on EMT and this greatly simplified the study of electromagnetic MMs (Figure 1.1).

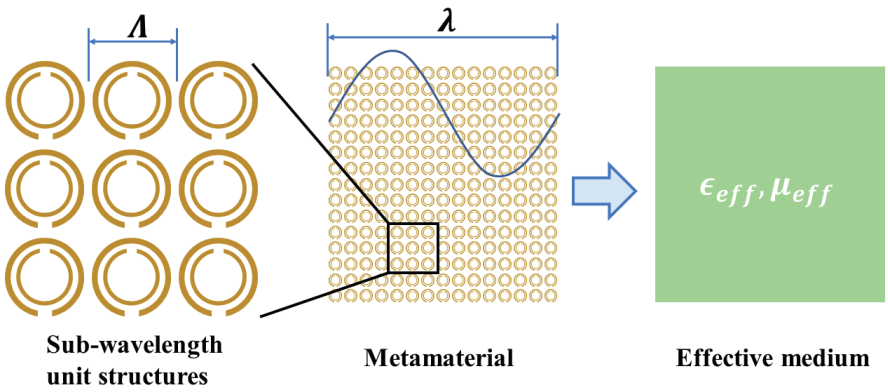

Figure 1.1: Diagram of a MM made of periodic sub-wavelength unit structures and the corresponding effective medium. To satisfy the demand of EMT, the period (Λ) of the structure is far less than the wavelength (λ) of the electromagnetic wave.

Due to the ability of modifying effective ϵ and μ, MMs now show dramatic potential in the field of high-directivity radiating[17], electromagnetic cloaking[2, 18], perfect absorbing[19] and quantum applications[20].

As special MMs, zero-index materials (ZIMs) show vanishing refractive index at specific frequencies and has attracted much attention in many research fields, such as emission controlling[21] and imaging[17]. In the parameter space of ϵ and μ (Figure 1.2), ZIMs locate at horizontal and vertical axes and the origin of coordinates. The horizontal axis represents ZIMs with μ closing to zero, i.e. mu-near-zero (MNZ) MMs. The vertical axis stands for ZIMs with ϵ closing to zero, i.e. ENZ MMs. The origin of coordinates means ZIMs with both μ and ϵ all closing to zero, namely double-zero ZIMs.

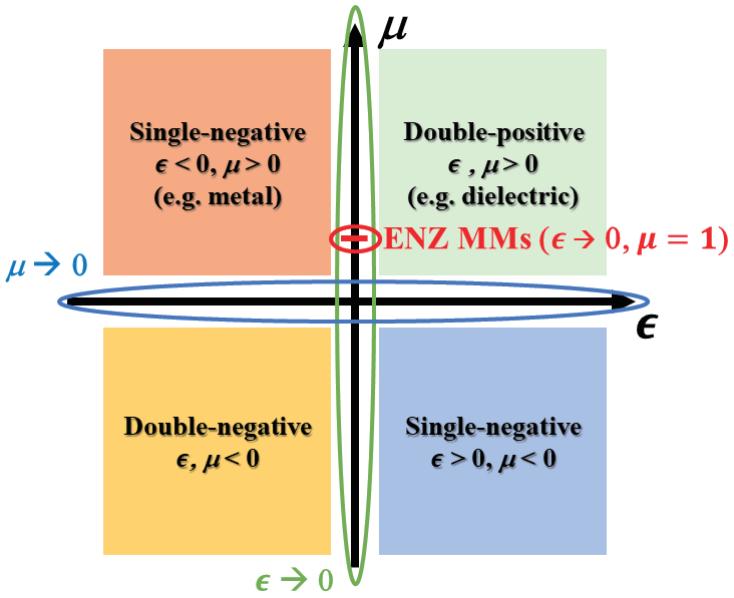

Figure 1.2: Parameter space of μ vs ϵ, and the location of ENZ MMs.

The ϵ of natural substances can be both positive (e.g., dielectric material) or negative (e.g., most metal materials). However, the μ value is usually equal to 1, due to the weak magnetic repose of most natural materials at a high-frequency range. The assumption $\mu = 1$ will be used in this thesis as there are no ferromagnetic materials or magnetic structure used in this work, and this ENZ MM is indicated in Figure 1.2. Therefore, Equation 1.1 can be simplified as

$$n = \sqrt{\epsilon} \tag{1.2}$$

Additionally, complicated structures and processes are always needed to realise double-zero ZIMs, i.e. reaching zero μ and ϵ at same time[22]. However, it is relatively easy to obtain zero-permittivity structure using non-magnetic materials[23]. Therefore, the zero-index condition can be obtained at ENZ media, according to Equation 1.2.

Inside ENZ MMs, due to ϵ approaching zero, the refractive index, effective displacement field and the wave vector are all close to zero, thus the wavelength diverges and no diffraction occurs. The ENZ MMs can be classified in two types: anisotropic epsilon-near-zero (AENZ) MMs and isotropic epsilon-near-zero (IENZ) MMs. AENZ condition is realised based on EMT, usually by averaging the positive and negative permittivity contributed by different sub-wavelength components, typically dielectrics and metals[24, 25]. Under this condition, one component of the effective permittivity tensor approaches zero while the others do not. The AENZ property make it possible to manipulate

the transmission in specific directions. The other type ENZ condition, i.e. IENZ, is achieved by transparent conductive oxides (TCOs)[26], such as Al-doped zinc oxide (AZO), indium tin oxide (ITO) and gallium zinc oxide (GZO). Their permittivity can be tuned by modifying their plasma frequency, and typically approaches zero at NIR range. In addition, TCOs have small optical losses and electric tunability, and thus displays potentials to be used in wider-range optoelectronic devices.

These peculiar properties have attracted significant attention in the last two decades. In 2002, Enoch et al. demonstrated a method for tuning the emission of an antenna embedded in a multilayer metal-grid material[21]. By changing the parameters of unit structures, the effective ϵ was modified, and the directive emission was realised in the ENZ condition. In 2006, Silveirinha et al. presented a theoretical work on the tunneling effect in ENZ MMs[27]. The electromagnetic waves were "squeezed" through arbitrary shaped ENZ channels with almost no phase variation. This effect was verified experimentally by Liu et al.[28] and Edwards et al.[29] in 2008. Based on this, the perfect bending waveguides were designed by Luo and Lai et al.[30, 31] and realised experimentally by Ma et al.[32]. Further research done by Luo et al. showed that AENZ MMs had the capability of controlling electromagnetic flux conveniently and efficiently[33].

In recent years, ENZ MMs have shown important and interesting physical properties, and enormous potential in applications such as sub-wavelength imaging[34], optical sensing[35] and asymmetric transmission[36]. However, the study of ENZ MMs is still a basic research, and further theoretical research and experimental design need to be investigated.

1.2 Light propagation in ENZ media

Media with vanishing refractive index show unique dielectric responses and promise the possibility of light manipulation. A simulation work has predicted that a time varying source in a matched zero-index material (ZIM) exhibits a constant spatial distribution within the medium[37], and the 1D distribution of the electric field is sketched in Figure 1.3 (a).

The region marked by two vertical dashed black lines shows the position of free space or a ZIM. The other parts outside the two boundaries are filled with lossy media. A line source locates at the middle of the medium region and emits light waves towards both the left and right boundaries. The dashed blue line in Figure 1.3 (a) shows a steady-state oscillation of the light wave inside the free space and a fast decay in the lossy media. The solid red line presents the distribution of electric field of the light inside the ZIM at a moment when the light just propagate to the inflection points, not arriving the boundaries of the medium. The electric field in the ZIM is constant spatially, but

varying in time, as source is varying with time. After the light travel through the whole medium, the electrical field will exhibit a fast decay similar to the blue dashed line. This effect is due to the zero phase variation and diverging wavelength inside the ZIM, and there is no phase difference between two points in the ZIM.

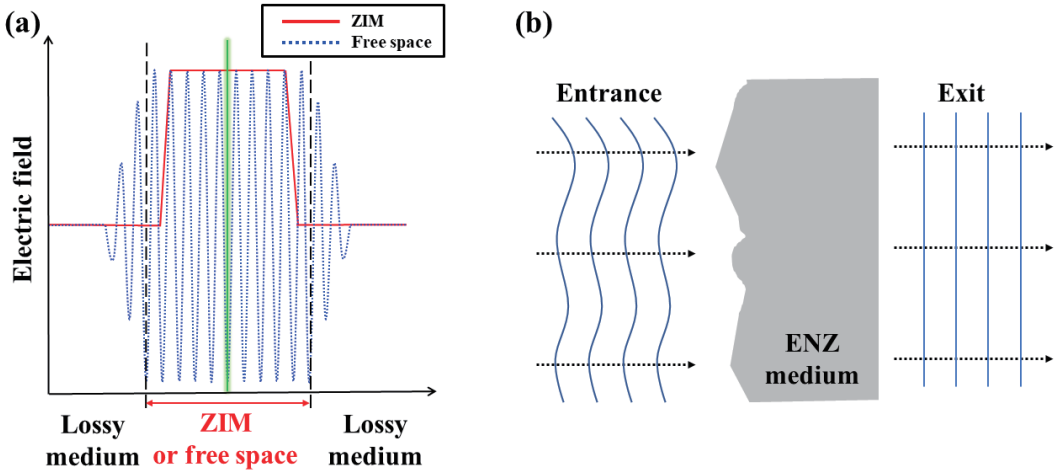

Figure 1.3: Diagrams of light propagating through ZIM (n≈0) and ENZ medium. (a) The light come from a line source (green vertical line) exhibit constant electric field in the ZIM (red solid line) while shows steady-state electric field in free space (blue dashed line)[37]. The two vertical dashed black lines are the boundaries of the ZIM or free space. The left and right regions beside the medium region are filled with lossy media. (b) An ENZ medium manipulate the shape of a wavefront from arbitrary to the same as exit surface[38].

As discussed above, the zero-index condition can be approached in ENZ MMs[39]. Another simulation work has predicted that the phase variation also approaches zero or effectively very small inside a ENZ slab[38], and this effect opens the door towards the direct modification of wavefront. As Figure 1.3 (b) illustrated, a electromagnetic wave with arbitrary shaped wavefront propagates through an ENZ medium from entrance side, and the phase distribution at the exit side is conformal with the shape of the exit surface. Therefore, by designing the exit surface of ENZ media, the impinging wave can be manipulated and the phase distribution can be transformed into a desired shape. The challenge of this design is the coupling of the input wave to the ENZ medium, which needs more investigation.

Due to the small permittivity, ENZ MMs also have negligible spatial dispersion. Spatial dispersion is defined here as the dependence between permittivity and wave vector or wavelength in a medium. Therefore, the wavelength of electromagnetic waves will be stretched inside ENZ media[34]. These effects in AENZ slab provides the possibility to realise far-field imaging without diffraction limits.

Figure 1.4 sketches a curved metal-dielectric multilayer structure which is designed to exhibit zero effective permittivity in the directions perpendicular to the stacking direction. The optical waves from two point sources separated in sub-wavelength scale will propagate through the structure nondiffractively. The output light spots are exactly copied from the sources, and with the help of symmetric curvature, the magnification beyond diffraction limits can be achieved.

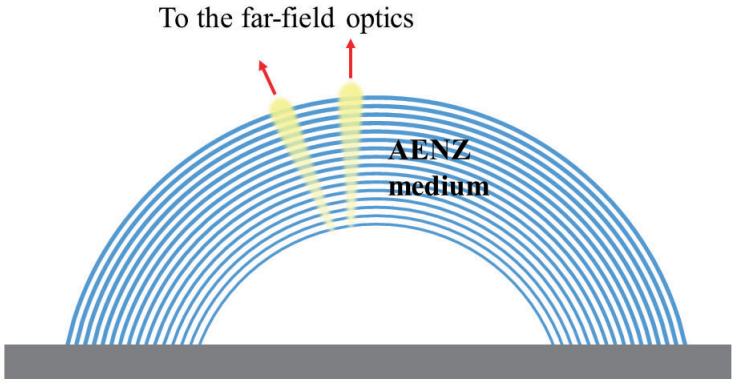

Figure 1.4: 2D diagram of a curved AENZ medium whose inner layer to which two light sources are attaching that separated in sub-wavelength scale[34]. After propagating through the ENZ medium, the two output light spots are separated with a distance large enough to break the diffraction limit.

Additionally, ENZ media can support electromagnetic chirality which usually only shown in three-dimensional (3D)[40] or 2D[41] complex chiral structures. Chirality has drawn a great deal of attention[42, 43] in the field of molecular biology and life science, associated with optics, crystallography and particle physics. Generally, the chiral response, i.e. the asymmetric transmission, can be achieved by breaking either the Lorentz reciprocity[44] or the spatial inversion symmetry[42]. With the help of considerable the magneto-electric coupling, the ENZ structure shows dramatical enhancement of the optical chirality[36].

1.3 Applications of ENZ medium in the emission enhancement

Due to the near-zero effective permittivity, ENZ MMs have vanishingly small refractive indices. In this situation, most media in nature, even the air, are optically "denser" than ENZ media. Therefore, total reflection will occur when light propagates from a ENZ slab to other "denser" material. Considering the interface between a ENZ slab and air, when a light source (e.g. dipole) is placed on top of or immersed inside the ENZ medium, the radiation intensity in the air side can be enhanced dramatically because air is the "denser" material in this model[45].

This effect has been used to enhance the emission of antennas. For example, the molecular fluorescence can be boosted inside a ENZ waveguide and the enhancement is independent of the location of the emission source[46]. In another model, the emission of plasmonic antennas can be enhanced dramatically by a ENZ substrate[47].

Additionally, due to the lack of spatial dispersion, the emission of point source embedded inside ENZ slabs can be modified into a plane wave with enhanced directivity and efficiency[48].

These characteristics make it possible to realise the superradiance, beam steering and the manipulation of quantum emission.

1.4 Enhanced optical nonlinearity at ENZ range

Nonlinear response of optical materials draws a great deal of attention and generate fascinating applications, such as optical harmonic generation[49], transient coherent effect[50] and self-focusing of optical beams[51]. Additionally, these nonlinear effects can be supported at ENZ MMs.

The mechanisms of nonlinear optics can be classified as resonant or nonresonant, according to the relationship between the frequency of light and the particular electronic resonances of the material[52, 53]. Nonresonant nonlinearities are generally weak and require high light intensities and/or very long light-matter interaction time and length[54]. On contrast, resonant nonlinearities can be several orders of magnitude stronger, but this comes at the cost of introducing detrimental and unavoidable losses[55, 56].

Under the ENZ condition, due to the linear permittivity approaching zero, the linear refractive index is relatively small compared to the nonlinear susceptibility, hence the nonlinear response can be obtained with low-power probing and low losses[57]. In the interface between vacuum and ENZ medium, the nonresonant enhancement of the typical electric field can combine the ENZ effect with nonlinearity[58], which leads to peculiar nonlinear effects, such as transmissivity directional hysteresis[59] and enhancement of second and third harmonic generation[60, 61].

1.5 Structure of the thesis

This thesis starts with an introduction of the historical development and particular properties of ENZ MMs. Different ENZ platforms have been introduced for typical applications, such as light squeezing, sub-wavelength imaging, enhanced directive emission and enhanced nonresonant optical nonlinearity. In the following chapters, I focus on the ENZ models related to my works.

Chapter 2 discusses the background theory of light-matter interaction in ENZ regime, which related to the works in the following chapters. The first section is about the realisation of ENZ structure, including mainly two models, i.e. the metal/dielectric multilayer structure according to EMT and TCOs which operate near their plasma frequency based on Drude-Sommerfeld model. Then, light modification, asymmetry transmission and enhanced directive emission based on ENZ media will be presented, followed by a summary.

Chapter 3 demonstrates the fabrication and characterisation of Ag/silicon dioxide (SiO_2) multilayer ENZ structure. The Ag and SiO_2 nanolayers are deposited using an electron beam (e-beam) evaporation technique, which is addressed in detail. To optically characterise thin films, we present a retrieval method based on Fresnel's equations. Finally, the investigation of the ENZ platform for enhancing the emission of quantum dots (QDs) is presented, before the summary.

Chapter 4 details the way to introduce flexibility into ENZ membranes using a sacrificial-layer assisted method. First, the complete fabrication process of the multilayer metal/polymer structure is demonstrated in detail. Next, we test optical properties of the material after large mechanical deformations and also show the capability of this membrane to conform on targets with irregular surfaces. The flexibility promises the feasibility of ENZ structures in superlens and other shape sensitive applications. In the end, the conclusion is presented.

Chapter 5 outlines the design of graphene-based ENZ structure which provides the possibility to introduce both flexibility and electrical tunability into multilayer graphene/dielectric structures. The fabrication of graphene using chemical vapour deposition (CVD) method is first demonstrated, followed by the characterisation of graphene using optical, electrical and physical means. Then we show the fabrication of flexible graphene/dielectric membrane and the initial result of the electrical tuning at NIR range.

Chapter 6 concerns about the fabrication of ITO thin films using radio frequency (RF) magnetron sputtering approach. First, the deposition and characterisation of ITO films with tunable permittivity via modifying the deposition parameters are presented. Then, we propose that the ENZ ITO material can be combined with different nanofeatures, fabricated directly using electron beam induced deposition (EBID) method, to realise typical optical responses. Additionally, the other applications based on the EBID technique are also addressed.

The final chapter summarises the main work in this thesis and discusses further perspectives.

Chapter 2

Background and theory

This chapter gives a general review of the background and fundamental physics of ENZ MMs. The first section outlines the approaches of realising ENZ structures, both in anisotropic and homogeneous configurations. Next, the optical wave modification in ENZ regime is discussed, particularly the phase variation minimisation and wavefront engineering. After that, the non-local enhancement of asymmetry transmission in ENZ regime is addressed in detail. This section is my original work with collaborators. The next section briefly discuss the emission enhancement related to ENZ MMs. The final part summarises the optical properties and further applications of ENZ membrane included in this thesis.

2.1 Realisation of ENZ MMs

The ENZ condition can be approached using different methods, sketched in Figure 2.1. One way is according to EMT via stacking materials with positive (e.g. dielectric) and negative (e.g. metal) ϵ alternatively in the sub-wavelength regime (Figure 2.1 (a))[25]. This method is able to create uniaxial AENZ MMs. The perpendicular (to the stacking direction) components of the effective ϵ can be tuned into zero by simply modifying the thicknesses of unit layers, while the parallel component usually retains the value bigger than 1. This approach can be also used in 2D model by patterning periodic structures consisting of complementary split ring resonators[28] or nanorods[24]. As shown in Figure 2.1 (b), the metal nanorod array is embedded in dielectric medium (such as aluminium oxide (Al_2O_3)) or surrounded by air and this structure can be designed to exhibit a vanishing effective permittivity at a specific wavelength.

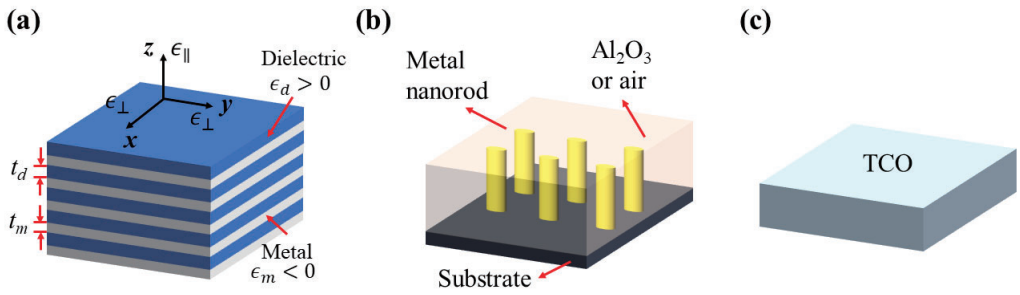

Figure 2.1: Diagram of three types of ENZ structures. (a) a periodic structure consisted of two unit layers: metal with thickness t_m and permittivity ϵ_m; dielectric with thickness t_d and permittivity ϵ_d. $\epsilon_\perp$ and $\epsilon_\parallel$ are the perpendicular and parallel components of the effective permittivity of the structure. (b) a 2D ENZ structure consisted with metal nanorods embedded in dielectric environment. (c) TCOs slab whose permittivity can reach zero at near-infrared ranges.

Another method of obtaining ENZ response is based on the materials operated closed to their plasma frequency, such as TCOs (Figure 2.1 (c))[62]. Plasma frequency is an intrinsic property of conducting materials, such as metals, semiconductors and TCOs, and determines the permittivity of these materials according to Drude-Sommerfeld model[63]. When these media interact with electromagnetic waves, free carriers (e.g. electrons) inside them oscillate with a frequency which is related to the density, charge and effective mass of carriers. Additionally, the frequency of this oscillation is independent of the wavelength of input waves. This frequency is so called plasma frequency. Typically, if the operating frequency is lower than the plasma frequency, the medium shows a negative permittivity; if the operating frequency is higher than the plasma frequency, the medium shows a positive permittivity. This effect promises the ENZ response of TCOs when they are operated near their plasma frequency. Specifically, here we use a special TCOs, i.e. ITO, and its permittivity approaches zero at NIR ranges. This material will be discussed in detail later in this chapter.

In this thesis, I focus on the two approaches shown in Figure 2.1 (a) and (c), i.e. the anisotropic metal/dielectric multilayer structure and homogeneous (isotropic) ENZ medium (e.g. ITO).

2.1.1 Realisation of AENZ MMs

In the optical regime, most metals show negative dielectric response because the optical frequency (ω) is much higher than their plasma angular frequency (ω_p), and their dielectric permittivity (ϵ_m) can be described by the Drude-Sommerfeld model[63] as

$$\epsilon_m(\omega) = \epsilon_b - \frac{\omega_p^2}{\omega^2 + i\gamma\omega} \tag{2.1}$$

where ϵ_b represents the background permittivity, γ is the collision frequency which is typically essential and related to optical losses.

Inside these metal materials, when $\epsilon_m < 0$, the internal free carriers move in the opposite direction to the external electric field. On the contrary, dielectric materials have positive permittivities ($\epsilon_d > 0$). To obtain the material with tunable permittivity, we can consider the simplest model, i.e. the 1D periodic structure consisting of repeating metal-dielectric bilayers (Figure 2.1 (a)). Each metal layer has a thickness of t_m and permittivity of ϵ_m, and each dielectric layer has a thickness of t_d and permittivity of ϵ_d. Using this structure, we can realise the capability to modify the effective ϵ and also achieve the ENZ condition.

In sub-wavelength situation, the multilayer structure shows anisotropic effective permittivity (ϵ_{eff}), expressed in the tensor form of

$$\epsilon_{eff} = \epsilon_0 \begin{pmatrix} \epsilon_\perp & 0 & 0 \\ 0 & \epsilon_\perp & 0 \\ 0 & 0 & \epsilon_\parallel \end{pmatrix} \tag{2.2}$$

where ϵ_0 is the permittivity of vacuum, $\epsilon_\perp$ and $\epsilon_\parallel$ are the relative permittivity components in the directions perpendicular and parallel to the principal axis (stacking direction), respectively.

If t_m and t_d are at sub-wavelength range and the period number (N) is big enough (e.g. $N \geq 5$)[64], the components of effective permittivity can be obtained by averaging the permittivity of unit layers, based on EMT[64, 65] and stated as

$$\epsilon_\perp = f\epsilon_m + (1-f)\epsilon_d \tag{2.3}$$

$$\frac{1}{\epsilon_\parallel} = f\frac{1}{\epsilon_m} + (1-f)\frac{1}{\epsilon_d} \tag{2.4}$$

where f is the filling fraction of the metal layer, defined as

$$f = \frac{t_m}{t_m + t_d} \tag{2.5}$$

By modify f for specific metal and dielectric materials, we can design the material with effective $\epsilon_\perp$ approaching zero at desired wavelengths and keep $\epsilon_\parallel$ bigger than 1. Furthermore, this method is

not limited to the two-component structure. For three or more unit layers, Equations 2.3 and 2.4 are expanded and shown as

$$\epsilon_{\perp} = \sum_{j}^{N_c} f_j \epsilon_j, \quad j = 1, 2, 3, ..., N_c \tag{2.6}$$

$$\frac{1}{\epsilon_{\parallel}} = \sum_{j}^{N_c} f_j \frac{1}{\epsilon_j}, \quad j = 1, 2, 3, ..., N_c \tag{2.7}$$

where f_j and ϵ_j are the filling fraction and permittivity of unit layer j. f_j satisfies $\sum_j^{N_c} f_j = 1$.

Here we consider a example of Ag/SiO_2 multilayer structure to verify the accuracy of EMT (Figure 2.2). The Ag unit layer is 10-nm thick and its permittivity is given in Reference [66]. The SiO_2 unit layer is 100-nm thick and have a permittivity (ϵ_{SiO_2}) following the relationship with wavelength (λ, with unit of μm) as[67]

$$\epsilon_{SiO_2} = 1 + \frac{0.6961663\lambda^2}{\lambda^2 - 0.0684043^2} + \frac{0.4079426\lambda^2}{\lambda^2 - 0.1162414^2} + \frac{0.8974794\lambda^2}{\lambda^2 - 9.896161^2} \tag{2.8}$$

Figure 2.2 presents the real part of effective epsilon ($\mathrm{Re}(\epsilon_{\perp})$) of 3-, 4-, 5-, 6- and 10-bilayer Ag/SiO_2 multilayer structure, calculated based on Fresnel's equations. The calculation method is considering the multilayer structure consisted of Ag and SiO_2 unit layers with parameters (thickness and refractive index) stated above. The mechanics and procedure of the calculation are detailed demonstrated in Chapter 3.

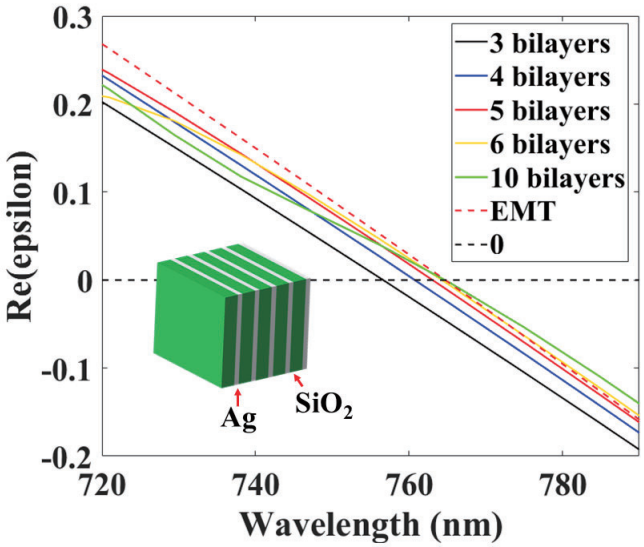

Figure 2.2: Real part of epsilon ($\mathrm{Re}(\epsilon_{\perp})$) of Ag/SiO_2 multilayer structure under the conditions of 3, 4, 5, 6 and 10 bilayers and EMT assumption.

The Re($\epsilon_\perp$) of the Ag/SiO_2 multilayer structure based on EMT (Equation 2.3) is also shown in Figure 2.2. The zero-permittivity wavelength is approaching the EMT assumption along with the increasing of the number of bilayers. Typically, the 5-, 6- and 10-bilayer structures reach the EMT assumption. However, the curves of the effective permittivities of 6- and 10-bilayer structures show obvious oscillation. This phenomenon is due to the thickness of these structures reach the wavelength scale or more, i.e. beyond the sub-wavelength scale, where the film shows obvious etalon effect[64, 68, 69]. This effect is also predicted by the EMT and limit the total thickness of the multilayer structure. Therefore, the 5-bilayer structure can be considered as a practicable EMT model, and this is also verified in the experiments shown in Chapter 3 and 4.

2.1.2 Realisation of IENZ MMs

Most metals show negative permittivity at optical range because their plasma frequencies are at ultraviolet (UV) range[70]. To "lower" the ω_p, it is better to use chemical reacting or doping approaches to create metal-dielectric compounds. The dielectric components with positive permittivity are able to increase the effective permittivity of the metal-dielectric compounds into ENZ and even positive ranges. This phenomenon can be treated as lower the ω_p of the compounds and is a popular way to realise the ENZ media. Notably, the TCOs are created to exhibit ENZ response using this approach.

Examples of TCOs are metal oxide or metal nitride, for example the ITO, AZO and titanium nitride (TiN). They have high carrier concentration with typical values usually more than 10^{20}cm^{-3}[71], and thus the high conductivity, and this make it possible to realise the electro-optical response. Due to the all-dielectric structure, TCOs also exhibit relatively low optical losses, compared to metals. These peculiar plasmonic characteristics motivate TCOs to be widely used in the field of superlensing[72] and optical modulation[73].

Here we focus on ITO.

ITO is stannum (Sn) (i.e. Tin) doped indium oxide (In_2O_3) and its free-electron response can also be described by the Drude-Sommerfeld model as Equation 2.1. The ω_p is defined as

$$\omega_p = \sqrt{\frac{n_c e^2}{\epsilon_0 m^*}} \tag{2.9}$$

where n_c is the carrier density, e isthe elementary charge, m^* is the effective mass of electron. Specifically for ITO, $m^* \approx 0.35 m_0$, where m_0 is the mass of free electron.

To achieve the aim of zero permittivity, we can modify the n_c by changing the doping level of Sn during fabrication. In general, the n_c of ITO thin film is at the magnitude range from 10^{20} to

10^{22}cm^{-3}. Hence, we can obtain the ITO films with the ENZ range of ITO locates at NIR region, typically around 1500 nm[62] (Figure 2.3 (a)) and also low losses (Figure 2.3 (b)).

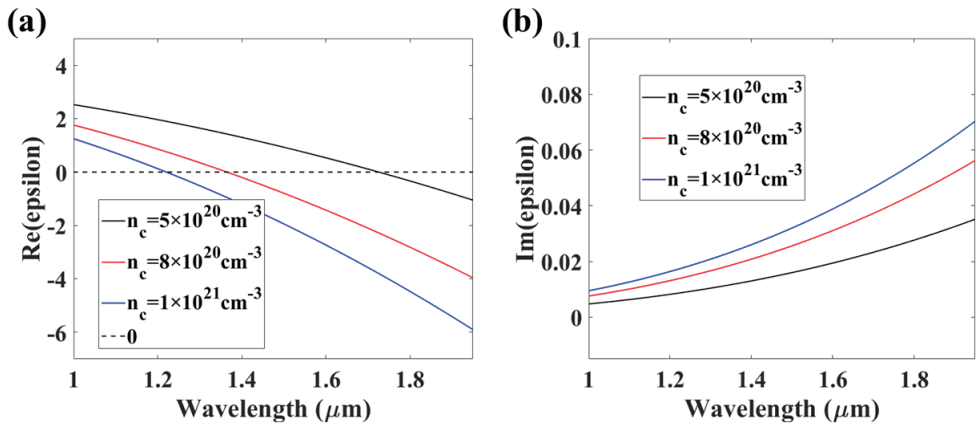

Figure 2.3: Real (a) and imaginary (b) parts of permittivities of ITO with different carrier densities (n_c).

2.2 Optical wave modification inside ENZ MMs

This section will briefly discuss the optical response of ENZ MMs, including the elliptical and hyperbolic optical responses.

First we consider a optical wave with angular frequency ω propagating through an AENZ slab, i.e. the metal-dielectric multilayer structure shown in Figure 2.1 (a). The optical wave can be described as $\mathbf{E}(\mathbf{r},t) = E_0 e^{i(\mathbf{kr}-\omega t)}$, where $\mathbf{r} = (x,y,z)$ represents the radius distance, t is propagation time and $\mathbf{k} = (k_x, k_y, k_z)$ is the wave vector which is defined by

$$\mathbf{k} = \frac{2\pi}{\lambda} \tag{2.10}$$

where λ is wavelength.

Inside the material, the dispersion relation is shown as

$$\frac{k_x^2 + k_y^2}{\epsilon_{\parallel}} + \frac{k_z^2}{\epsilon_{\perp}} = \frac{\omega^2}{c^2} \tag{2.11}$$

where c is the speed of light in vacuum.

Equation 2.11 shows that the dispersion response depends on the value and sign of the $\epsilon_{\parallel}$ and $\epsilon_{\perp}$. For isotopic media, such as vacuum, air and dielectric materials, whose $\epsilon_{\parallel}$ and $\epsilon_{\perp}$ are both positive, the elliptical response occurs (Figure 2.4 (a)). If a material exhibit the relation of $\epsilon_{\parallel} \cdot \epsilon_{\perp} < 0$, the

material undergoes a hyperbolic dispersion (Figure 2.4 (d) and (e)). Between these two situations, the ENZ responses occur. One condition is when $\epsilon_\perp \approx 0$ and $\epsilon_\parallel > 0$, the isofrequency surface is compressed into $k_x - k_y$ plane in the **k** space (Figure 2.4 (b)). The other one is when $\epsilon_\perp \approx 0$ and $\epsilon_\parallel < 0$, the isofrequency surface is also compressed, but exhibiting a hyperbolic behaviour (Figure 2.4 (c)).

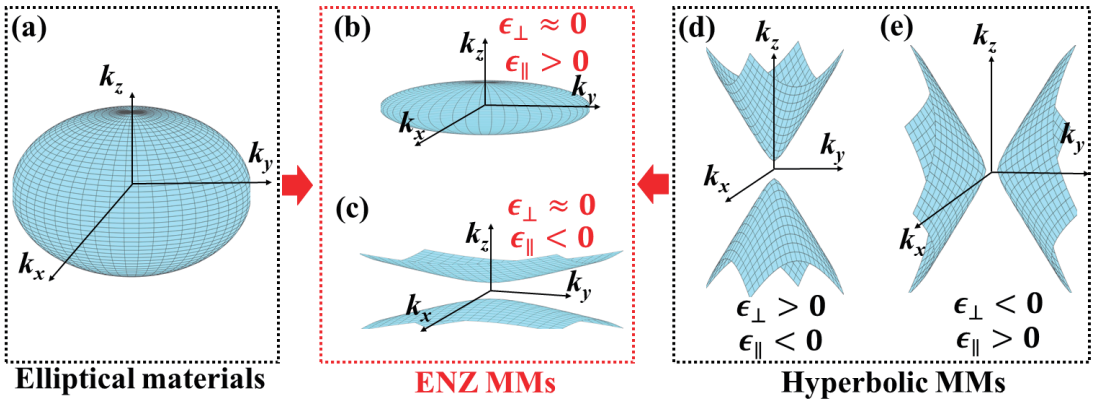

Figure 2.4: Isofrequency surfaces of elliptical materials (a), ENZ MMs (b and c) and hyperbolic MMs (d and e), shown in the **k** space.

To show the radiation patterns or the distribution of electromagnetic fields of these media with different dispersion responses, some works have been done in Reference [74]. Figure 2.5 illustrates the far-field distribution of electromagnetic fields, i.e. radiation patterns, when a light source is embedded inside these materials. Here, we consider an electric dipole as the source located at x direction with a generated H-field shown in Figure 2.5 (a). Inside elliptical materials, the radiation pattern of the dipole keeps similar diverging shape as the source emitted, because $\epsilon_\parallel$ and $\epsilon_\perp$ are all positive. In the hyperbolic regime, the radian patterns exhibit different behaviour when light propagating in them, i.e. dielectric ($\epsilon_\perp > 0$ and $\epsilon_\parallel < 0$) and metallic ($\epsilon_\perp < 0$ and $\epsilon_\parallel > 0$) dispersions[75, 76]. The dielectric hyperbolic MMs exhibit converging light propagation effect (Figure 2.5 (c)), which shows the potential for realising directional emitting and imaging[77, 78]. On the contrary, light propagates along the resonance cone in the metallic hyperbolic MMs (Figure 2.5 (d)), and this phenomena will benefit the ultra-fine light probing[74, 79].

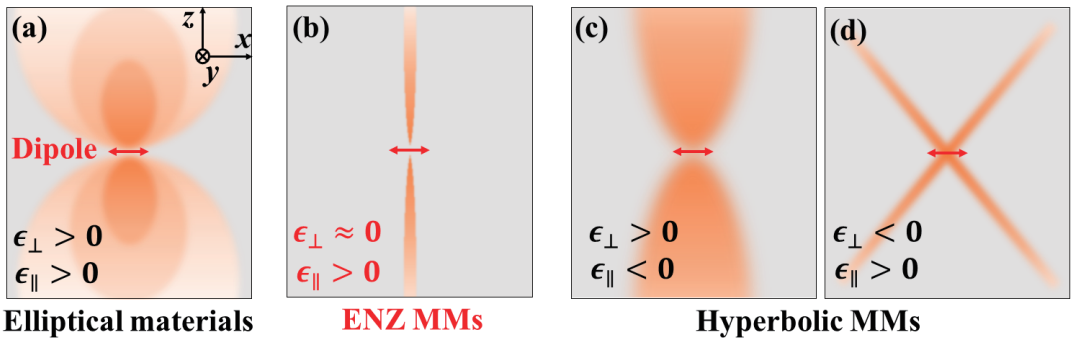

Figure 2.5: Diagram of typical radiation patterns of a dipole located in elliptical materials (a), ENZ MMs (b) and hyperbolic MMs (c and d)[74].

Under the circumstance of $\epsilon_\perp \approx 0$ and $\epsilon_\parallel > 0$, the k_z is close to 0, and thus the optical wave propagate along the z direction with a diverging wavelength and vanishing spatial dispersion. Then the field distribution will not change during propagation. Therefore, the radiation pattern in this ENZ medium shows high directional and low divergence (Figure 2.5 (b)). The other ENZ condition ($\epsilon_\perp \approx 0$ and $\epsilon_\parallel < 0$) also shows similar optical response due to the vanishing value of $\epsilon_\perp$[74]. This effect promises the capability to break the diffraction limitation due to the lack of spatial dispersion. Typically, if we curve this AENZ membrane and coat it onto specific nanopatterns or nanoemitters, the light propagating inside the medium will show negligible phase changing, and thus the sub-wavelength imaging without diffraction can be achieved[34].

Here we discuss the IENZ medium, i.e. the medium showing ENZ response only in specific directions.

We already know that the permittivity of the IENZ structure is close to 0 at specific frequencies, and thus the refractive index (n) tends to 0 as well, for the low-loss materials. This means that even the light propagate a long distance (d) inside this medium, the phase changing $\Delta\phi = nkd$ will remain almost 0. In this case, the direction of output light from ENZ medium is perpendicular to the exit surface[21]. For example, we consider a point source embedded in a ENZ slab, shown in Figure 2.6. At the medium/air interface, the angle of refraction (θ_t) approaches to 0 no matter how the angle of incidence (θ_{in}) changes, according to the Snell's Law[80]

$$n_t \sin\theta_t = n \sin\theta_{in} \tag{2.12}$$

where n_t means the refractive index of transmitting medium (i.e. air in Figure 2.6).

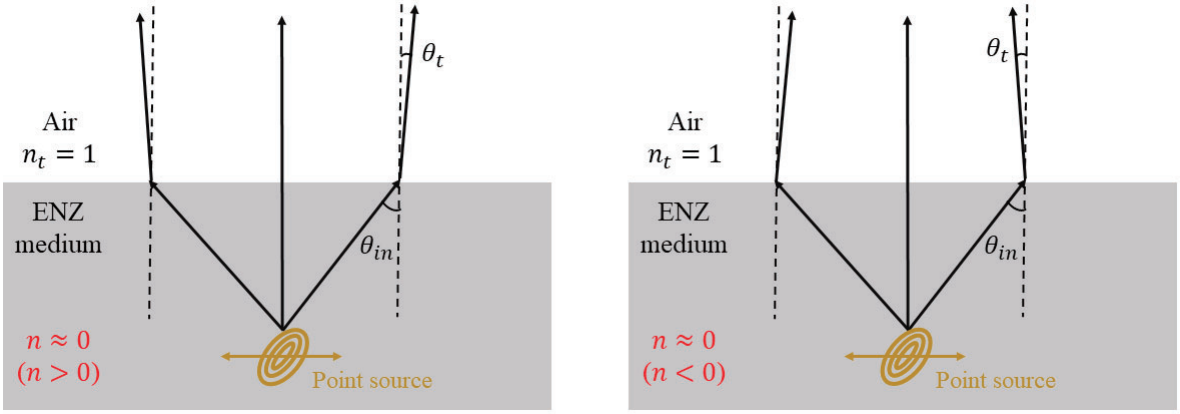

Figure 2.6: A point source is embedded in a ENZ medium and the output lights are all perpendicular to the air/medium interface due to $n \approx 0$.

Besides, because the internal field is irrotational field, the ENZ medium only allow the optical wave with infinite phase velocity propagating through. Hence, the phase changing during propagation is closed to 0, which also matches the discussion of Equation 2.11.

Based on the characteristic of the perpendicular exit and near-zero phase variation, we can realise the wave-front modification by controlling the exit surface of the ENZ medium[38]. Figure 1.3 (b) sketches this process. A curved wavefront propagates through a ENZ slab and the exit wavefront becomes parallel to the exit surface.

2.3 Asymmetric transmission enhanced by the AENZ slab

Asymmetric transmission for forward and backward propagation of tilted circular polarised optical waves usually occur in chiral MMs by breaking either the Lorentz reciprocity[44] or the spatial inversion symmetry[36, 81]. The enhancement of optical activity (dichroism and circular birefringence) in 1D chiral MMs operating around the ENZ condition has been reported in Reference [36]. Chirality is a common property in the molecular material research field, photonics and nanotechnology. Chirality in bulk materials is ubiquitous in nature, but 2D or 1D chiral materials are rarely seen[40, 42, 82, 83]. This section demonstrates that the asymmetric transmission can be supported by a sub-wavelength AENZ slab and undergo a marked nonresonant enhancement in the ENZ regime. This nonresonant enhancement effect results from the contributions of the nonlocal response when the permittivity approaches zero, which is comparable or even greater than the local parts of the dielectric response[60, 84, 85]. In addition, in linear ENZ MMs, the nonlocal response can also affect

the medium response, which can be utilized to enhance nonlocal phenomena such as the excitation of additional waves[86]. Here we propose that nonlocal effects due to 1D chirality are enhanced by the ENZ effect without any resonant mechanisms (i.e., with no cavity or plasmonic effects).

Figure 2.7 sketches a ultra-thin slab with thickness L consisted of periodic Ag/air bilayers. The structure period is Λ and the filling fraction of Ag layer is f_{Ag}. A monochromatic plane wave of wavelength λ_0 probes the slab forward and backward with incident angles θ and φ. The incident waves can be both left-handed circular polarised (LHCP) and right-handed circular polarised (RHCP), and also both forward and backward.

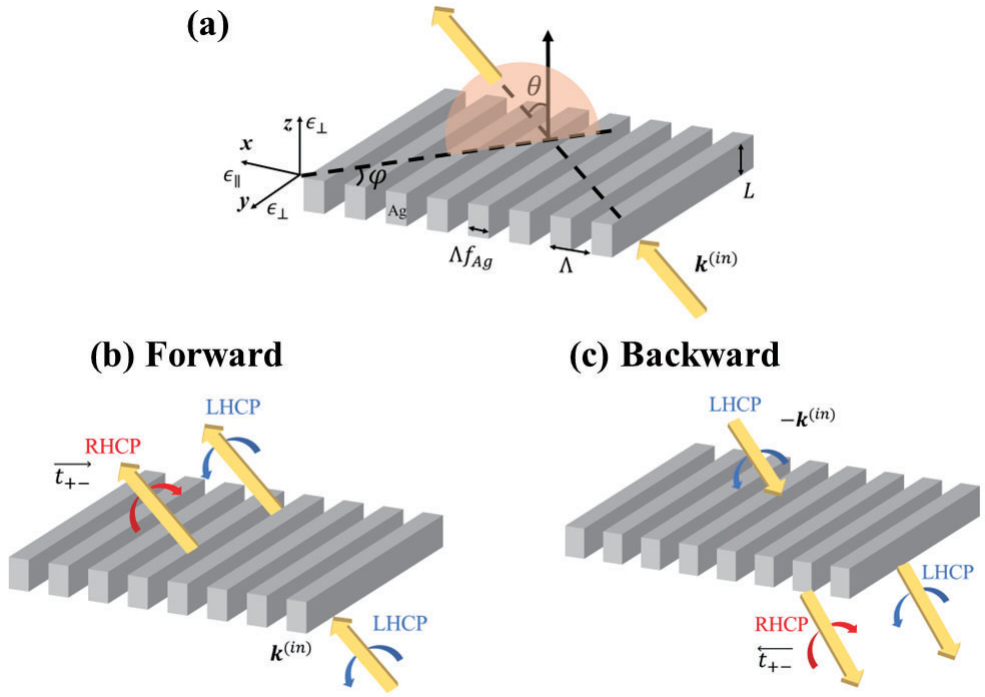

Figure 2.7: Geometry of the asymmetric transmission process. (a) Schematic view of the tilted plane wave (yellow arrow) impinging onto a ENZ slab consisted of Ag/air bilayers and the definition of the Cartesian coordinate and angular parameters. Propagation direction is defined as forward for the $\mathbf{k}^{(in)}$ direction (b) and backward for the $-\mathbf{k}^{(in)}$ direction (c).

The wave vector of the incident wave $\mathbf{k}^{(in)}$ can be described as

$$\mathbf{k}^{(in)} = k_x^{(in)}\hat{\mathbf{e}}_x + k_y^{(in)}\hat{\mathbf{e}}_y + k_z^{(in)}\hat{\mathbf{e}}_z = k_0(\sin\theta\cos\varphi\hat{\mathbf{e}}_x + \sin\theta\sin\varphi\hat{\mathbf{e}}_y + \cos\theta\hat{\mathbf{e}}_z) \tag{2.13}$$

where superscript (in) represents incident wave, $(\hat{\mathbf{e}}_x, \hat{\mathbf{e}}_y, \hat{\mathbf{e}}_z)$ are the unit vectors in Cartesian coordinate, (k_x, k_y, k_z) are the components in $\mathbf{k}$ space and $k_0 = 2\pi/\lambda_0$.

The dielectric response here is also described as Equation 2.2 and there are two forward waves excited inside the slab, viz. the ordinary (o) and extraordinary (e) plane waves, whose longitudinal wave vectors are

$$k_z^{(o)} = \sqrt{k_0^2 \epsilon_\perp - (k_x^2 + k_y^2)} \tag{2.14}$$

$$k_z^{(e)} = \sqrt{k_0^2 \epsilon_\parallel - (k_x^2 \frac{\epsilon_\parallel}{\epsilon_\perp} + k_y^2)} \tag{2.15}$$

At hyperbolic ENZ range where $\epsilon_\perp \approx 0$ ($\epsilon_\perp < 0$) and $\epsilon_\parallel > 0$, the ordinary wave is evanescent ($k_z^{(o)} = \sqrt{-(k_x^2 + k_y^2)}$), whereas the extraordinary wave is a propagating mode and it can accumulate the desired propagation phase even if the slab is ultrathin. Actually, the hyperbolic dispersion in the ENZ regime leads to the large longitudinal wave vectors for extraordinary waves ($k_z^{(e)} \gg k_0$), thus triggered the etalon resonances and enhance the asymmetric response of transmissions in forward and backward directions[87].

To quantify the asymmetric transmission, we consider the linear and circular polarisation for the optical wave.

First, for linear polarisation, TE(s) and TM(p), whose basis is ($\widehat{\mathbf{e}}_s = -\sin\varphi\widehat{\mathbf{e}}_x + \cos\varphi\widehat{\mathbf{e}}_y$, $\widehat{\mathbf{e}}_p = \cos\theta\cos\varphi\widehat{\mathbf{e}}_x + \cos\theta\sin\varphi\widehat{\mathbf{e}}_y - \sin\theta\widehat{\mathbf{e}}_z$), the forward transmission matrix ($\overrightarrow{\mathbf{T}_l}$) is obtained by

$$\begin{pmatrix} E_p^{(t)} \\ E_s^{(t)} \end{pmatrix} = \begin{pmatrix} \overrightarrow{t_{pp}} & \overrightarrow{t_{ps}} \\ \overrightarrow{t_{sp}} & \overrightarrow{t_{ss}} \end{pmatrix} \begin{pmatrix} E_p^{(in)} \\ E_s^{(in)} \end{pmatrix} = \overrightarrow{\mathbf{T}_l} \begin{pmatrix} E_p^{(in)} \\ E_s^{(in)} \end{pmatrix} \tag{2.16}$$

where $\mathbf{E}^{(in)} = (E_p^{(in)}, E_s^{(in)})$ and $\mathbf{E}^{(t)} = (E_p^{(in)}, E_s^{(in)})$ are the incident and transmitted electric fields, $\overrightarrow{t_{uv}}$ $(u, v = p, s)$ means the matrix component of $\overrightarrow{\mathbf{T}_l}$.

As we consider the anisotropic slab, the cross-polarisation transmission coefficients are same and nonzero, i.e.

$$\overrightarrow{t_{ps}} = \overrightarrow{t_{sp}} \neq 0 \tag{2.17}$$

Similarly, the forward transmission matrix ($\overrightarrow{\mathbf{T}_c}$) of left ($+$) and right ($-$) circular polarisations, whose basis is ($\widehat{\mathbf{e}}_+ = (\widehat{\mathbf{e}}_p + i\widehat{\mathbf{e}}_s)/\sqrt{2}$, $\widehat{\mathbf{e}}_- = (\widehat{\mathbf{e}}_p - i\widehat{\mathbf{e}}_s)/\sqrt{2}$), can be described as

$$\overrightarrow{\mathbf{T}_c} = \begin{pmatrix} \overrightarrow{t_{++}} & \overrightarrow{t_{+-}} \\ \overrightarrow{t_{-+}} & \overrightarrow{t_{--}} \end{pmatrix} \tag{2.18}$$

where the matrix components are

$$\begin{aligned}
\overrightarrow{t_{++}} &= \frac{1}{2}(\overrightarrow{t_{pp}} + \overrightarrow{t_{ss}}) \\
\overrightarrow{t_{+-}} &= \frac{1}{2}(\overrightarrow{t_{pp}} - \overrightarrow{t_{ss}} - i2\overrightarrow{t_{ps}}) \\
\overrightarrow{t_{-+}} &= \frac{1}{2}(\overrightarrow{t_{pp}} - \overrightarrow{t_{ss}} + i2\overrightarrow{t_{ps}}) \\
\overrightarrow{t_{--}} &= \frac{1}{2}(\overrightarrow{t_{pp}} + \overrightarrow{t_{ss}})
\end{aligned} \tag{2.19}$$

In the situation of backward probing where the incident wave propagates along $-\mathbf{k}^{(in)}$ direction, the backward transmission matrices for linearly and circular polarised bases can be obtained based on the reciprocal theorem[88]. Furthermore, the asymmetric transmissions for linear and circular polarisations are characterised by the parameters

$$\Delta_l = \left|\overrightarrow{t_{sp}}\right|^2 - \left|\overleftarrow{t_{sp}}\right|^2 = \left|\overrightarrow{t_{sp}}\right|^2 - \left|\overrightarrow{t_{ps}}\right|^2 \tag{2.20}$$

$$\Delta_c = \left|\overrightarrow{t_{+-}}\right|^2 - \left|\overleftarrow{t_{+-}}\right|^2 = \left|\overrightarrow{t_{+-}}\right|^2 - \left|\overrightarrow{t_{-+}}\right|^2 \tag{2.21}$$

Using Equations 2.17 and 2.20, we can obtain $\Delta_l = 0$, which means that the asymmetric transmission is not supported by linearly polarised waves.

From Equations 2.19 and 2.21, the asymmetric transmission parameter for circular polarised basis is rearranged, shown as

$$\Delta_c = 2\,|\Delta t|\,\left|\overrightarrow{t_{sp}}\right|\sin(\Delta\psi) \tag{2.22}$$

where $\Delta t = \overrightarrow{t_{pp}} - \overrightarrow{t_{ss}}$ and $\Delta\psi = \arg(\Delta t\overrightarrow{t_{ps}}^*)$.

Equation 2.22 shows that the asymmetric transmission for tilted circular polarised waves results from both the linear polarisation asymmetric response ($\Delta t \neq 0$) and the presence of the linear cross-polarisation conversion ($\overrightarrow{t_{ps}} \neq 0$). These two factors are the natural characteristics of the uniaxial medium. Therefore, the values of Δt and $\overrightarrow{t_{ps}}$ are the keys to achieving a dramatic enhancement of the asymmetric transmission.

A specific Ag/air structure is demonstrated here to show the enhancement of the asymmetric transmission in the AENZ regime. The parameters of the structure (Figure 2.7 (a)) are $L = 30\,\text{nm}$, $f_{Ag} = 0.5$ and $\theta = 60^\circ$. The permittivity of Ag is obtained by Equation 2.1, where $\epsilon = 5$, $\omega_p = 14 \times 10^{15}\,\text{Hz}$ and $\gamma = 32 \times 10^{13}\,\text{Hz}$.

Under the homogenised condition where $\Lambda \ll \lambda$, effective permittivity of the Ag/air structure is obtained using EMT, i.e. Equations 2.2, 2.3 and 2.4, and the zero-permittivity point ($Re(\epsilon_\perp) = 0$) locates at $\lambda = 0.4\,\mu$m, indicated in Figure 2.8 (a).

Figure 2.8 (b) illustrates the asymmetric transmission Δ_c versus λ and φ. The maximum $\Delta_c \approx 0.2$ is obtained at $\lambda = 0.42\,\mu$m and $\varphi = 45^\circ$ where $\epsilon_\perp = -0.14 + i0.14$ and $\epsilon_\parallel = 1.32 + i0.01$.

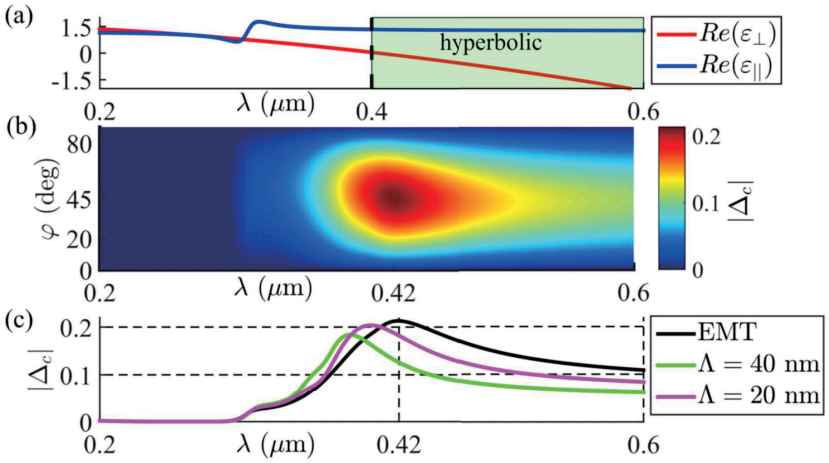

Figure 2.8: Numerical simulation results of the asymmetry transmissions in the ENZ slab sketched in Figure 2.7.[89] (a) Real part of $\epsilon_\perp$ as a function of λ (the shadow area indicates hyperbolic region). (b) Δ_c parameter as a function of φ and λ for $\theta = 60^\circ$ and $L = 30\,$nm. (c) Comparison between the asymmetric transmission evaluated with EMT (black solid line) and those predicted by the rigorous coupled-wave analysis for different values of the spatial period Λ.

For the purpose of verifying the above results attained based on EMT and also discussing the influence of spatial nonlocality on the considered asymmetric transmission, we use another numerical method, namely the rigorous coupled-wave analysis technique[90], to calculate the asymmetric transmission Δ_c.

Figure 2.8 (c) exhibits the comparison between the asymmetric transmission evaluated with EMT and those predicted by the rigorous coupled-wave analysis for different values of Λ, at $\varphi = 45^\circ$ and $\theta = 60^\circ$. The nonlocality impacts the results in the ENZ regime and it slightly reduces the value of the Δ_c. Therefore, the results of the rigorous coupled-wave analysis method initially prove that the asymmetric transmission is purely related to the homogeneous structure response.

The work of this section has been published in the journal "Journal of Optics", see Reference[89]. We have demonstrated that the 1D ENZ slab can exhibit the asymmetric transmission of different circularly polarised light which are typically shown in complex 2D and 3D chiral structures. Additionally, the optical like-diode response is enhanced dramatically in the ENZ regime. We believe that

our investigation constitutes a fundamental step for the realisation of compact polarisation devices.

2.4 Emission enhancement on the ENZ substrate

Here, we discuss the emission enhancement of the condition where the light source (e.g. dipole or nanoantenna) locate on top of an ENZ medium.

As $\epsilon \approx 0$, the refractive index (n) of the ENZ medium also approaches 0. Therefore, air is an optically denser medium comparing to the ENZ medium. Considering the situation where a light beam propagates from a optically denser medium (e.g. air) to a optically thinner medium (e.g. ENZ slab), the total reflection phenomenon will be launched where incident angle (θ_{in}) reaches critical angle (θ_c). Based on Snell's Law[80], the θ_c is determined when the transmitted angle (θ_t) reaches 90°, as $\theta_c = \arcsin(\frac{n_t}{n_d})$, where n_d and n_t are the refractive indices of the optically denser and thinner media, respectively. At the interface between ENZ medium and air, $n_t = n_{ENZ} \approx 0$ and $n_d = n_{air} = 1$, hence $\theta_c \approx 0$, which means that the total reflection occurs at all incident angles.

Figure 2.9 sketched the air/substrate model with a plasmonic nanoantenna (light source) located on top of the substrate at the interface[47]. The permittivity of substrate varies from positive ($\epsilon > 1$) through near-zero ($\epsilon \approx 0$) to negative ($\epsilon < -1$). When the light source is placed on top a substrate with $\epsilon > 1$, such as dielectric materials with low loss, the emission is mainly scattered into the substrate (Figure 2.9 (a)). When the substrate is switched to ENZ medium, most emission energy has been squeezed into the air direction (Figure 2.9 (b)), because the air is optically denser than the substrate and thus the total reflection occurs. If the permittivity of the substrate decreasing down to negative, the emission of the source propagating in the substrate part vanishes quickly (Figure 2.9 (c)), because of the high conductivity of the substrate for the electromagnetic fields[91], and this phenomena typically happens in metals.

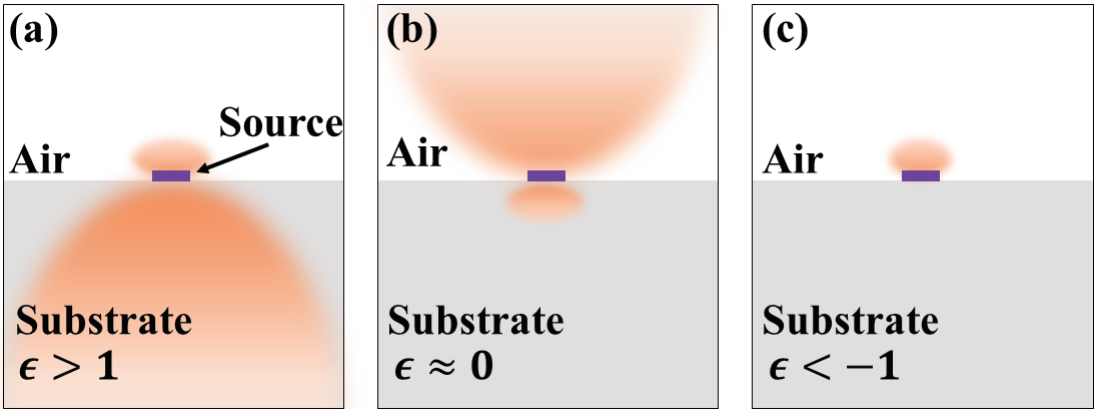

Figure 2.9: Diagram of the emission distribution of light source located on top of substrates with different permittivities: $\epsilon > 1$ (a), $\epsilon \approx 0$ (b) and $\epsilon < -1$ (c)[47].

Hence, the emission will be enhanced due to the presence of the ENZ substrate, and this effect is verified by our demonstration in Chapter 3.

In reality, we need to consider the complex refractive index ($\boldsymbol{n}$) which consisted with the real part (n') and imaginary part (n'', the extinction coefficient), i.e. $\boldsymbol{n} = n' + in''$. Similarly, the complex permittivity is $\boldsymbol{\epsilon} = \epsilon' + i\epsilon''$. Then, the real part of the refractive index is determined by permittivity as

$$n' = \sqrt{\frac{|\boldsymbol{\epsilon}| + \epsilon'}{2}} \tag{2.23}$$

where $|\boldsymbol{\epsilon}| = \sqrt{\epsilon'^2 + \epsilon''^2}$.

The optical loss of the medium (n'') is also obtained

$$n'' = \sqrt{\frac{|\boldsymbol{\epsilon}| - \epsilon'}{2}} \tag{2.24}$$

By designing the ENZ structure using material with small ϵ'', we can realise the emission enhancement with low optical loss. Meanwhile, the ENZ substrate can concentrate the emission direction perpendicular to the interface due as the wave-front modification will be launched even with the distances just in the size of several free-space wavelengths[47], as we discussed in Section 2.2.

2.5 Summary

Based on EMT and Drude-Sommerfeld model, we can design, modify and manipulate the effective permittivity of anisotropic and homogeneous structures and obtain the AENZ and IENZ media. This ability motivates the applications of ENZ media in phase variation minimising and wave-front modification. Additionally, the asymmetric transmission effect is enhanced in the ENZ regime. The ENZ substrate is also capable of enhancing the emission of light sources with high directivity. Based on these works, ENZ MMs open up important applications in the fields of sub-wavelength imaging, emission modifying and optical sensing, etc. However, in the following chapters, I have only focused on my works, which aims at the approaches to realising ENZ MMs and some other ENZ hybrid platforms and typical applications related.

Chapter 3

Fabrication, characterisation of multilayer ENZ structures and related emission enhancement

This chapter demonstrates an approach to fabricate metal/dielectric multilayer ENZ structure using e-beam evaporation method. The retrieval method to optically characterising the ENZ samples is also explained in detail. Using this ENZ structure as substrate, we are able to enhance the emission of gallium arsenide (GaAs) QDs.

The outline of this chapter starts with an overview of the nanotechniques used in the fabrication of multilayer ENZ structures, before the explanation of the details of the fabrication process, typically the e-beam evaporation. The optical characterisation of each unit layer and the multilayer structure are also demonstrated here. Then, the numerical simulation and experimental verifying of the emission enhancement on ENZ substrate are presented. The final section summarises with a discussion of the influence of the fabrication and characterisation methods on the ENZ MMs for further optical applications.

3.1 Overview

According to EMT, we realise the ENZ structure by layering materials with positive (dielectric) and negative (metal) permittivity, with sub-wavelength thicknesses that are chosen so that the real part of the effective permittivity crosses zero at the desired wavelength, e.g. visible range. The deposition of each unit layers is implemented inside the chamber of an e-beam evaporator typically without breaking the vacuum. The e-beam evaporation technique is able to deposit both metal (e.g.

Ag, Au and germanium (Ge)) and dielectric (e.g. SiO_2 and zinc selenide (ZnSe)) thin layers, with high-accuracy thickness and ultra-high purity. This approach provides a way to realise the multilayer ENZ structure in large scale and controllable thickness.

In this work, we also demonstrate a method to retrieve the permittivity of optical films, based on Fresnel's law[80]. This approach is able to determine the effective permittivity values of a given slab by combining the thickness, transmission and reflection, without considering the other details inside the structure. Using this method, we can characterise the optical properties of ENZ structures and their unit layers.

Based on this ENZ platform, we also propose and demonstrate an approach to enhance the emission properties of GaAs QDs at a specific wavelength range.

3.2 Fabrication

To achieve the ENZ condition at visible range with low loss, we design the multilayer ENZ structure formed by unit layers of Ag and SiO_2. In the visible regime, Ag with negative permittivity exhibits lower loss than most noble metals[92, 93], and SiO_2 with positive permittivity shows good thermal stability and also negligible optical loss. In the designed multilayer ENZ structure, unit layers have sub-wavelength thicknesses to satisfy the requirement of EMT. Additionally, the thickness of the Ag layer is required to be as lower as possible to reduce the optical loss of the whole structure. Therefore, the thickness of Ag and SiO_2 unit layers are determined as $t_m = 6\,\text{nm}$ and $t_m = 60\,\text{nm}$, sketched in Figure 3.1. In order to make the multilayer structure symmetry, the top and bottom layers are all SiO_2 films with a thickness of $t_d/2$. The substrates to hold the structure are square coverglass (Agar) with side length of 24 mm and thickness of 200 µm.

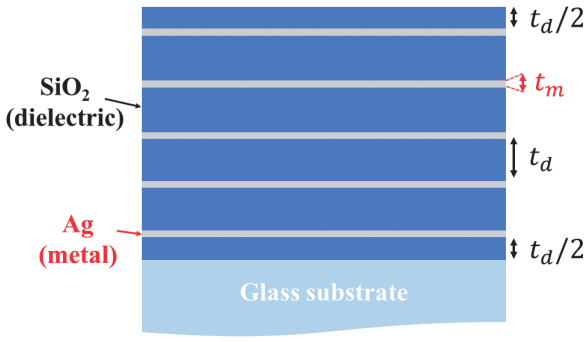

Figure 3.1: Diagram of the multilayer ENZ structure consisted of Ag and SiO_2 unit layers. t_m and t_d are the thickness of Ag and SiO_2 layers, respectively.

The multilayer metal/dielectric structure is fabricated using an e-beam evaporation approach. The diagram of the e-beam evaporator (Edwards AUTO 306) is shown in Figure 3.2. The target material (Ag or SiO_2) was stored in a tungsten (W) crucible which held by a water-cooled hearth. During the evaporation process, the target material was bombarded with a focused electron beam (FEB) deflected by a magnet system, thus evaporated into gaseous particles and finally forming thin layers when reached the substrate right above the crucible. Typically, the beam current was set at about 45 µA for Ag and 6 µA for SiO_2 to reach an evaporation rate of 0.1 nm s^{-1}. A quartz crystal detector was used to monitor the evaporation rate and thickness. By modifying the tooling factor of the detector, we could calibrate the thickness of deposited films. During the evaporation process, the substrate holder was rotating all the time, around the axis perpendicular to its bottom surface, to improving the smoothness of deposited layers. The whole evaporation process was performed in a high-vacuum chamber with a base pressure of about 3×10^{-6} mbar and a working pressure that less than 2×10^{-5} mbar.

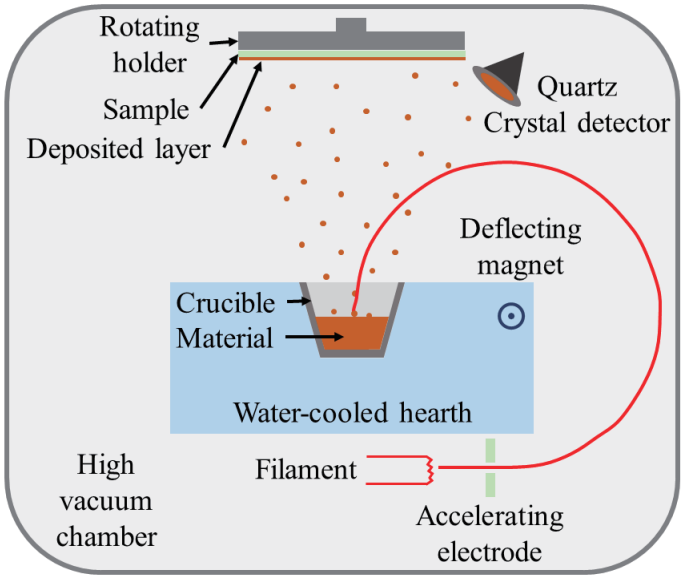

Figure 3.2: Diagram of the e-beam evaporator, formed with filament for generating electron beams, electrode for accelerating and focusing electron beams, magnet system for deflecting electron beams, W crucible for holding target materials, water-cooled system to accommodating the crucible, quartz crystal detector for monitoring evaporation rate, and the rotating holder of samples.

The e-beam evaporation approach can deposit large and uniform metal and dielectric thin films. The maximum size of the deposited film reaches 10 cm×10 cm, which is the size of the sample holder. However, e-beam evaporation technique has some disadvantages. Because the evaporation process is activated by the electron beam, this approach is not suitable for some electron beam

lithography (EBL) steps where the photoresist layers need to keep undeveloped. The evaporated materials are typically amorphous, which leads to high resistivity for some materials, such as metals and ITO[94–96]. Additionally, due to the poor wettability of some noble metals (e.g. Ag), the evaporated films, typically at ultra-thin range (under 50 nm), have a relatively rough surface due to the cluster effect[97]. For example, in the designed multilayer ENZ structure, unit layers should have a thickness in the sub-wavelength scale to satisfy the requirement of EMT. Typically, the Ag layer is extremely thin (6 nm) and required to be homogeneous. However, the deposited 6-nm Ag layer on glass substrate has high roughness and shows blue but not silver colour (see the photograph of the Ag sample in Figure 3.3).

Figure 3.3: Photographs of the 6-nm Ag samples with and without the Ge wetting layer. The mark of Ag means that the Ag layer was deposited directly on the glass substrate, while the Ge/Ag mark means that there was a 0.7-nm Ge layer evaporated on the glass substrate prior to the deposition of Ag layer.

This phenomenon is due to the Rayleigh scattering occurred at the rough Ag surface, where the nanoscale clusters and cracks randomly distributed. The scanning electron microscope (SEM) image of the 6-nm Ag layer (Figure 3.4 (a)) also verifies this by showing obvious defects on its surface. The dimension of the Ag clusters is around 50 nm, which is about 1/10 of the wavelength of blue light. Therefore, the rough Ag layer scatters blue light and shorter-wavelength light more, compared to the light at other wavelength range. This effect not only leads to the scattering issue but also causes high optical loss[98–100].

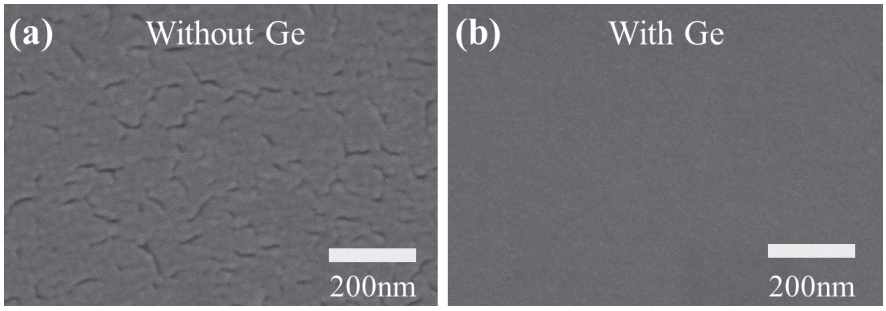

Figure 3.4: SEM images of the 6-nm Ag layers deposited on glass substrates with and without the Ge wetting layer, to showing the surface morphology.

To improve the smoothness of Ag layers, a popular method is introducing a nucleation layer[98] prior to the deposition of the Ag layer. Here, we use a Ge layer to improve the uniformity of the ultra-thin Ag layer. In order to find the most suitable thickness of the Ge wetting layer, we have already deposited Ge layers with different thickness varying from 0.3 to 1.5 nm. Finally, the 0.7-nm thick Ge layer has been determined as the wetting layer for evaporating ultra-thin Ag layers.

Figure 3.4 (b) shows the surface morphology of the Ag layer with Ge wetting layer, the presence of Ge wetting layer reduce the surface roughness dramatically. Most cracks and defects on the surface of Ag layer have been wiped out, compared to Figure 3.4 (a). During the observation process of the Ag samples with and without the Ge wetting layer using SEM, I focused on some dust particles (reference focus points) just beside the imaging position to make sure that the focus condition of different images (Figure 3.4 (a) and (b)) are at same level.

Besides, the Ge/Ag sample shows silver colour (Figure 3.3) rather than blue, and this also verifies the improvement of the smoothness of Ag layer. We used the Ge wetting layer for improving the smoothness of Ag layers in the fabrication of multilayer ENZ structures, and the whole fabrication process is shown in Figure 3.5.

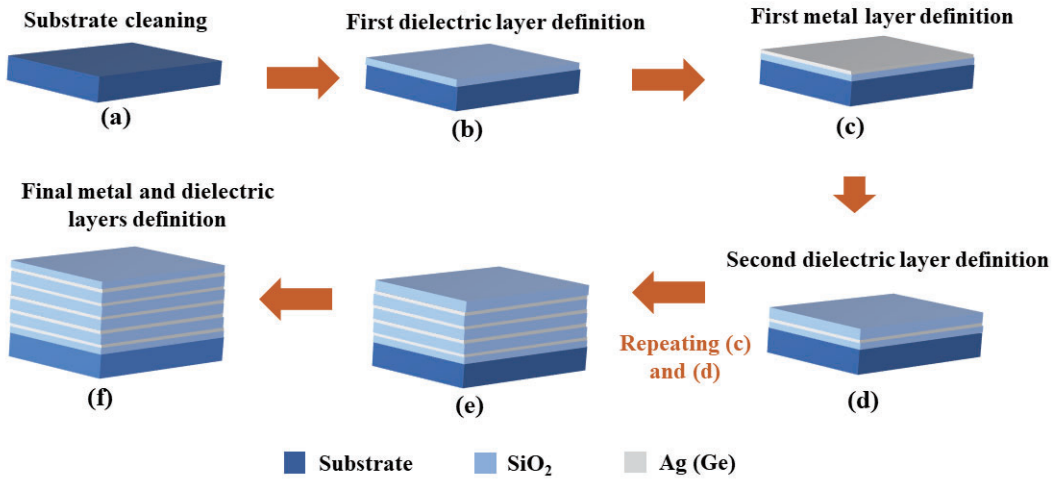

Figure 3.5: Fabrication process of multilayer Ag(Ge)/SiO_2 structure. (a) The cleaning of glass substrate using solvents. (b) The definition of first dielectric (SiO_2) layer with thickness of $t_d/2$. (c) The definition of first metal (Ag) layer with thickness of t_m. (d) The definition of second SiO_2 layer with thickness of t_d. (e) Repeating process (c) and (d). (f) The definition of final SiO_2 layer with thickness of $t_d/2$.

First, a glass substrate was cleaned by ultrasonic bathing in acetone and propan-2-ol (IPA), each for 5 min (Figure 3.5 (a)). Then, the substrate was loaded into the evaporator and the deposition process started. The bottom SiO_2 layer with thickness of $t_d/2$ was defined (Figure 3.5 (b)), followed with the first Ag (Ge) layer with thickness of t_m and the second SiO_2 layer with thickness of t_d (Figure 3.5 (c) and (d)). After repeating the deposition of Ag (Ge)/SiO_2 bilayer several (e.g. 3,4,5) times (Figure 3.5 (e)), the top SiO_2 layer with thickness of $t_d/2$ was finally defined (Figure 3.5 (f)), and then the multilayer ENZ sample was fabricated.

3.3 Characterisation

3.3.1 Retrieval method

The optical characterisation here typically aims at obtaining the effective refractive index and permittivity of thin films (such as multilayer structures and their unit layers). To characterise these structures, we first tried a common approach, ellipsometry, which can retrieve the refractive index of a film based on the intensity and polarisation state of the reflected signals. However, due to having the near-zero permittivity and refractive index, ENZ film cannot be characterised correctly. Typically, the measured permittivity (real part) of film using ellipsometre cannot show the zero point.

In order to determine the effective permittivity of thin films, specifically the ENZ slab, we designed a retrieval method using measured transmission, reflection and thickness. This method considers the multilayer structure as a homogeneous slab and fitting the effective permittivity of an equivalent slab with an identical thickness that exhibits the same transmission and reflection. The detail of this method is presented in the following.

The fitting procedure is based on the Fresnel's law which will be first discussed here[80]. We consider a simple structure consisting two layers with refractive index of n_1 and n_2, respectively, shown in Figure 3.6 (a). A light wave with either p or s polarisation is shone from medium n_1 to medium n_2. The incident, reflected and transmitted angles are θ_{in}, θ_r and θ_t, respectively. The relationship of these angles can be describe as: $\theta_{in} = \theta_r$ and $n_1 \sin\theta_{in} = n_2 \sin\theta_t$. The reflection and transmission coefficients (r and t) can be obtained by Fresnel's equations, shown as[80]:

$$r_s = \frac{n_1 \cos\theta_{in} - n_2 \cos\theta_t}{n_1 \cos\theta_{in} + n_2 \cos\theta_t} \qquad t_s = \frac{2n_1 \cos\theta_{in}}{n_1 \cos\theta_{in} + n_2 \cos\theta_t} \tag{3.1}$$

$$r_p = \frac{n_2 \cos\theta_{in} - n_1 \cos\theta_t}{n_2 \cos\theta_{in} + n_1 \cos\theta_t} \qquad t_p = \frac{2n_1 \cos\theta_{in}}{n_2 \cos\theta_{in} + n_1 \cos\theta_t} \tag{3.2}$$

where p and s represent p and s polarisation, respectively.

For both polarisations, the reflectivity (R) can be calculated by squaring the magnitude of r_u, shown as

$$R = |r_u|^2 \tag{3.3}$$

whereas transmissivity (T) is obtained by

$$T = \frac{n_2 \cos\theta_t}{n_1 \cos\theta_{in}} |t_u|^2 \tag{3.4}$$

where $u = s, p$ represent the polarisation states.

Reflectivity and transmissivity represent the fraction of the incident power that is reflected and transmitted at the interface, so they are also known as the power reflection coefficient and power transmission coefficient, respectively. In measurement, reflectivity and transmissivity can be directly calculated using the reflected and transmitted intensities, and for convenience, "reflection" and "transmission" are used to represent the power reflection coefficient and power transmission coefficient in this thesis.

The absorption of the effective material can be described as

$$A = 1 - R - T \tag{3.5}$$

To simplify the calculation model and reduce the difficulty of measurement, we typically shone the light at normal incidence to the sample for characterisation, i.e. $\theta_{in} = \theta_r = \theta_t = 0$. Under this circumstance, the reflection and transmission coefficients of p and s polarised waves have identical magnitude (r and t) which are described as

$$r_s = -r_p = \frac{n_1 - n_2}{n_1 + n_2} = r, \qquad t_s = t_p = \frac{2n_1}{n_1 + n_2} = t \tag{3.6}$$

The reflectivity and transmissivity are thus simplified as

$$R = |r|^2, \qquad T = \frac{n_2}{n_1}|t|^2 \tag{3.7}$$

Then we extend the model into the multilayer model that we design to realise the ENZ condition. This structure is formed by N ($N > 2$) layers, sketched in Figure 3.6 (b). A light wave with a vacuum wavelength of λ is shone from the top at layer 1 and transmit through the whole structure and finally reach the layer N. We define that the direction of the incident wave (from top to bottom) is the forward direction (f) and the reverse direction is the backward direction (b).

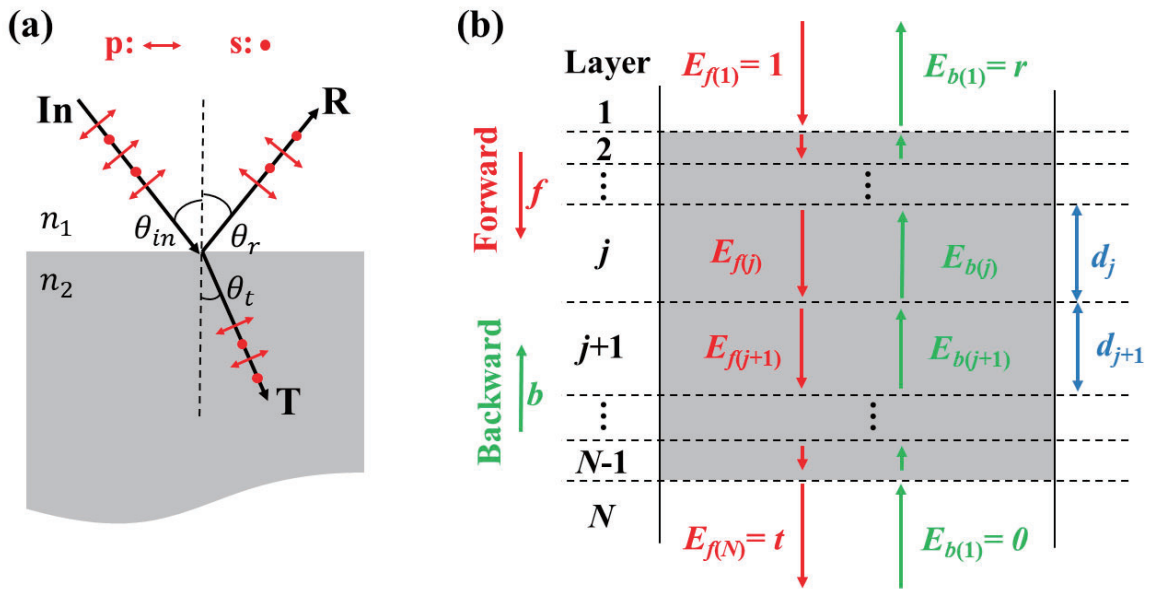

Figure 3.6: Sketches of the light-matter interaction models of the retrieval method. (a) The transmission (T) and reflection (R) of (s or p) polarised light at the interface between two media with refractive indices of n_1 and n_2. θ_{in}, θ_t and θ_r represent the angle of the incident, transmitted and reflected light, respectively. (b) The light wave with amplitude of E probing a multilayer structure at a normal incidence. f and b indicate the direction of forward and backward. The d_j means the thickness of layer j.

Inside the structure, layer j ($1 < j < N$) has a thickness of d_j and refractive index n_j. When the light wave propagates through the layer j, its phase changes, and the phase shift factor (δ_j) is defined as

$$\delta_j = d_j k = \frac{2\pi d_j}{n_j \lambda} \tag{3.8}$$

where k is the component of wave vector at the light propagation direction.

At the interface between layer j and $j+1$, the amplitude of the wave changes following the relationship shown as

$$E_{f(j+1)} = (E_{f(j)} e^{i\delta_j}) t_{j,j+1} + E_{b(j+1)} r_{j+1,j} \tag{3.9}$$

$$E_{b(j)} e^{-i\delta_j} = (E_{b(j+1)} t_{j+1,j} + (E_{b(j+1)}) e^{i\delta_j}) r_{j,j+1} \tag{3.10}$$

where, $E_f(u)$ and $E_b(u)$ are the amplitude of the wave propagating in layer u ($u = j, j+1$) at directions of forward and backward, respectively. $t_{u,v}$ and $r_{u,v}$ ($u, v = j, j+1$) represent the reflection

and transmission coefficients from layer u to layer v, and they follow the relationship of Equation 3.6, i.e. $r_{u,v} = -r_{v,u}$ and $t_{u,v}t_{v,u} - r_{u,v}r_{v,u} = 1$.

To simplify the calculation procedure of multilayer structure, we restructure and combine Equations 3.9 and 3.10 into matrix format, described as

$$\begin{pmatrix} E_{f(j)} \\ E_{b(j)} \end{pmatrix} = M_j \begin{pmatrix} E_{f(j+1)} \\ E_{b(j+1)} \end{pmatrix} \tag{3.11}$$

where M_j is defined as ($j = 2, 3, \ldots, N-1$)

$$M_j = \frac{1}{t_{j,j+1}} \begin{pmatrix} e^{-i\delta_j} & 0 \\ 0 & e^{i\delta_j} \end{pmatrix} \begin{pmatrix} 1 & r_{j,j+1} \\ r_{j,j+1} & 1 \end{pmatrix} \tag{3.12}$$

Considering the whole multilayer model, we let the amplitude of the incident wave as 1, i.e. $E_{f(1)} = 1$, and the final reflected and transmitted waves have the amplitudes of $E_{b(1)} = r$ and $E_{f(N)} = t$, respectively. There is no incident wave from the bottom layer (N), so $E_{b(N)} = 0$. Therefore, the r and t follow the relationship of

$$\begin{pmatrix} 1 \\ r \end{pmatrix} = \tilde{M} \begin{pmatrix} t \\ 0 \end{pmatrix} \tag{3.13}$$

where $\tilde{M}$ is described as

$$\tilde{M} = \frac{1}{t_{1,2}} \begin{pmatrix} 1 & r_{1,2} \\ r_{1,2} & 1 \end{pmatrix} M_2 M_3 \ldots M_N = \begin{pmatrix} \tilde{M}_{11} & \tilde{M}_{12} \\ \tilde{M}_{21} & \tilde{M}_{22} \end{pmatrix} \tag{3.14}$$

By combining Equations 3.13 and 3.14, we obtain the reflection and transmission coefficients which are given by[80]

$$r = \frac{\tilde{M}_{21}}{\tilde{M}_{22}} \qquad t = \frac{1}{\tilde{M}_{11}} \tag{3.15}$$

For multilayer structure with given thickness and refractive index of each unit layer, we can numerically simulate reflection (R) and transmission (T) using Equations 3.6 - 3.8 and 3.12 - 3.15.

For the unknown film, this method offers an approach to retrieve the effective refractive index with the following procedures. First, we determine the R and T at normal incidence by optical measurement. The total thickness of the structure is measured typically using a surface profiler. Second, we consider this light propagation model (refer to Figure 3.6 (b)) as a three-layer structure, i.e. air/film/air or air/film/substrate (if the thickness of the film is far less then the thickness of

its substrate). The effective reflection (R_{eff}) and transmission (T_{eff}) are calculated using the fitted effective refractive indices and measured thickness. At a reasonable range of fitted refractive index, all the calculated R_{eff} and T_{eff} are compared with the measured R and T. The fitting process can be done by computer and finally we can determine the best-fitting effective refractive index (n_{eff}) of the film. The effective permittivity can be then obtained by $\epsilon_{eff} = \sqrt{n_{eff}}$.

This retrieval method is designed for the incoherent light, as the coherent light will cause the unexpected oscillation at the transmission and reflection spectra. Besides, the thickness of the structure should be within a sub-wavelength scale to meet the requirement of EMT and avoid the oscillation in spectra as we discussed in Chapter 2.

3.3.2 Characterisation of unit layers

The setup for optically characterisation is sketched in Figure 3.7. To characterise the optical properties of the Ag and SiO_2 layers, and also multilayer structures, a W halogen light source (Ocean Optics) was used to probe samples at normal incidence with s polarisation. A collimation system (formed with two coupled lenses) and an adjustable diaphragm were used to control the beam profile of the input light. A beam splitter (BS) was placed beneath the sample to guided the reflected light. The transmitted and reflected signals were collected and spectrally analysed with two spectrometers (Ocean Optics USB 2000 + VIS-NIR-ES, 350–1000 nm). This setup has already been built by our group members, but I have also developed this apparatus and built new setups following same optical rules for other optical measurements in my further works, for example, the characterisation of ITO at NIR range.

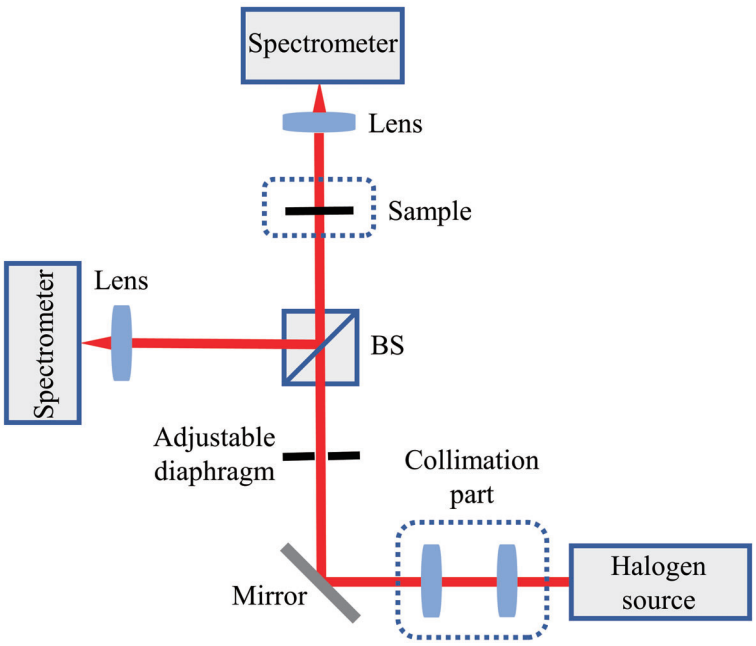

Figure 3.7: The digram of the optical path for measuring membranes, formed with the light input part (W halogen source, collimation part and diaphragm), sample and signal collection parts (transmission and reflection).

For every measurement, the transmitted and reflected signals were first collected, followed with the collection of the corresponding reference signals, i.e. the light intensities transmitted through the air and reflected from an Ag mirror (Thorlabs). The Ag mirror was not ideal for detecting the real reflection but had an average reflection of more than 95% in the visible range, which was enough for the requirement of our measurement. Due to this, our measurement had an estimated uncertainty of 1%. The transmission (T) and reflection (R) were obtained by dividing the transmitted and reflected by the related reference intensities.

Prior to the optical characterisation, the sample thickness was determined using a Dektak Surface Profiler (Veeco). For example, to determine the thickness thin Ag film, we first covered part of substrate (e.g. glass) during the evaporation process, and then scanned across the edge between Ag layer and substrate using the surface profiler to obtain the thickness of the Ag film.

Using the data of T, R and sample thickness, the effective refractive index (n) and extinction coefficient (k) were retrieved, thus the effective permittivity (ϵ, complex) was also obtained via the relationship of $\epsilon = (n + ik)^2$.

Before fabricating and chartering the multilayer ENZ structure, we needed to first determine the optical properties of unit layers, i.e. Ag and SiO_2 layer because the thin films do not behave like

the bulk materials. The Ag films (6nm) with and without Ge layer were characterised first, using the setup shown in Figure 3.7. The measured transmission and reflection are shown in Figure 3.8. The transmission of Ag (Ge) sample is about 40% higher than the one of Ag sample at the visible wavelength range. The reflection values of both samples were very close, but the Ag sample reflects more light at short wavelength range, compared to the Ag (Ge) sample.

The high transmission and low reflection of Ag film are due to the high scattering. As we discussed in the fabrication section, the cracks and roughness on the surface of the Ag thin film with the size of about 50 nm scatter the light with the wavelength of around 500 nm most, according to the Rayleigh scattering mechanism. The light scattered in wide direction range and most of them cannot be collected by the spectrometer in our apparatus. Hence the reflection of Ag sample decreased dramatically. This phenomena also verified our discussion about the high scattering effect of the rough surface the Ag sample in the fabrication section.

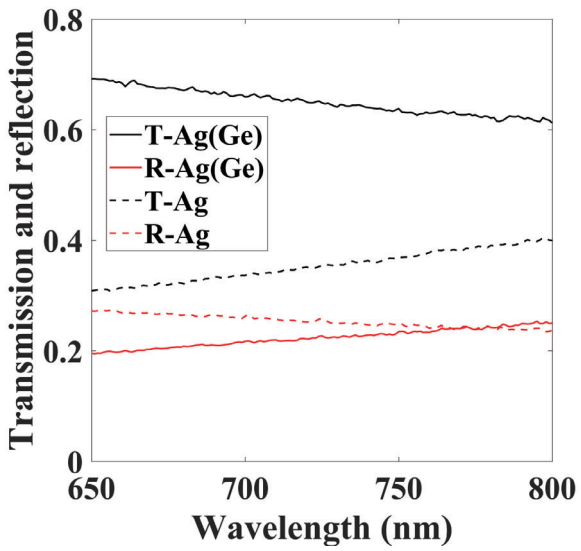

Figure 3.8: Measured transmission (T) and reflection (R) of the 6-nm Ag samples with and without the Ge wetting layer, respectively.

Figure 3.9 shows the retrieved permittivity and refractive index of the Ag (Ge) sample, using the measured values of T and R shown in Figure 3.8. The reference refractive index of Ag thin films [66] is shown in Figure 3.9 (b) and it fit the measured value in acceptable range. Additionally, we can see that the thin-film Ag exhibits different optical responses compared to bulk Ag.

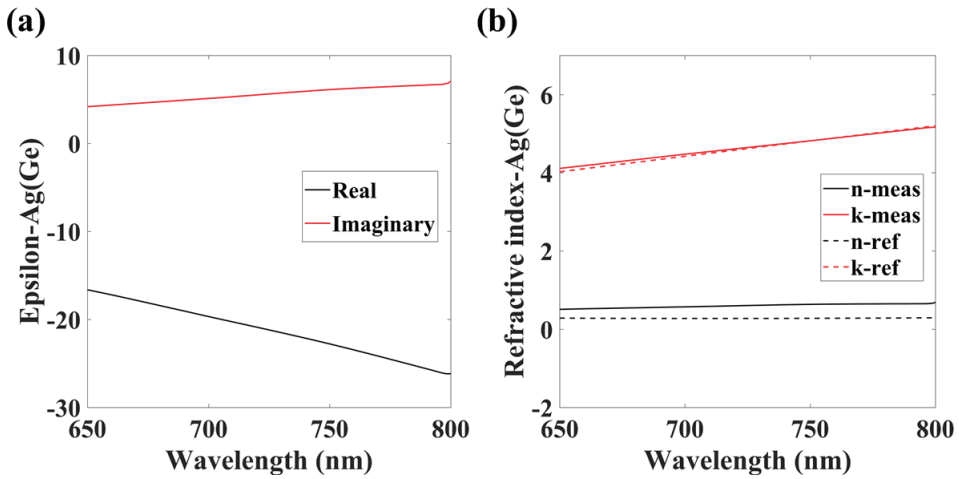

Figure 3.9: Optical characterisation results of the Ag (Ge) sample based on the transmission and reflection shown in Figure 3.8. (a) The retrieved epsilon (real and imaginary parts) of the sample. (b) The retrieved refractive index (n-meas and k-meas) of this sample, compared with literature reference values (n-ref, k-ref)[66].

The SiO_2 unit layer (60nm) was then characterised using the same approach. Figure 3.10 shows the high transmission (>90%), and low reflection (<10%) of the SiO_2 layer, and indicates that the loss of the layer is negligible, as we expected.

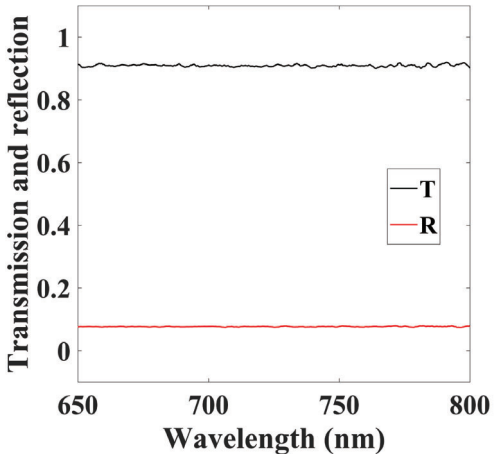

Figure 3.10: Measured transmission (T) and reflection (R) of the 60-nm SiO_2 layer deposited on a glass substrate.

The retrieved permittivity and refractive index of the SiO_2 layer are shown in Figure 3.11. The refractive index of the SiO_2 film is characterised as a value of about 1.5 at the visible range and fit the reference value[101] reasonably well.

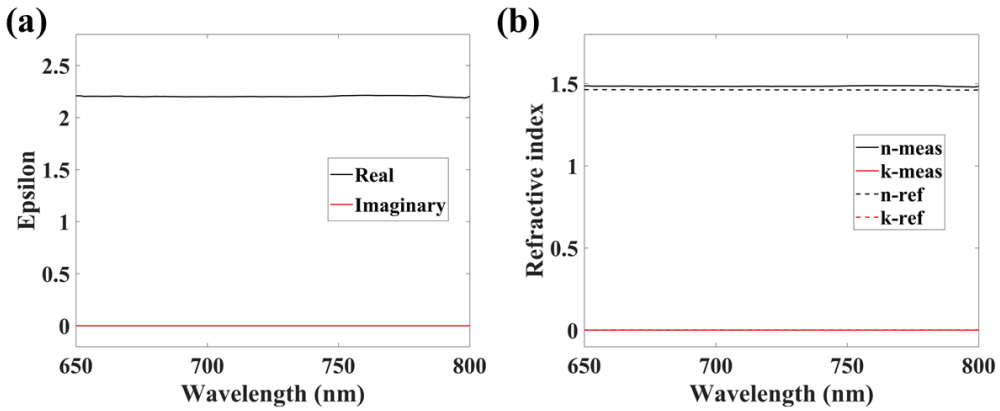

Figure 3.11: The retrieved epsilon (a) and refractive index values (b) of the SiO_2 sample shown in Figure 3.10, compared to the reference refractive values (n-ref, k-ref)[101].

3.3.3 Characterisation of multilayer ENZ structures

In order to verify the applicability of EMT to multilayer structures, we fabricated 3-, 4-, 5- and 6-bilayer ENZ films on glass substrates, formed by the 6-nm Ag (Ge) and 60-nm SiO_2 unit layers. The measured transmission and reflection of these samples are displayed in Figure 3.12.

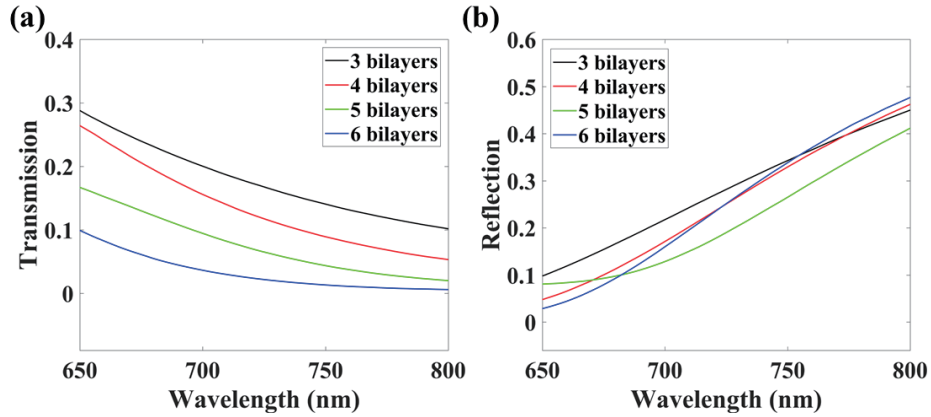

Figure 3.12: The measured transmission (a) and reflection (b) curves of 3-, 4-, 5- and 6-bilayer ENZ samples.

Along with the number of bilayers increasing from 3 to 6, the average transmission decreases by about 15%, while the reflection does not change much in general. The change of transmission is related to the increase of both the loss and reflection when the number of Ag layer increase. This complicated relationship cannot be determined directly by comparing the transmission and reflection curves. Therefore, we retrieve the permittivity (real and imaginary parts) of these samples and

present the values in Figure 3.13.

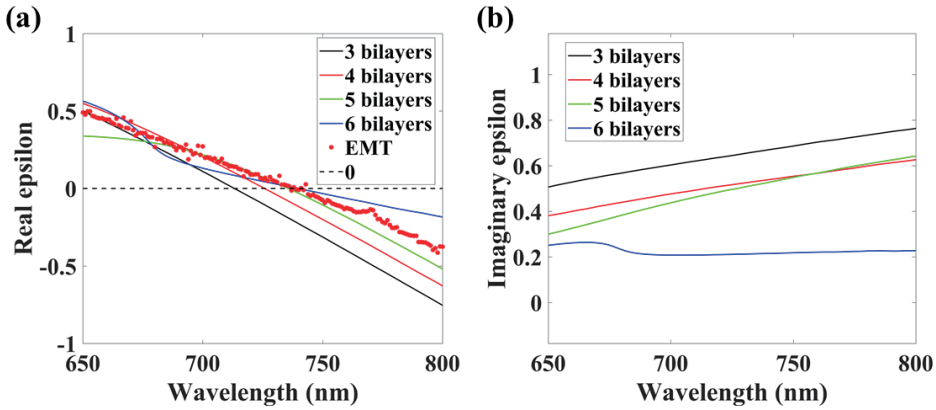

Figure 3.13: Real (a) and imaginary (b) parts of retrieved epsilon of different ENZ samples (3-, 4-, 5- and 6-bilayer) based on the transmission and reflection results shown in Figure 3.12.

By comparing the real epsilon of these ENZ samples (Figure 3.13 (a)), we found that the curves tend to converge and the zero permittivity wavelengths are approaching 748 nm, along with the increasing of the number of bilayer. Additionally, based on the EMT ($\epsilon_{eff} = (\epsilon_m t_m + \epsilon_d t_d)/(t_m + t_d)$), the effective epsilon (real part) are calculated using the parameters of the characterised Ag (Ge) and SiO_2 unit layers and shown in Figure 3.13 (a) as well. The real epsilon of 5- and 6-bilayer sample approach the values calculated using EMT method. Hence, the EMT works well for 5- and 6-bilayer structure to achieve the ENZ condition.

Figure 3.13 (b) showed the retrieved imaginary part of 3-, 4-, 5- and 6-bilayer ENZ samples, which decreased along with the increasing of the number of bilayers.

The 6-bilayer sample showed oscillations in the curves of permittivity (both real and imaginary parts), which was predicted in Chapter 2. Therefore, the 5-bilayer sample was enough to be used as the ENZ MM.

To verify the reliability of the 5-bilayer Ag (Ge)/SiO_2 structure, we did the numerical simulation of the transmission, reflection and absorption of this structure using the multilayer model shown in Figure 3.6 (b). The calculation results (T_c, R_c and A_c) show an acceptable fitness to the measured T_m, R_m and A_m. The slight difference between experimental and numerical results could be explained by the roughness of the multilayer structure during fabrication.

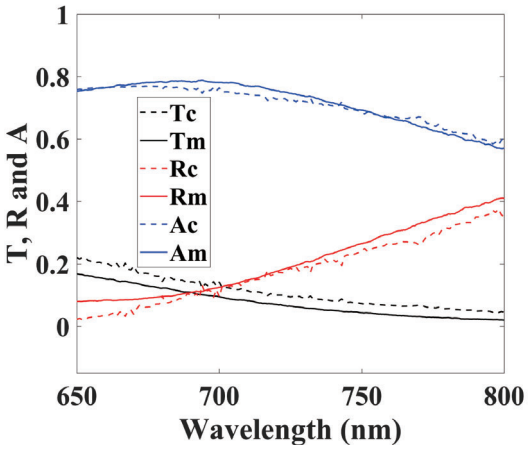

Figure 3.14: Transmission (T), reflection (R) and absorption (A) of the 5-bilayer Ag (Ge)/SiO_2 ENZ sample in measurement (Tm, Rm, Am) and calculation (Tc, Rc, Ac) using measured values of refractive index of Ag (Ge) and SiO_2 unit layers shown in Figure 3.9 and 3.11.

Furthermore, by modifying the thickness of the SiO_2 unit layer (t_d), we were able to manipulated the ENZ range of this Ag/SiO_2 multilayer structure. Figure 3.15 presented the retrieved permittivity of the 5-bilayer ENZ structure with the thickness of SiO_2 unit layer varied as 50, 60 and 70 nm. The related real part of the effective permittivity reached zero at the wavelength of about 650, 745 and 850 nm, respectively. These samples were designed to enhance the emission of QDs, and the result would be presented in the following section.

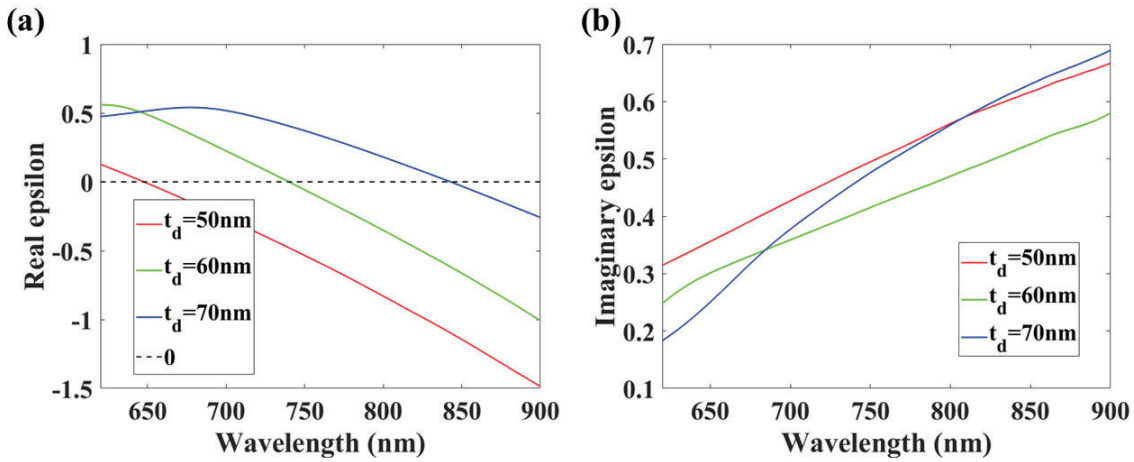

Figure 3.15: Real (a) and imaginary (b) parts of 5-bilayer ENZ samples formed by 6-nm Ag unit layer and SiO_2 unit layer with different thickness (t_d).

3.4 Emission enhancement on ENZ substrates

This section presents the work of ENZ substrates enhancing the emission of QDs, both numerically and experimentally.

Due to the vanishing permittivity and refractive index, the ENZ MMs are considered as optically "thinner" media compared to most natural materials, e.g. air. Hence, the total reflection occurs when light probes from air to ENZ media. This effect motivates the development of emission enhancement using ENZ substrates. Here, we used semiconductor emitters, such as QDs[102], as light emitters and managed to modify their emission properties using ENZ substrates.

QDs are nanoscale semiconductor crystals whose carriers are imprisoned in three spatial directions. The emission properties of QDs originate from the fluorescence phenomenon of bulk semiconductors and are controlled by the quantum confined effect[103]. Figure 3.16 sketches the different distribution of energy levels in bulk semiconductors and QDs.

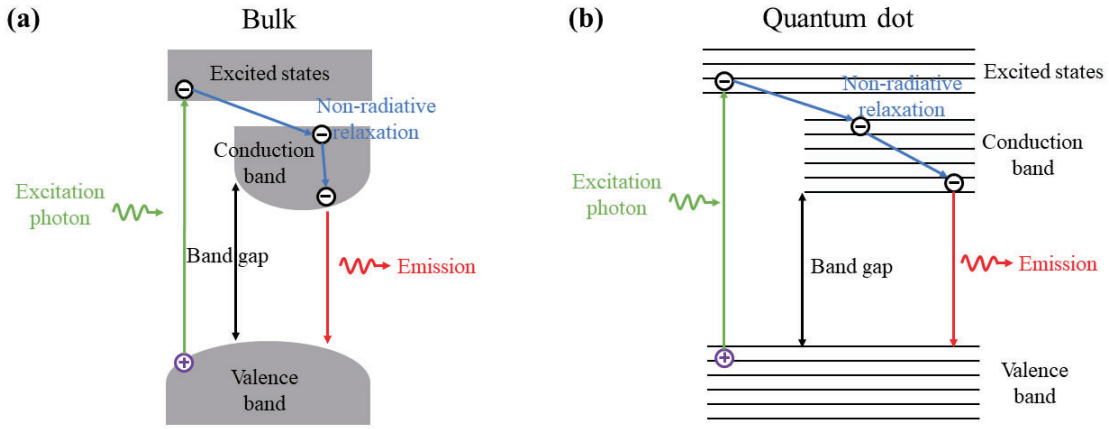

Figure 3.16: Sketches of energy levels and fluorescence processes in bulk semiconductors (a) and QDs (b).

To understand the mechanism of the emission of QDs and also the fluorescence of semiconductors, we first review several concepts, such as energy level, bandgap and density of states, etc.

Inside a semiconductor or insulator, electrons are confined to different bands of energy, and forbidden from other regions. Typically, valence band and conduction band are two states we focused on. If electrons are all stay at the valance band, they cannot move free inside the material, and thus the material is non-conductive in macroscopic. If some electrons jump to the conduction band, the material is conductive as these electrons are free to move within the material and serve as a charge carrier to conduct electric current. No electron states can exist between the valence band

and conduction band, and these regions are called bandgaps. Electrons can jump from one band to another, for example, from a valence band to a conduction band, which requires specific amount of energy. The required energy differs with different materials and also have different sources, such as phonons or a photons. Additionally, conductors, e.g. metals, have very small or no bandgaps due to the overlap between the valence and conduction bands.

Considering the bulk semiconductors, the carriers (electrons) inside them can jump from valence band to conduction band by absorbing excitation photons and jump back to valence band with emitting lower-energy photons (Figure 3.16 (a)). Due to the relatively large spatial size and carrier number, compared to the microscopic world, bulk semiconductors have continuous valence band and conduction band, and thus their emission spectra are broadband. However, due to the size limitation, the quantum effect appears in QDs, i.e. the energy levels become discrete (Figure 3.16 (b)). This effect leads to the narrowband emission spectra of QDs.

Generally, the emission efficiency of semiconductors is determined by their density of states, viz. the number of energy levels in unit energy range. Figure 3.17 sketches the density of states of semiconductors changes along with the decreasing of spatial dimensions and sizes.

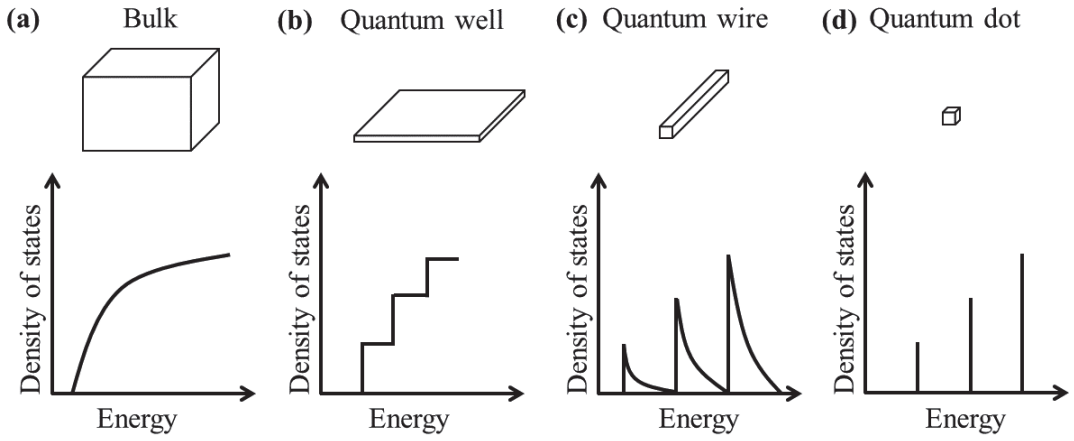

Figure 3.17: The density of states of semiconductors in different dimensions.

By compressing bulk semiconductors into nanoscale in only one dimension (direction), the quantum wells are obtained. They are the most common 2D semiconductor materials, especially in the field of emitting lasers[104]. Quantum wells have macroscopic dimensions in two dimensions, while the third dimension is about 10 nm large. The carriers in quantum wells move in two dimensions similar to the bulk material, and is limited by the boundary barrier in the third dimension, thus forming quantized energy level. Therefore, the density of states of quantum wells presents a stepped

shape (Figure 3.17 (b)). Similarly, quantum wires represent the 1D semiconductors whose carrier movement limited in two dimensions, and their density of states is further compressed and has singularities at the energy threshold positions (Figure 3.17 (c)).

QDs are considered as the zero-dimensional (0D) materials as their sizes in three dimensions are all less than 100 nm. The quantum confined effect in three dimensions leads the discrete energy level which similar to the structure of atoms or molecules[105]. The density of states of QDs is also similar to the discrete linear absorption or emission peaks in atoms (Figure 3.17 (d)), so the QDs are also known as "artificial atoms". Due to the minimal size, QDs have much higher density of energy levels, compared to bulk materials, so their radiation transition intensity is greatly enhanced. These peculiar characteristics, i.e. high stability, narrowspectral linewidth and short radiative lifetime, make QDs excellent candidates for quantum light emitters at the single photon level[106, 107].

Here, we propose and demonstrate an approach to enhance the emission properties of GaAs QDs using the multilayer Ag/SiO_2 ENZ MMs we developed in Figure 3.15.

The GaAs QDs are embedded in semiconductor nanowires (NWs), typically, core-shell GaAs/aluminium gallium arsenide (AlGaAs) NWs[108]. Semiconductor NWs are promising platforms for hosting and optoelectronic manipulating QDs because of their high crystalline quality and integration possibilities[109]. In addition, NWs and QDs can be fabricated successively using molecular beam epitaxy (MBE) approach[110]. Generally, MBE process takes place in ultra-high vacuum, based on vapor-liquid-solid (VLS) mechanism[111, 112]. Gaseous elements (atoms and molecules) condense on monocrystal substrates and form the desired solid structures layer by layer. This method ensure the high purity and crystalline quality.

The samples of GaAs QDs embedded in GaAs/AlGaAs NWs were prepared and provided by our collaborators, Dr Zhang-Kai Zhou and Dr Ying Yu from the School of Physics and Engineering, Sun Yat-sen University, Guangzhou, China.

3.4.1 FDTD modelling of emission enhancement

The simulation work was done using Finite-Difference Time-Domain (FDTD) method with a commercial software, Lumerical FDTD Solutions. The FDTD approach differentiates Maxwell's equations in time and space, and then calculates alternately the electric field and magnetic field in the space domain by using the leapfrog algorithm[113]. The changes of electromagnetic field are simulated by updating the time domain to achieve the purpose of numerical calculation. This method, i.e. leapfrog algorithm, first solves the electric field vector components in a volume of space at a given

instant in time, and then solves the magnetic field vector components in the same spatial volume at the next instant in time. This leapfrog process is repeated over and over again until the desired transient or steady-state electromagnetic field behaviour is fully evolved.

The advantage of FDTD method is that it can directly simulate the distribution of the electromagnetic field with high precision, which is one of best methods for the numerical simulation in optics. Besides, because it is a time-domain method, FDTD approach is capable to cover a wide wavelength range with a single simulation run, and thus it is suitable for our purpose to calculate the ENZ region of the multilayer structure.

To analyse specific problems with FDTD method, we need consider the geometric parameters, material parameters, computational accuracy, computational complexity and computational stability of the research object. Typically, as FDTD process requires that the entire computational domain should be gridded, and the grid spatial discretisation must be sufficiently fine to resolve both the smallest electromagnetic wavelength and the smallest geometrical feature in the model. In the numerical model used here, the ENZ condition was achieved using 5-bilayer Ag/SiO_2 structure with the same parameters, sketched in Figure 3.1. The Ag unit layer had a thickness (t_m) of 6 nm. The thickness of SiO_2 (t_d) was variable, at three values (50, 60 and 70 nm), to achieve different zero-permittivity wavelength. The grid sizes of each unit layers are designed to be smaller than thickness and also the wavelength. For example, the grid size inside the 6-nm Ag unit layer is 2 nm. The refractive indices of Ag and SiO_2 conformed to References [114] and [67]. Additionally, to make the multilayer structure symmetry, top and bottom layers were all SiO_2 films with a thickness of half t_d.

The ENZ structures were probed with plane waves to characterise the ENZ region. The plane waves had a wavelength with the range from 500 to 900 nm and the step size of 1 nm. The transmission and reflection signals were collected and used to retrieve the effective permittivity. The real and imaginary parts of the retrieved permittivity are shown in Figure 3.18.

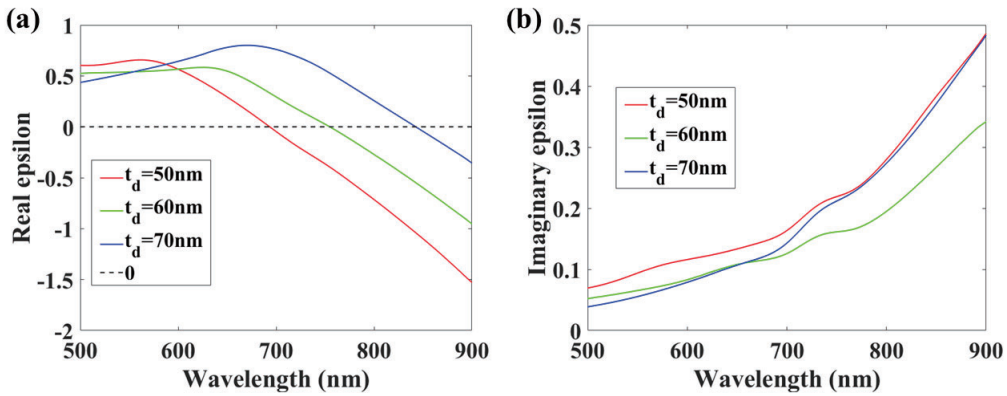

Figure 3.18: Real (a) and imaginary (b) parts of retrieved effective permittivity (epsilon) of ENZ structures with different thickness of SiO_2 unit layers (t_d), based on the calculated transmission and reflection using FDTD approach.

Figure 3.18 (a) presents that the zero-permittivity (real) wavelength increases along with the increasing of thickness of SiO_2 unit layer. This makes it possible to test the influence of different ENZ substrates on the quantum dot (QD) emission. Figure 3.18 (b) indicates that the imaginary part of permittivity of three models are very similar and all increasing at longer wavelength range. By comparing Figure 3.15 (a) and Figure 3.18 (a), we can find that the fabricated ENZ samples have similar real epsilons and ENZ ranges to the numerical results. Additionally, the imaginary epsilon exhibit lower values (Figure 3.18 (b)) than the results of real samples (Figure 3.15 (b)), which is mainly due to the ultra-thin Ag layer showing higher optical losses, compared to bulk Ag we used in FDTD models.

Considering the enhancement of emission on ENZ substrates is due to the mechanics similar to the total reflection as discussed in Chapter 2, we calculated the effective refractive index (n) using the real and imaginary parts shown in Figure 3.18 and plot the absolute n of different ENZ structures in Figure 3.19.

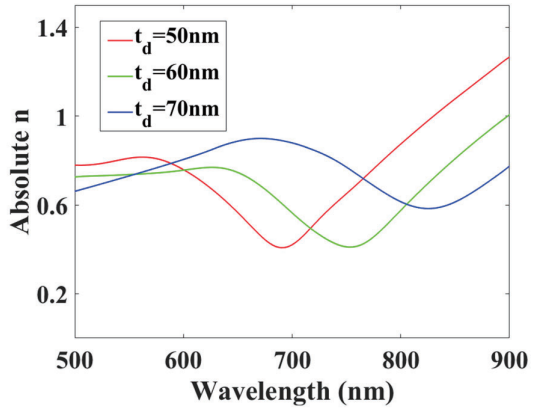

Figure 3.19: Calculated refractive index (absolute value) of different ENZ structures based on the permittivity shown in 3.18. The absolute n shows the minimum value at different wavelengths according to the changing thickness of SiO_2 unit layers (t_d).

The absolute value of the refractive index shows a minimum value due to the ENZ effect. The absolute n moves toward the minimum value at longer wavelength range along with the increasing of the thickness of SiO_2 unit layers. Because the optical loss, which related to the imaginary permittivity, cannot be ignored, the minimum value of the refractive index is positive and cannot reach zero as we expected. Besides, the zero permittivity and minimum refractive index occur at almost the same wavelength range, indicated in Table 3.1 and this agreement allows us to use the ENZ region to represent the minimum-n range.

t_d	Zero-ϵ wavelength	Minimum-n wavelength
50 nm	~693	~691
60 nm	~755	~754
70 nm	~843	~826

Table 3.1: The comparison of the zero-ϵ and minimum-n wavelengths in ENZ structures containing 6-nm Ag unit layer and SiO_2 unit layer with different thickness (t_d).

Here, in the FDTD model, we changed the plane waves with electric dipoles which exhibited similar emission behaviour to QDs. The dipoles were placed exactly on top of ENZ structures (Figure 3.20 (a)) and their reflection signals are collected and spectrally analysed (Figure 3.21 (a)). In addition, to investigate the effect of ENZ substrate, compared to standard mirror, i.e. the dielectric/metal bilayer structure, a control model (SiO_2/Ag structure) was settled (Figure 3.20 (b)). In the mirror model, Ag layer had a thickness of 30 nm, which is the sum of the thickness of Ag layers in the 5-bilayer Ag/SiO_2 ENZ model. The thickness of SiO_2 layer (t_d) varied at 0, 50, 100 and 120 nm.

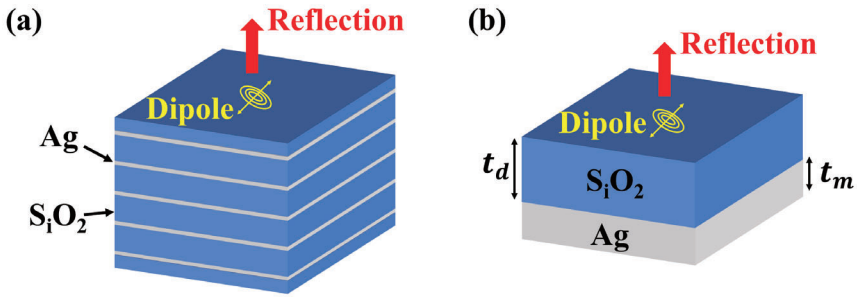

Figure 3.20: Diagrams of electric dipoles locating on top of multilayer Ag/SiO_2 ENZ structure (a) and bilayer SiO_2/Ag mirror slab (b). The reflection signals of dipoles were collected.

Figure 3.21 (a) indicates that the reflection of the dipole emission is increased by about 200% at ENZ ranges, compared to non-ENZ ranges. The spectral range of enhancement conforms the ENZ region and varies with the changing of zero-permittivity wavelength. The mirror structure showed higher reflection at broad wavelength range, compared to the multilayer structure, and the highest transmission region changed along with the variation of the thickness of the top SiO_2 layer (Figure 3.21 (b)). This is due to the SiO_2 layer protect the electromagnetic waves from shorting out by the metal (Ag) layer[115, 116]. The high reflection of the mirror occurs in broadband, and this is not applicable for the applications that need narrow-band pumping, such as lasing[117–119]. The emission enhancement just around the ENZ range is more suitable in this case.

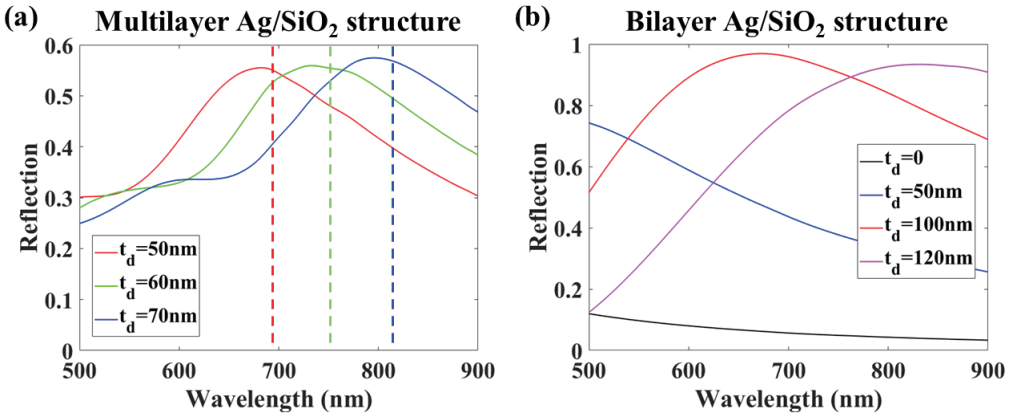

Figure 3.21: Numerical signals of reflection of ENZ (a) and bilayer SiO_2/Ag mirror (b) slabs with different thickness of SiO_2 layers. The vertical dashed lines in (a) represent corresponding zero-permittivity wavelengths.

3.4.2 Fabrication

Our collaborators prepared and provided the NWs samples, and the fabrication and transfer processes were illustrated in Figure 3.22.

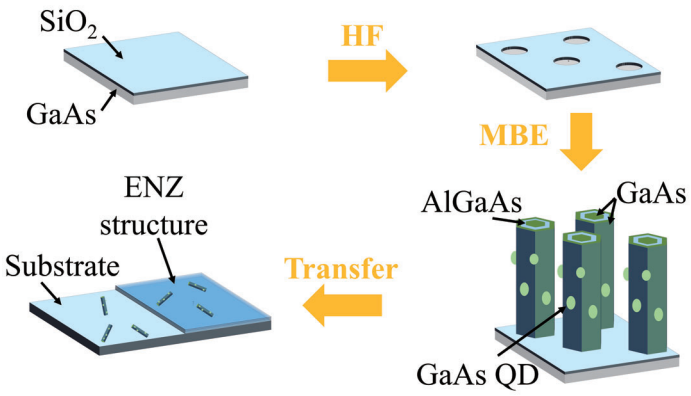

Figure 3.22: Sketch of the fabrication and transfer processes of GaAs QDs and GaAs/AlGaAs NWs. QDs and NWs are first deposited using MBE method then transferred directly to the top of ENZ membrane and other substrates (e.g. glass).

First, the GaAs QDs and their hosts, core-shell GaAs/AlGaAs NWs, were fabricated on GaAs (001) substrate using MBE method formed by two steps: pretreatment and deposition.

The GaAs substrate was pretreated by first sputter-coating a 15 nm SiO_2 layer and then immerging in 10% hydrofluoric acid (HF) aqueous solution for 2 s to create randomly distributed vacancy spots for the MBE growth. After that, the substrate was loaded into the MBE chamber (Veeco Mod Gen-II) which was then pumped into 10^{-8} Torr. The last procedure before growth was that the substrate was degassed for 10 min at 700 °C.

The deposition process took place at the pressure of about 10^{-6} Torr and started from covering the vacancy spots with 1 nm sized gallium (Ga) droplets. Then, the GaAs cores started growing vertically. When the cores reached the designed length of 3.5 µm, the vertical growth was stopped by depositing Ga droplets again, which also triggered the lateral growth of GaAs cores. As soon as the width of cores reached 200 nm, the other two $Al_{0.7}Ga_{0.3}As$ barrier shells with thickness of 200 nm were deposited to cover the GaAs cores, and the GaAs QDs grew between them, laterally on the facet of the NWs. Finally, the core-shell GaAs/$Al_{0.7}Ga_{0.3}As$ NWs embedding GaAs QDs were coated with another 60-nm GaAs layers to protect the QDs, typically against oxidation.

After deposition, the NWs embedding QDs can be transferred from GaAs substrate to other structures or devices via direct-contact method. For instance, the NWs will located randomly onto

target substrates (e.g. ENZ and glass slabs) after the contact with the GaAs directly. This procedure is sketched in Figure 3.22 as well.

Figure 3.23 (a) presents the SEM image of a GaAs/AlGaAs nanowire (NW) transferred on top a silicon (Si) substrate and points out the location of GaAs QDs. Figure 3.23 (b) shows a GaAs/AlGaAs NW lying on an ENZ substrate.

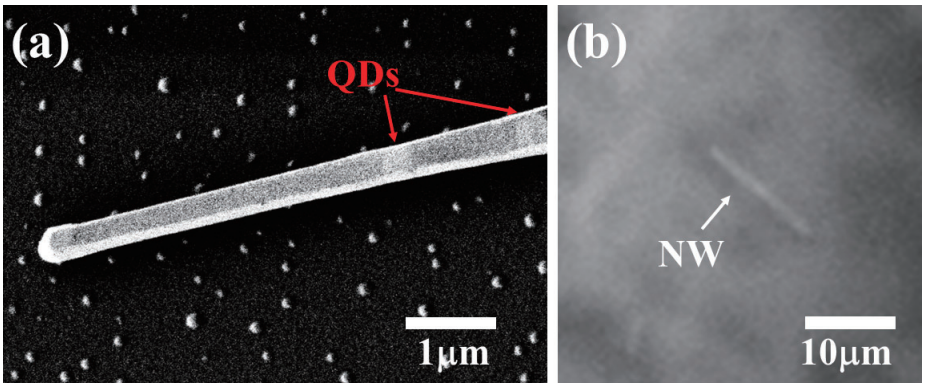

Figure 3.23: SEM image of a GaAs/AlGaAs NW hosting GaAs QDs.

To investigate the influence of ENZ substrate on the emission of GaAs QDs, we managed to transfer the NWs onto glass and ENZ substrates. The ENZ structures are identical to the FDTD models presented in Figure 3.20 (a), i.e. the Ag/SiO_2 multilayer structure with $t_m = 6\,\text{nm}$ and $t_d = 50, 60, 70\,\text{nm}$. The SiO_2 and Ag layers were fabricated using e-beam evaporation approach. Before the evaporation of the multilayer structure, another piece of glass was firmly covered on half of the glass substrate. Therefore, after deposition and removing the top glass sheet, the sample contained both ENZ structure and control group (glass) was obtained (Figure 3.24). Benefit from this kind of sample, we transferred NWs onto ENZ structure and glass sheet at the same time. The ENZ condition of these three samples were characterised as shown in Figure 3.15.

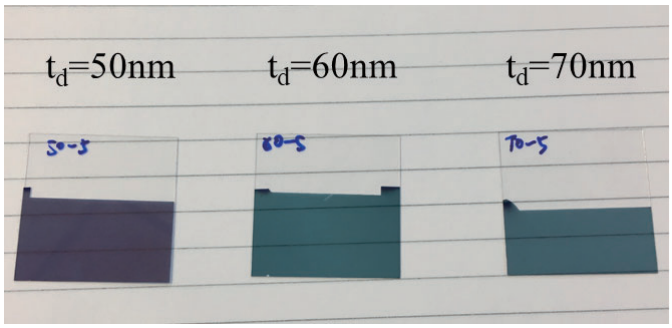

Figure 3.24: Photographs of ENZ samples with different thickness on glass substrates.

3.4.3 Results

The GaAs/AlGaAs NWs embedding GaAs QDs were transferred onto the ENZ sample with $t_d = 60\,\text{nm}$ and also glass substrate. Then the sample was mounted in an optical microscopy cryostat (Montana) at cryogenic temperatures of 3.4 K[120] and excited with a continuous-wave (CW) laser with wavelength of 405 nm (Figure 3.25).

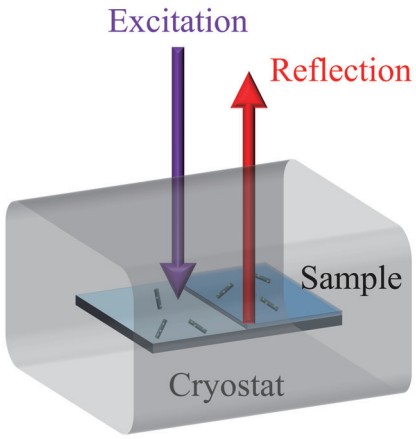

Figure 3.25: Diagram of the optical microscopy cryostat used to exciting QDs and collecting reflection (emission) signals.

The reflection (emission) signals of QDs on ENZ sample and glass substrate were collected and spectrally analysed. Figure 3.26 shows a typical result of the reflection comparison on different substrates. The reflection of QD emission is enhanced by about 10 times near the zero-permittivity wavelength range (around 740 nm).

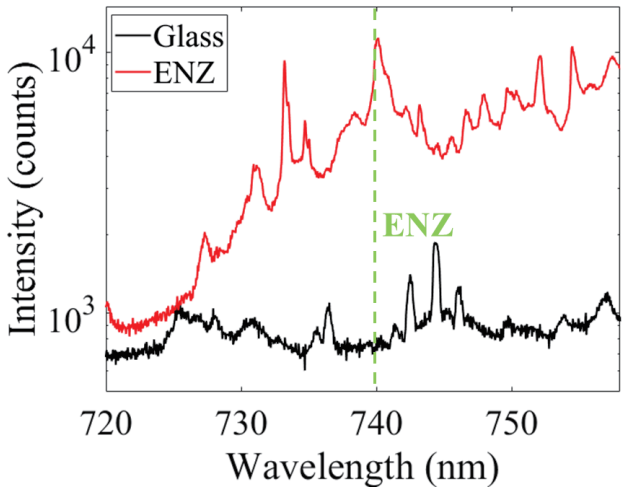

Figure 3.26: The comparison of the reflection signals of QDs located on the ENZ structure and glass substrate.

We collected plenty of reflection signals of NWs located both on the ENZ structure and glass substrate and analysed the intensity of emission peaks as a function of wavelength. The statistical result (Figure 3.27) shows that the ENZ structure greatly enhances the reflection of QD emission at the entire collection wavelength range (ENZ range). However, the influence at the non-ENZ region cannot be obtained here and needs more investigation.

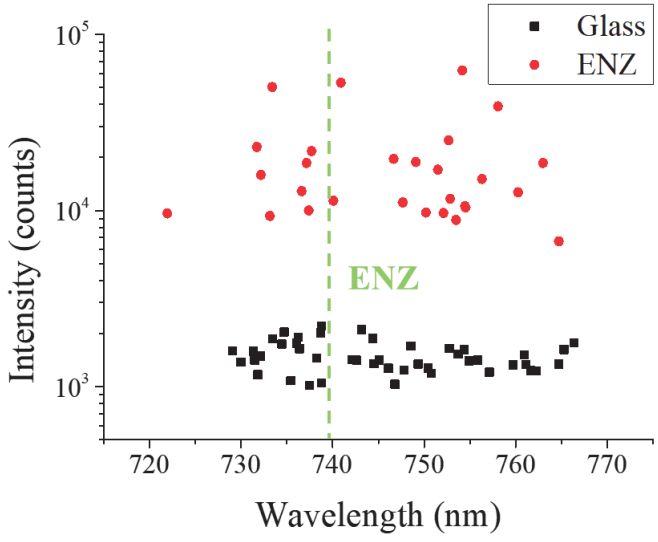

Figure 3.27: Statistic analysis of the reflection signals of QDs located on the ENZ structure and glass substrate. The vertical dashed line represent the zero-permittivity wavelength.

3.4.4 Discussion and further perspective

GaAs QDs embedded in GaAs/AlGaAs NWs are good candidates for illumination applications. Here, we demonstrated that the ENZ substrates enhanced the QD emission in a way similar to total reflection. At the interface of air/ENZ structure, the ENZ media are optically thinner than air, therefore, most emission energy is reflected into the air side.

The numerical results proved this effect by comparing the reflection signal of the emission of an electric dipole at ENZ and non-ENZ ranges. The experimental design combined the GaAs QDs with ENZ substrates. By comparing the reflection signal of QDs located on ENZ structure and the glass substrate, we found that the ENZ substrate enhanced the QD emission dramatically, by about 2 magnitudes at the ENZ range with low optical loss. The statistical analysis verified this as well. However, due to the narrow spectral range in measurement, the comparison between ENZ and the non-ENZ region is not shown. Hence, in further works, the broadband spectral measurement and analysis are required. Additionally, the other emitting materials, such as colloidal QDs and micro-disk emitters, can also be invested combined with ENZ media.

3.5 Conclusion

Here we demonstrated an approach to fabricating multilayer ENZ structure formed by Ag and SiO_2 sub-wavelength layers, using e-beam evaporation method. By determining the thickness of Ag and SiO_2 unit layers as 6nm and 60nm, respectively, we achieved the ENZ condition at the wavelength of about 748nm. Additionally, with the help of Ge wetting layer, the ultra-thin Ag layer exhibited high smoothness and low scattering effect. This also reduces the total loss of the ENZ multilayer structure. The ENZ samples with different bilayer numbers show different optical responses. By comparing the numerical calculation based on EMT with the measured results, we found that the 5-bilayer structure achieved the ENZ condition reliably and also showed a relatively low loss.

We built a multilayer light-matter interaction model based on Fresnel's equations, to realising the numerical simulation of the multilayer structure and the optical characterisation (retrieval) of fabricated samples. This approach benefits the process of designing and characterising ENZ MMs and also the theoretical verification of experimental measurement.

Furthermore, we have demonstrated an approach to enhance the emission properties of semiconductor QDs, based on the ENZ substrate defining. The numerical results predicted that the emission of QDs (dipoles) will be enhanced dramatically after the introducing of ENZ substrates. In the model of ENZ slab/dipole/air, the vanishing permittivity and refractive index of the substrate led to the

effect similar to the total reflection, and thus directed the emitting energy mostly into the medium with higher refractive index (air). In experiment, the multilayer ENZ structure was obtained using e-beam evaporation approach. The enhancement of QD emission was observed at the ENZ range as well. However, due to the limitation of the spectrum width, the emission at the non-ENZ region was not obtained and this would be finished in the further works. In general, this enhancement effect due to the presence of the ENZ substrate makes it possible to realise the directive photon amplifying and optical beam steering.

These results exhibit a fundamental and significant effect on the design of ENZ strictures and promote the further application of ENZ MMs in tunable optical devices and emission enhancement.

Chapter 4

Flexible ENZ MMs

In this chapter, I show the work of designing and experimentally realising an optical free-standing and low-loss ENZ MM. The motivation of this work is first introduced by discussing the limitation of the rigid substrate to ENZ structure and how the flexibility breaks it. Then, we demonstrate the fabrication and characterising processes of both rigid and flexible ENZ slab in detail. Finally, an application of the flexible ENZ membrane is shown, followed with a conclusion. The work of this chapter has been published in journal "APL Photonics".

4.1 Motivation

Many ENZ medium based applications, such as invisibility cloaking[121, 122], superlensing[123, 124] and optical sensing[125, 126], could benefit from mechanical flexibility[127]. Flexible MMs can be tuned after fabrication and they can conform to targets with arbitrary shapes, decoupling the fabrication constraints of the form factor of the targets[128]. In visible, infrared, terahertz and microwave regimes, flexible MMs exhibit great potential in imaging[77, 129–131], optical, chemical and biological sensing, and the realisation of practically flexible optoelectronic devices[132–136].

Here, we design and experimentally realise a low-loss, flexible and free-standing ENZ MM in the visible range. We use a metal/dielectric multilayer structure to achieve the ENZ condition. By using a sacrificial layer-assisted transfer method, we integrate the fabricated ENZ MM with a flexible substrate, and we show that it preserves its optical properties after 10000 bending cycles. Furthermore, we experimentally prove that the flexible ENZ membrane is able to conform on surfaces with a radius of curvature of the order of few microns, and this makes it possible to realise the superlens and other optical sensors.

4.2 Fabrication

The ENZ MM is a metal-dielectric multilayer, where the unit cell consists of three layers made of electron beam evaporated Ag (Ge) and a spin-coated, epoxy-based polymer (SU-8, Microchem), respectively.

In the optical frequency range, Ag exhibits lower loss than most other noble metals[92, 93], and SU-8 shows high flexibility, good thermal stability and high transparency in the full visible spectrum[137, 138]. SU-8 is commercially available in different formulations, to produce films of thickness that go from a few tens of nanometers to several tens of microns. Additionally, we have tried other dielectric materials, such as SiO_2 and hafnium dioxide (HfO_2), but these thin films exhibit wrinkles and defects after bending, which are not ideal for the realisation of flexible membrane. Hence, with its stable optical properties and high flexibility, the SU-8 layer is a good candidate for acting as the dielectric layer for realising the zero permittivity condition and also the flexible ENZ membrane. To achieve the ENZ condition at the visible range (wavelength at about 680 nm), the thicknesses of SU-8 and Ag layers are designed as 85 nm and 15 nm, respectively. The thickness of each layer is detected by a surface profiler (Veeco Dektek 150).

SU-8 could be spun on the surface of a substrate (SiO_2 or Si) with thickness varying from a few nanometers to hundreds of microns, based on different spin speeds and concentrations. There were two kinds of SU-8 used here: SU-8(3:1) with a weight concentration of SU-8(2000.5): SU-8(2050) = 3:1 and SU-8(1:2) with a weight concentration of SU-8(2000.5): cyclopentanone = 1:2. Figure 4.1 showed the thickness of SU-8(3:1) and SU-8(1:2) as a function of the spin speed. The thicknesses of SU-8 layers were measured using a surface profiler. For each concentration, there were three identical SU-8 films were fabricated and their thicknesses were all measured to obtaining the uncertainties of thickness, which were also shown in Figure 4.1.

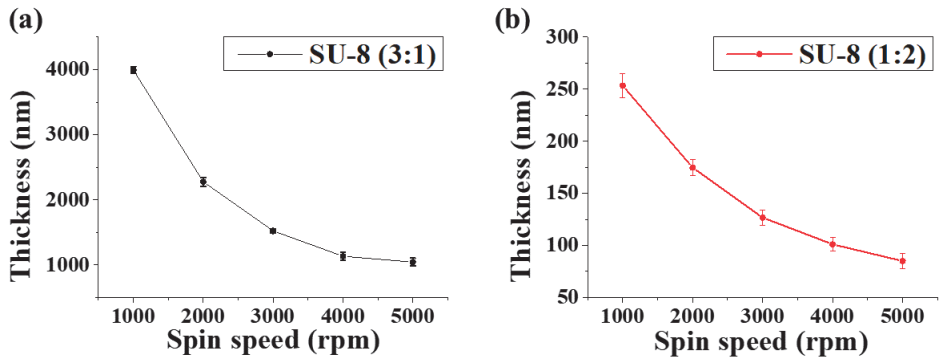

Figure 4.1: The thickness of SU-8(3:1) (a) and SU-8(1:2) (b) spun for 1 min in different speed.

The Ag layers were deposited using e-beam evaporation method, in large scale and showing controllable thickness. However, due to the poor wettability of Ag, the evaporated ultra-thin Ag films have relatively rough surface due to the cluster effect[97]. In the designed multilayer ENZ structure, 15 nm Ag layer shows obvious defects on its surface (Figure 4.2 (a)) and this caused high optical loss[98] and scattering effects[99, 100]. To improve the smoothness of Ag layer, a popular method is introducing a wetting layer, specifically a 0.7 nm Ge layer[98], as we discussed in Chapter 3, prior the definition of Ag layer. Using this technique, it is possible to obtain smooth and continuous Ag layers with a percolation limit below 5 nm[64, 97, 98]. Considering the deposition of Ag layer is happened on the surface of SU-8 layer, the other method to obtain ultra-smooth Ag layer is treating the SU-8 substrate with oxygen (O_2) plasma prior the evaporation. The O_2 plasma ashing was performed for 10 s in a plasma asher (GaLa Instrumente GmbH) with power of 100 W and O_2 gas flow of 3 sccm.

The surface morphology of Ag layers under different treating conditions are shown in Figure 4.2. Ag layers were deposited on top of 85 nm SU-8(1:2) layer. Without any treatment, the Ag layer shows obvious cracks on its surface (Figure 4.2 (a)). By comparing Figure 4.2 (a) and (b), we can find that the presence of Ge wetting layer reduce the surface roughness dramatically and qualitatively indicates that the Ge seeding layer improves the Ag layer smoothness. Similarly, by treating the SU-8 layer with O_2 plasma, we largely improved the smoothness of Ag layer but left inconspicuous clusters on the surface (Figure 4.2 (c)). Finally, by treating the SU-8 layer with both plasma ashing and Ge wetting layer, we obtained the best smoothness of the Ag layer (Figure 4.2 (d)), which was comparable to the one treated with only Ge wetting layer. Hence, both plasma ashing and Ge wetting layer benefit the deposition of ultra-smooth Ag layer, while the Ge wetting layer has a better performance. Besides, considering the potential contamination during the plasma ashing, we only used the Ge wetting layer for improving the smoothness of Ag layers in the fabrication of multilayer ENZ structures. The homogeneous Ag layer with low absorption was then obtained.

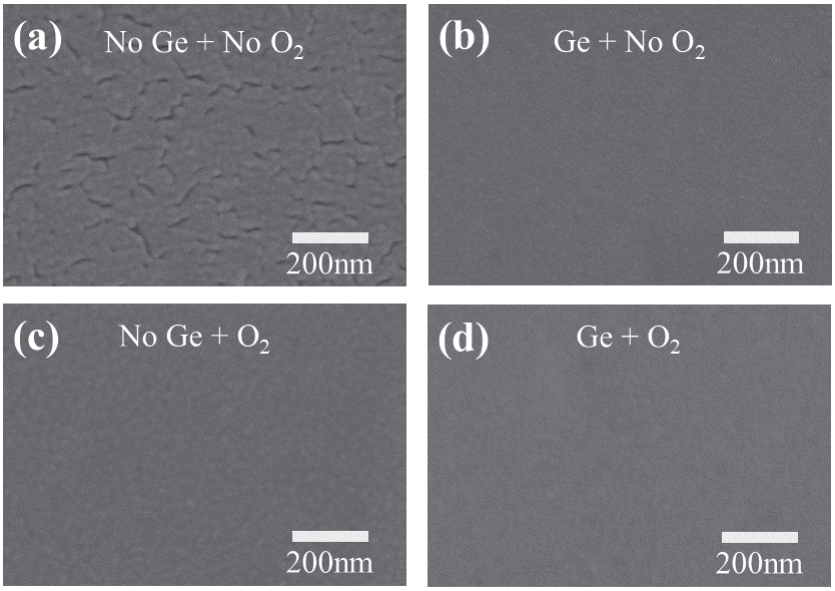

Figure 4.2: SEM images of 15 nm Ag layers deposited on identical SU-8(1:2) layers under different treating circumstances: (a) with neither Ge wetting layer nor O_2 plasma ashing; (b) with Ge wetting layer but no O_2 plasma ashing; (c) with O_2 plasma ashing but no Ge wetting layer; (d) with both Ge wetting layer and O_2 plasma ashing.

The flexibility is realised by using another polymer OmniCoat (Microchem), serving as the sacrificial layer. The OmniCoat can be spun on Si or glass substrates before the definition of the multilayer structure and then dissolved by a tetramethylammonium hydroxide (TMAH) based solution (specifically, MF 319 (Microposit)), after the definition of ENZ structures.

The fabrication process of Ag/SU-8 flexible ENZ membrane (FlexENZ) is shown in Figure 4.3. A glass or Si (rigid) substrate was first cleaned by ultrasonic bathing in acetone and IPA, each for 5 min. A sacrificial layer (Omnicoat) is deposited on the rigid substrate through spin coating and baked for 1 minute at 230°C. Next, a supporting layer of SU-8(3:1) with the thickness of 3 µm is spun coated on the sample and baked at 100°C for 5 minutes, followed by UV exposure for 3 minutes and post-exposure baking at 100°C for 2 minutes (Figure 4.3 (a)), to promote the permanent cross-linking of the polymer. This layer facilitates the mechanical handling of the final device, but it does not contribute meaningfully to its optical properties and, if required, can be completely eliminated. To obtain the ENZ condition in the visible range, we chose a unit cell with a total thickness of 100 nm, with a 15:85 metal to dielectric ratio. Then a 15 nm metallic (Ag) layer and its 0.7-nm Ge wetting layers were deposited via e-beam evaporation, followed with the definition of a SU-8(1:2) layer with thickness 85 nm, obtained via spin coating and then baked, exposed and post-exposure baked

with the same parameters used for the thick support layer (Figure 4.3 (b) and (c)). After repeating several rounds (e.g. 3, 4 and 5) of the deposition of Ag and SU-8(1:2) layers, the multilayer structure desired was obtained (Figure 4.3 (d)). Here we show results with devices made of up to 5 bilayers, which is sufficient to homogenise the response of the multilayer. After that, the OmniCoat layer was removed using MF 319 in a few hours and the multilayer ENZ membrane was then released (Figure 4.3 (e)). Finally, the multilayer metamaterial was transferred to cover irregular objects (typically micro-spheres) located on Si or glass substrates (Figure 4.3 (f)).

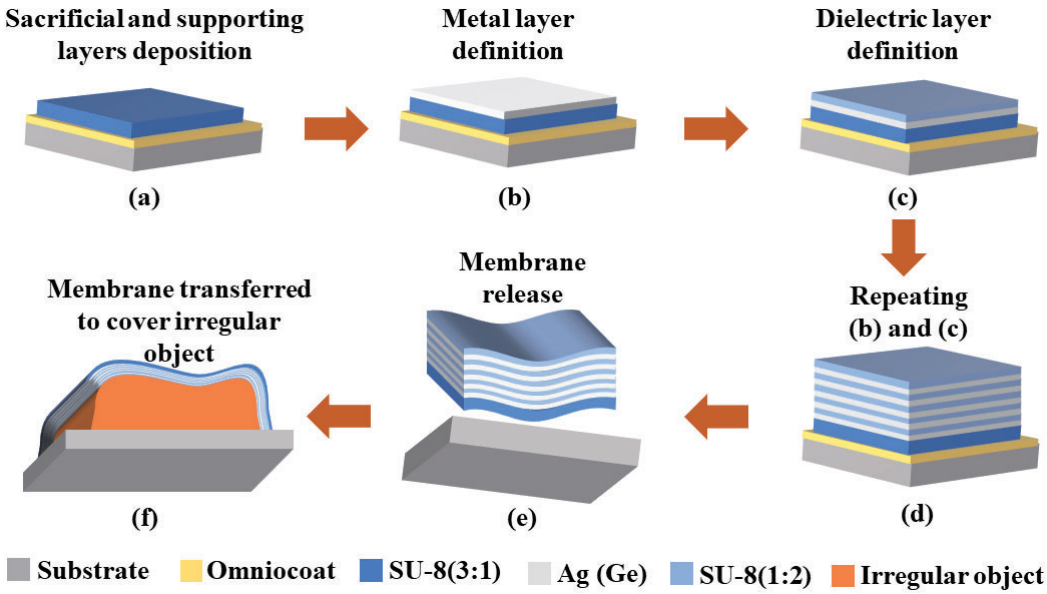

Figure 4.3: Fabrication process of FlexENZ. (a) The deposition of sacrificial layer (Omnicoat) and supporting layer (SU-8(3:1)) on stiff substrate (glass or Si). (b) and (c) The definition of first metal/dielectric (Ag/SU-8(1:2)) bilayer. (d) Repeating the deposition of bilayers. (e) and (f) Releasing the ENZ membrane and transferring it to cover irregular object.

Figure 4.4 shows the released ENZ membrane transferred onto a flexible plastic frame. The centre of the plastic sheet was cut out to exposing the ENZ membrane for further measurement and transferring to cover other objects.

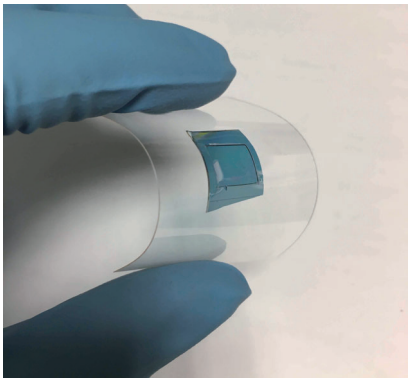

Figure 4.4: A representative photograph of a hand-held FlexENZ. The FlexENZ was transferred onto a flexible plastic sheet with a hole in the centre.

4.3 Characterisation

We characterised the optical properties of the fabricated devices using a collimated beam of 5 mm generated by a tungsten halogen light source, at normal incidence to the sample. The transmitted and reflected signals were collected and analysed with two optical spectrometers. To this extent we used the standard retrieval approach demonstrated in Chapter 3[139], which uses Fresnel's equations[80] to extract the effective complex permittivity ($\epsilon = (n + ik)^2$) of a thin film of an unknown material, which based on the measured transmission (T) and reflection (R) spectra.

In Figure 4.5 (a), we report refractive index (n) and extinction coefficient (k) of different SU-8 layers, suitably spin-coated on a glass substrate, in both the formulations used for the thick and thin layers. From the measurements, we obtained effectively constant refractive indices of 1.64 and 1.66, respectively, with negligible losses ($k \approx 0$). With its stable optical properties and high flexibility, the SU-8 layer is a good candidate for acting as the dielectric layer for realising the zero permittivity condition with high flexibility.

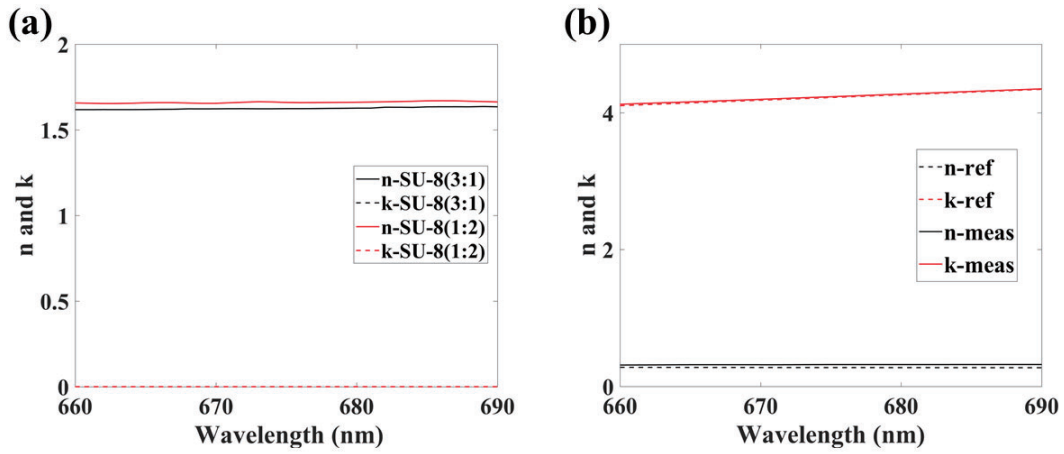

Figure 4.5: Optical characterisation results of SU-8 layers and the 15 nm Ag layer. (a) The refractive index (n) and extinction coefficient (k) of measured SU-8 layers in different concentrations. (b) The n and k of the Ag layer (with Ge wetting layer) in measurement (n-meas, k-meas) and reference (n-ref, k-ref)[66].

As discussed in the fabrication section, the Ge wetting layer did improve the smoothness of the Ag ultra-thin layer, and this is quantitatively confirmed by the retrieved optical parameters, shown in Figure 4.5 (b). The retrieved refractive index (n-meas) and extinction coefficient (k-meas) of Ag layer show that the film behaves like bulk Ag, with values reported in literature[66].

To check for consistency of the measured data, Figure 4.6 we show the measured transmission (Tm), reflection (Rm) and absorption (Am) spectra for a 5-bilayer ENZ MM, compared to the respective spectra Tc, Rc and Ac, calculated by using Fresnel's equations and the values measured n and k of SU-8(1:2) and Ag layers reported in Figure 4.5 (a) and (b).

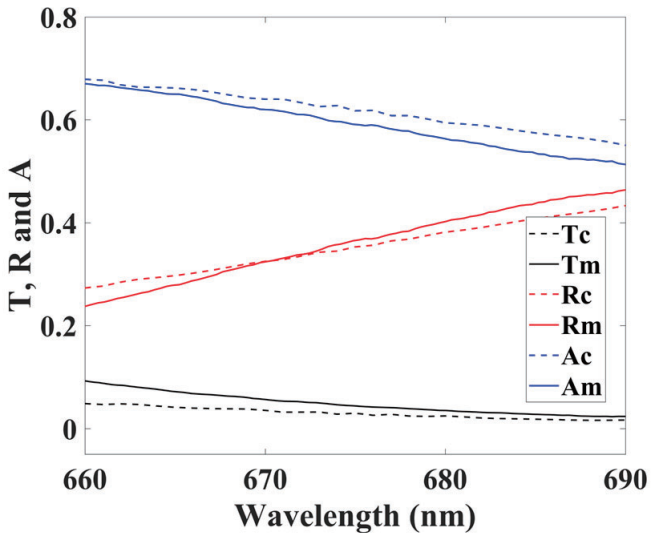

Figure 4.6: Transmission (T), reflection (R) and absorption (A) of 5-bilayer Ag/SU-8(1:2) structure in measurement (Tm, Rm, Am) and calculation (Tc, Rc, Ac) using measured n and k of SU-8(1:2) and Ag layers shown in Figure 4.5 (a) and (b).

Furthermore, it is important to verify the validity of the EMT for our samples. We fabricated 3-, 4- and 5-bilayer ENZ samples on glass substrates using the same parameters of Ag and SU-8(1:2) layers as the ones used in Figure 4.5. We measured the transmission (T) and reflection (R) spectra of these samples before their releasing from the rigid carriers, and that of the free-standing 5-bilayer sample. Figure 4.7 (a) and (b) show the measured T and R of rigid and released ENZ samples. With the number of bilayer increasing, the T and R curves all tend to converge, which indicates that the effective permittivity theory works well in the 5-bilayer situation.

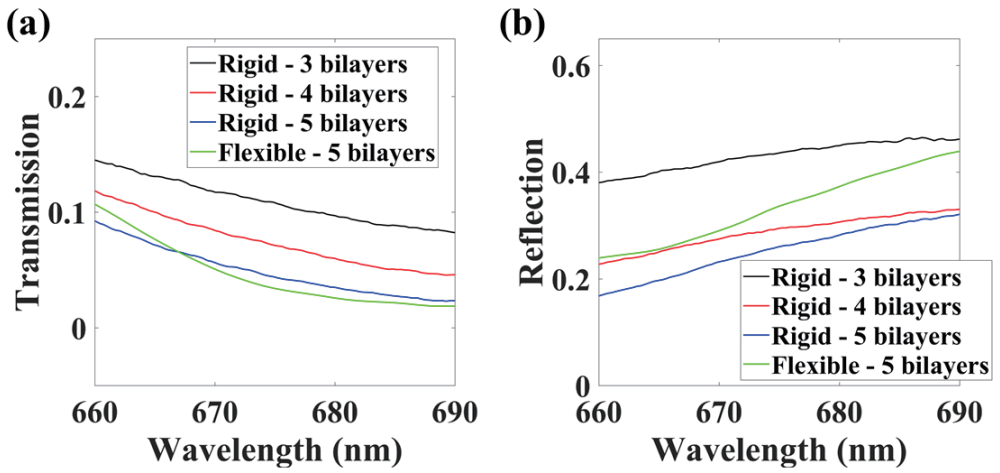

Figure 4.7: Transmission (a) and reflection (b) characterisation of rigid 3-, 4- and 5-bilayer and flexible 5-bilayer ENZ structures.

According to the measured T and R signals in Figure 4.7 (a) and (b), the permittivity (real and imaginary parts) of related ENZ samples was retrieved and shown in Figure 4.8.

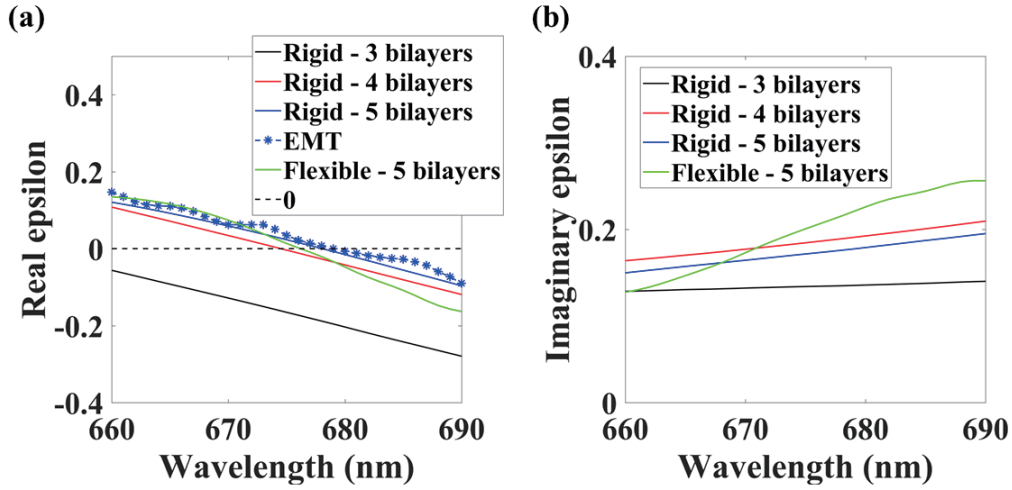

Figure 4.8: Real (a) and imaginary (b) parts of retrieved epsilon of different ENZ samples (rigid 3-, 4- and 5-bilayer and flexible 5-bilayer) based on the T and R shown in Figure 4.7.

As the layer number increases the permittivity values tend to converge toward the theoretical curve, obtained using the EMT with the retrieved values of the permittivity of the individual layers (Figure 4.8 (a)). It should be noted that the imaginary part of the retrieved permittivity for the flexible case appears to be much higher than the rigid case. We attribute this difference to the change in reflectivity (see panel (b) of the same figure), caused by a not perfectly planar surface after the

membrane release. Hence, the EMT works well for the 5-bilayer ENZ membrane which can be considered as FlexENZ after releasing for further investigation.

4.4 Results and discussion

To verify the ability of the FlexENZ to withstand deformations without compromising its optical properties, we transferred the free-standing 5-bilayer sample onto a flexible plastic frame, as shown in Figure 4.9 (a). The sheet was then fixed onto a motorized translation stage (Thorlabs) and subject to up to 10000 bending cycles (BCs) with optical measurements performed at the end of various cycles. Figure 4.9 (b) sketches the curved sheet that has arclength L=4 cm and the cord distance D varied from 1.5 to 3 cm via the moving translation stage. Correspondingly, the curvature (defined as the reciprocal of the radius) of the free-standing ENZ MM was changed from 0.5 to 0.2 cm^{-1}.

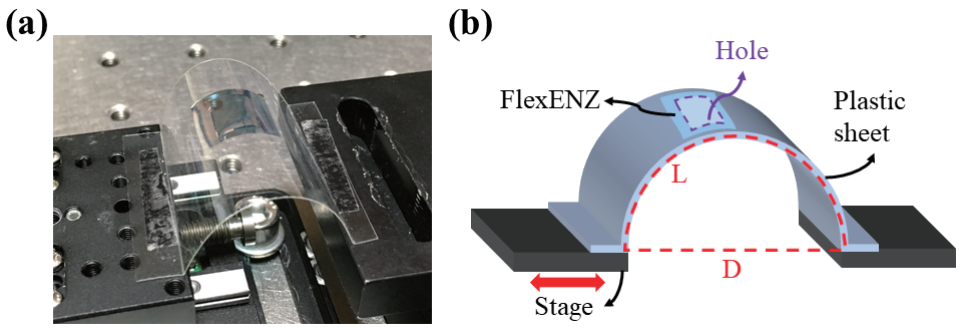

Figure 4.9: The photograph (a) and diagram (b) of a curved 5-bilayer FlexENZ fixed on a motorized translation stage.

In Figure 4.10, we report the transmission (a) and reflection (b) spectra of the FlexENZ sample after 10, 100, 1000 and 10000 BCs, using the optical characterisation setup described in Section 4.3.

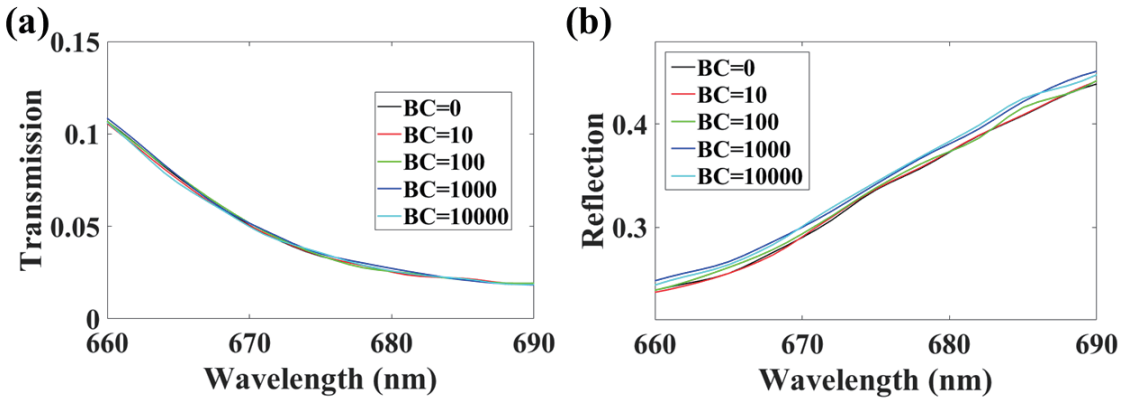

Figure 4.10: Measured transmission (a) and reflection (b) of 5-bilayer FlexENZ sample after different BCs, from 0 to 10000.

After every bending, the T curve of the FlexENZ remain the same and the R curve shows little difference within 10%. Additionally, the retrieved real permittivity, shown in Figure 4.11 (a), remains identical after bending. The imaginary epsilon (Figure 4.11 (b)) shows overall low value and does not change much due to the bending effect. These results for the different number of BCs remain essentially unchanged, proving that our flexible ENZ MM can withstand large mechanical deformations while preserving its optical properties with a very high level of reversibility and repeatability.

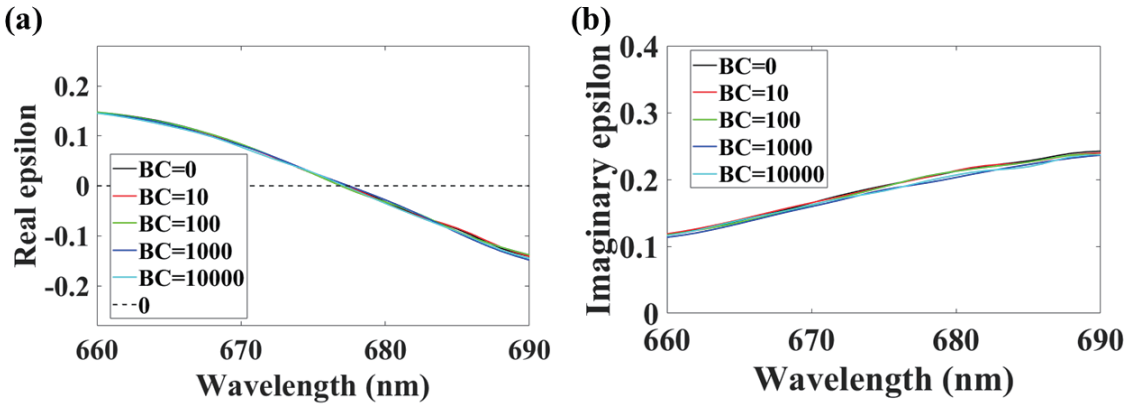

Figure 4.11: Retrieved epsilon (real and imaginary parts) of the FlexENZ sample after bending different times, based on the T and R shown in Figure 4.10.

Finally, to test the compliance of the membrane, we transferred the FlexENZ sample on a Si substrate containing sulfate latex microspheres with a diameter of 6 µm (curvature of 6000 cm^{-1}). The high curvature is recognisable in top-view SEM images, of the coated spheres, as shown in

Figure 4.12 (a). To better investigate the coverage of the microspheres, we cut through the ENZ MM coated sphere using focused ion beam (FIB) milling. In order to protect the top SU-8 layer, we deposited a protective platinum (Pt) thin layer before the FIB process via ion beam-induced deposition (IBID)[140]. Figure 4.12 (b) and (c) show the cross-section SEM images of the interface between the sphere and FlexENZ. As visible in Figure 4.12 (b), the cut sphere appeared deformed. At this stage, we were not able to ascertain with absolute certainty whether this was due to the weight of the membrane or the FIB processing. In any case, this effect would have to be considered where the application requires coating delicate or deformable samples.

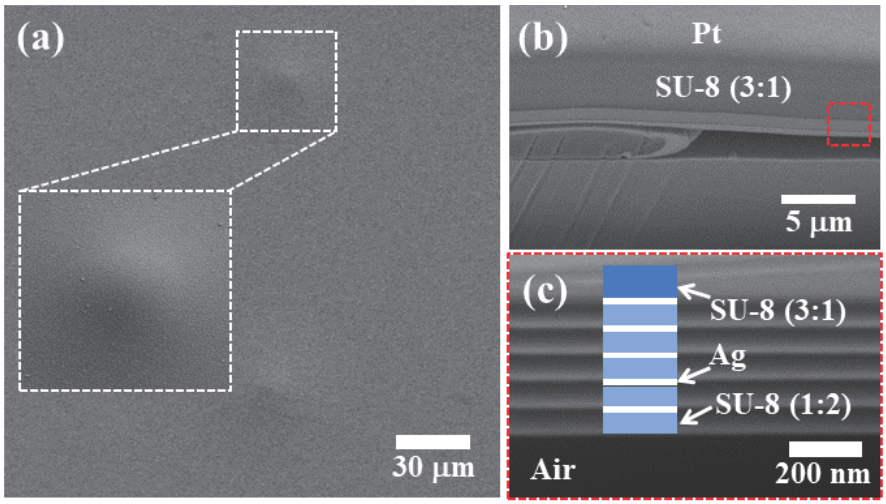

Figure 4.12: SEM images of the FlexENZ sample covering sulfate latex spheres. (a) and (b) Top viewing and cross-section SEM images of FlexENZ covering spheres. (c) SEM image to show the Ag/SU-8(1:2) multilayer ENZ structure marked in (b) with a red dash frame.

Another method to test the tightness of the FlexENZ covering sphere is using the optical microscope. The curvature caused by the contact between spheres and ENZ membrane clearly exhibited Newton-Rings patterns (Figure 4.13). The gap between adjacent rings is related to the probing wavelength and the order of the rings. If needed, the curvature can be obtained by probing the sample with single-wavelength laser, but the illuminating source of the microscope is a white source (broadband), we cannot directly calculate the curvature of the Newton-Rings patterns. Even so, the uniform rings distribution indicated qualitatively that the curvature at the sphere/membrane interface was homogeneous.

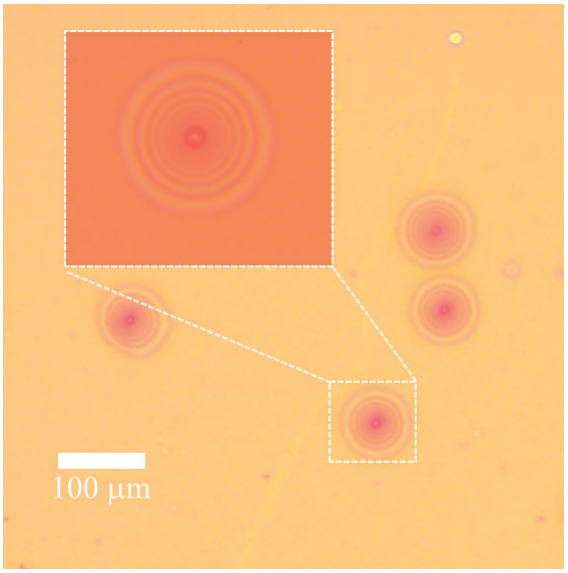

Figure 4.13: Microscope images of curved FlexENZ over the spheres beneath and showing Newton-Rings pattern.

We believe that this high-curvature covering method will help ENZ structures to overcome the diffraction limitation and realise high-resolution imaging on a micro or even a nanoscale.

4.5 Conclusion

In this work, we designed and fabricated a flexible free-standing ENZ MM consisting of Ag/SU-8 multilayers. The SU-8 layer was fabricated using the spin coating method and showed high flexibility and negligible optical loss. The Ag layer was deposited in an e-beam evaporator and obtained high smoothness and low optical loss with the help of Ge wetting layer. The ENZ condition was achieved at about 680 nm by repeating the definition of the SU-8 and Ag layers 5 times which conformed to the EMT.

The flexible ENZ MM was created particularly by introducing an Omnicoat sacrificial layer between the ENZ structure and the rigid substrate. We showed that the optical properties of the FlexENZ do not significantly change after repeated, macroscopic and sustained mechanical deformations (up to 10000 cycles). The free-standing ENZ MM can also fit surfaces with a radius of curvature of the order of few microns. We believe that our results could enable novel tunable nano-optical components for achieving ENZ-based applications such as field enhancement, wavefront shaping, all-optical modulation and optical sensing.

Chapter 5

Graphene-based ENZ MMs

In this chapter, I propose a method to design and fabricate graphene-based ENZ MMs that formed by graphene and dielectric nanolayers and can be used for flexible and tunable ENZ membrane applications. I have not finished the demonstration of the ENZ response of graphene/dielectric multilayer structure here, but managed the fabrication protocol and obtained some initial results.

The structure of this chapter is as follows. First, I briefly explain the motivation of this project and introduce the design mechanics and numerical results of the graphene/dielectric multilayer ENZ model. Then, the fabrication of both graphene and multilayer structures are demonstrated. The characterisation of graphene layers using various approaches is also presented. Finally, I present the optical behaviour of the graphene-based ENZ structures in both visible and infrared regime, and also the preliminary results of electrically tuning of the structures.

5.1 Motivation

The multilayer structure constructed by metal and dielectric components in the sub-wavelength range is a popular approach to realised the ENZ MMs. However, this structure shows high absorption due to the high optical loss of the metal unit layer[25, 92]. This limits its feasibility of applications in the optical range. Additionally, metal layers show poor tunability about their optical properties[26], and this effect reduces the possibility of tuning the ENZ structure. Here, we propose another multilayer structure to achieve the ENZ condition by replacing the metal layer with graphene layer, as graphene exhibits negative and tunable permittivity at visible and infrared frequencies, with low optical loss[141].

Graphene[142, 143], known as a real 2D semi-metal material, attracts wide attention because of its tunable optical properties, physical flexibility and high electron mobility[144–146]. The permittivity

of graphene is determined by its conductivity which can be tuned via applying an external electric field, chemical or molecular doping and thermal stimulation[147–149]. Therefore, graphene has great potential for realising tunable multilayer ENZ structure. Besides, benefiting from the single-layer atomic structure, graphene also exhibits extremely high flexibility and plasticity with a considerable toughness, which makes it a great candidate as the component of flexible MMs. Graphene has been applied into variable fields, for example optical modulation[145], polarisation dependent absorption[141, 150] and surface cloaking[151].

Here we investigate a graphene/dielectric multilayer structure to realise ENZ condition which can be tuned by applying voltage in visible and infrared regime. The CVD approach is demonstrated in this chapter to produce high-quality, high-performance and monocrystal graphene. Under the condition of high temperature and low pressure, carbon sources (e.g. methane (CH_4)) will pyrolyse and be reduced by specific gas (e.g. hydrogen (H_2)) to produce free carbon atoms which form the graphene film on the surface of transiction metals (e.g. copper (Cu) and nickel (Ni))[152]. The graphene samples are characterised via Raman spectroscopy[153, 154], custom made atomic force microscope (AFM) and other optical and electrical methods. The multilayer graphene/dielectric structures are achieved by stacking or rolling unit layers. However, we have not experimentally realised a fully workable ENZ structure here. We believe that the tunable graphene-based ENZ MMs offer a new platform for optical switching, photonic memory and other optoelectronic applications.

5.2 Numerical modelling of graphene/PMMA multilayer structure

The graphene/dielectric multilayer structure is designed based on the EMT and sketched in Figure 5.1. As the probing light propagates along the stacking direction in our measurement, we only consider the effective permittivity ($\epsilon_\perp$) of the multilayer structure perpendicular to the stacking direction here. In the sub-wavelength range, the $\epsilon_\perp$ is described as

$$\epsilon_\perp = (t_g\epsilon_g + t_d\epsilon_d)/(t_g + t_d) \tag{5.1}$$

where t_u, ϵ_u ($u = g, d$) are the thickness and permittivity of unit layers, and the subscripts g, d represent the graphene and dielectric layers, respectively.

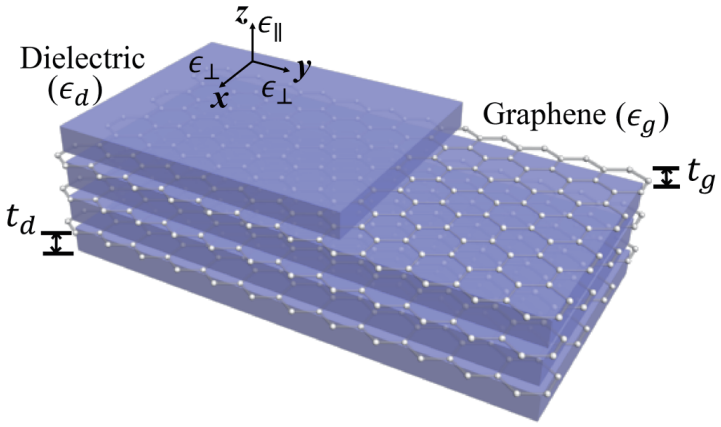

Figure 5.1: Diagram of graphene/dielectric multilayer structure to achieving ENZ condition.

In the visible regime, we choose polymethyl methacrylate (PMMA) as the dielectric unit layer because of its high transparency and flexibility. This is also prepared for realising the flexible ENZ structure. The permittivity of PMMA (ϵ_d) is described as[155]

$$\epsilon_d = 1 + \frac{0.99654\lambda^2}{\lambda^2 - 0.00787} + \frac{0.18964\lambda^2}{\lambda^2 - 0.02191} + \frac{0.00411\lambda^2}{\lambda^2 - 3.85727} \tag{5.2}$$

where λ is the wavelength of probing light with the unit of μm.

Graphene has an effective permittivity which relates to its conductivity (σ_g) and thickness, and described as[149, 156]

$$\epsilon_g = 1 - i\frac{\sigma_g}{\omega\epsilon_0 t_g} \tag{5.3}$$

where ϵ_0 is the permittivity of vacuum, ω is the angular frequency of the incident wave.

At the visible and infrared range, the conductivity of graphene is determined by Kubo formula[149, 157], shown as

$$\sigma_g = -\frac{i4\pi q^2 k_B T}{h^2(\omega - i2\tau)}[\frac{\mu_c}{k_B T} + 2ln(e^{-\mu_c/k_B T} + 1)] - \frac{i4\pi q^2(\omega - i2\tau)}{h^2}\int_0^\infty \frac{f_D(-\xi) - f_D(\xi)}{(\omega - i2\tau)^2 - 16(\pi\xi/h)}d\xi \tag{5.4}$$

where q means the electron charge, k_B is Boltzmann constant, T represents absolute temperature, h is Planck constant, ω stands for the angular frequency of incident wave, τ is the phenomenological scattering rate (0.1 meV), μ_c represents the chemical potential and $f_D(\xi)$ is the Fermi-Dirac function ($f_D(\xi) = 1/[e^{(\xi-\mu_c/k_B T)} + 1]$).

The μ_c can be controlled by doping, changing temperature and applying voltage[158]. The easiest and most reliable way to tune the μ_c is applying gate voltage V_g, given by the relationship of[159]

$$|\mu_c| = \hbar v_F \sqrt{\pi |a_0(V_g - V_{dirac})|} \tag{5.5}$$

where $\hbar$ is reduced Planck constant, $v_F = 9 \times 10^5$ m/s is the Fermi velocity of Dirac fermions in graphene, $a_0 \approx 9 \times 10^{16}$ $m^{-2}V^{-1}$ is the constant estimated from the parallel-plate capacitor[160], and V_{dirac} is the voltage offset resulted from the defect or doping in graphene and typically its value is small and we set it as 0 here.

To demonstrate the voltage tuning effective permittivity of the graphene/dielectric multilayer structure, we consider a specific model formed by graphene and PMMA unit layers. The thickness of a single graphene layer is 0.335 nm[161] and we set the thickness of PMMA (t_d) as 10 nm and 40 nm, respectively. At visible range, the effective permittivity ($\epsilon_\perp$) of the graphene/PMMA multilayer structure changes along with the applying voltage and the wavelength of incident wave, shown in Figure 5.2.

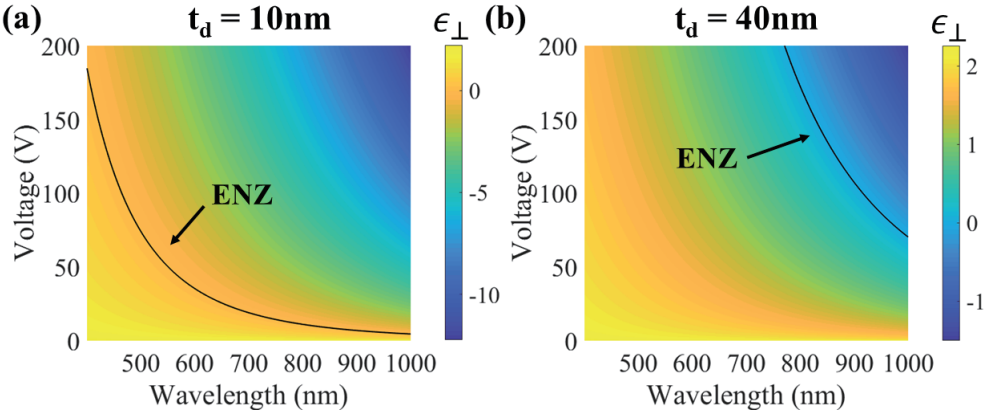

Figure 5.2: The calculated effective permittivity ($\epsilon_\perp$) of the graphene/PMMA multilayer structure formed by unit layers of single-layer graphene and PMMA layer with different thickness (t_d) of 10 nm (a) and 40 nm (b). The zero permittivity (ENZ) regions are marked with solid black lines.

When t_d =10 nm, Figure 5.2 (a) shows that the effective permittivity of the multilayer structure can be tuned from positive to negative at the entire visible range by applying voltage from 0 V to 200 V. With the thickness of PMMA increasing to 40 nm, the ENZ region only locates at high-voltage range (100 - 200 V) and at long-wavelength range (700 - 1000 nm). Considering the fabrication process, the 10 nm PMMA is difficult to obtain via spin-coating method, hence the model with t_d =40 nm is more practical. In Figure 5.3, we present the calculated real and imaginary parts of the effective

permittivity (epsilon, $\epsilon_{\perp}$) of the graphene/PMMA multilayer structure, at the condition of t_d =40 nm and V_g varying at 100, 150 and 200 V. The real part of epsilon reaches 0 at different wavelengths along with the changing of applied voltage (V_g) and the whole structure shows extremely low loss according the value of imaginary epsilon. This calculated results promise the possibility to realise the electrically tunable graphene/PMMA ENZ structure.

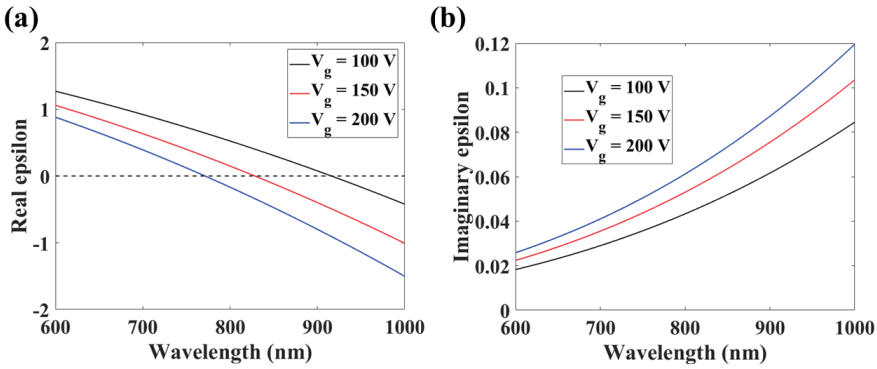

Figure 5.3: The calculated effective real (a) and imaginary (b) permittivity of the graphene/PMMA multilayer structure, at the condition of t_d =40 nm and V_g =100, 150, 200 V.

5.3 Fabrication and transfer of graphene

5.3.1 CVD process of graphene

The problem of large-area fabrication has been a major obstacle to the industrial development of graphene. At present, there are three main methods for the preparation of graphene. (i) The mechanical exfoliation method[162]: graphene prepared by this method have the same interlayer arrangement style as natural graphite crystal structure with minimal defects and highest quality, but the sample size is very small (e.g. at the range of several microns) and the production efficiency is low. (ii) The CVD method[152]: this method can be used for preparing large-area graphene. Although the defect and uniformity are relatively high, this kind of graphene can meet the basic requirements of scientific research and application by showing excellent optical properties. (iii) The chemical reduction of graphite oxide method[163]: this method can only be used to produce thick graphene with a large number of layers. The quality of this kind graphene is relatively poor, and the crystal orientation is uncertain, which is difficult to apply in the field of electronics.

Here, we use the CVD method to prepare graphene. The CVD method is based on the pyrolysis of carbon compounds (e.g. CH_4) and the growth on the substrate. This method originated from the

deposition of "single-layer graphite" pattern forming on the surface of a Pt substrate in low energy electron diffraction experiment[164]. These graphite patterns were then called "surface carbon", and they were dispersed on the surface of the platinum film[165]. Based on this discovery, there are many works focused on different metal substrates and different annealing conditions and engaged in the formation of a single-layer or a few-layers of graphite. The viable metal substrate includes Ni, iron (Fe), Pt, palladium (Pd) and Cu[166–168]. The CVD method for fabricating graphene can be divided into two kinds, based on different mechanisms[168–170]. (i) The carbon carburising mechanism: this method applies to the synthesis process on Ni and other metal substrates with high carbon solubility. Carbon atoms deriving from carbon source pyrolysis in high temperature infiltrate into the metal substrate and then separate out when the cooling process begins and form the graphene layer. (ii) The surface growth mechanism: this method is used in Cu and other metal substrates with low carbon solubility. At high temperature, carbon atoms are adsorbed by the metal substrate and distribute on the surface to form the "graphene island". In the following cooling process, continuous graphene is formed from the "graphene islands" in two-dimensional growth.

Multilayer graphene is easily grown on the Ni substrate, but the quality is not as good as the graphene on the Cu substrate. On the contrary, it is relatively easy to grow a single-layer and multilayer graphene with better quality on the Cu substrate. Besides, compared to the mechanical exfoliation method for the growth of graphene, the most significant advantage of the CVD method is large-area and controllable preparation, and the CVD graphene can be easily transferred to other substrates for desired applications. High-quality CVD graphene can easily achieve the continuous monolayer level, with the size up to millimetre level and also good crystal quality[171, 172].

In order to deposit single-layer graphene, we use the Cu foil (Alfa Aesar) as the substrate with the custom developed CVD apparatus sketched in Figure 5.4. The deposition occurs in a quartz tube, which surrounded by a high-temperature furnace. The furnace is fixed onto a translation stage, to allow the fast cooling of the sample to room temperature. The tube is connected to a high-vacuum pumping system including a vacuum pump and a pressure detector. During the CVD process, three gases, argon (Ar), H_2 and CH_4, are injected into the tube. We use pressure regulators to control the flow rate and ratio of gases. The Ar is the protection gas of the system due to its inactive and stable chemical properties, especially at high temperature[173]. The H_2 gas reacts with the CH_4 gas to create graphene molecules and also able to remove and prevent the oxidation of the Cu substrate.

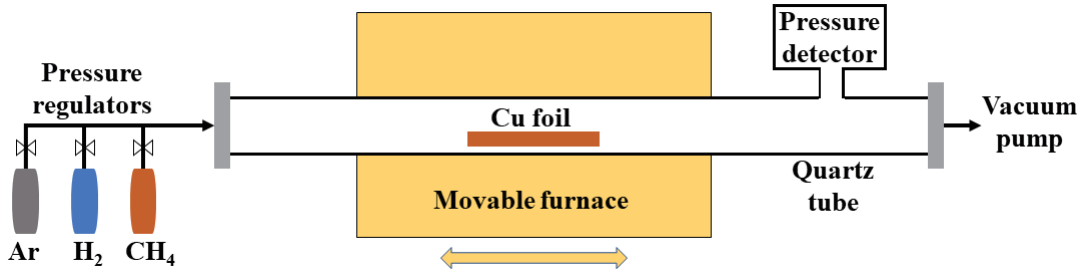

Figure 5.4: Diagram of the CVD apparatus, which contains a quartz tube hosting the Cu foil, a movable high-temperature furnace, a vacuum pumping system, and the gas injection system.

Figure 5.5 illustrated the fabrication procedure of the CVD method. First, the Cu foil, typically with size of 2 cm by 4 cm and thickness of 25 µm, was cleaned and deoxidised in a 20% acetic acid aqueous solution, before loaded into the quartz tube, followed by the gas washing of the tube via vacuum pumping and Ar injection alternatively for 3 times, to creating an oxygen-free atmosphere. Then, the tube was evacuated into 300 mTorr and heated to 1000 °C. Next, the substrate was annealed at the temperature for 30 minutes with a 500 sccm gas flow of Ar and 10% H_2. During the annealing process, H_2 removed the oxide on the surface of Cu, and this effect also increased the Cu grain size which will benefit the growth of large and uniform graphene. After that, the deposition step started at the same temperature and the pressure of 100 mTorr. The CH_4 gas injected for different time (1 - 10 minutes) to create graphene films with a different number of layers. Under the protection of Ar and catalysation of H_2, CH_4 atoms decomposed at high temperature on the surface of Cu film to form a carbon–metal solid solution. The graphene was synthesised at the final step when the system was cooled down to room temperature at variable cooling speed. The carbon atoms diffused from the solid solution and form the single- or few-layer graphene on the surface of Cu. The number of the graphene layer is related to the time of reaction with CH_4, the gas ratio between H_2 and CH_4, and also the cooling rate. The relationship between the number of graphene layers and fabrication parameters are discussed in detail in the characterisation section.

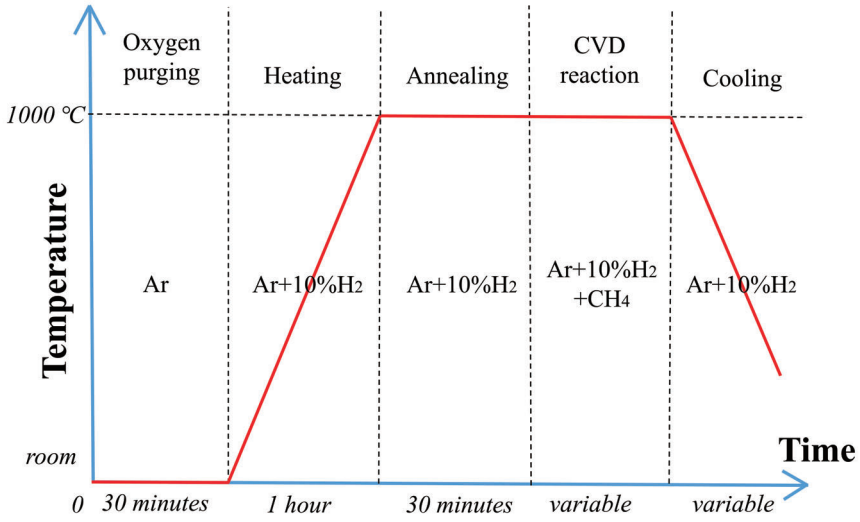

Figure 5.5: Sketch of the fabrication process of the CVD process, including oxygen purging, heating, annealing, growing and cooling steps, and also the specific temperature, gas atmosphere and time consumed at each step.

In Figure 5.6, we present the Cu foils before and after the graphene deposition. The introducing of graphene changes the colour of Cu foil via adding more grey colour. This is also a visual judgement of the quality of the CVD graphene, as the high-temperature treating will not change the colour of the acid cleaned Cu foil and only the graphene deposition introduces the whitish colour.

Figure 5.6: Photographs of the Cu foil with and without graphene on the surface.

5.3.2 Graphene transfer

The CVD graphene on the Cu substrate cannot be characterised or used directly, as the bonding between graphene and Cu substrate is strong and the substrate will influence the characterisation process, e.g. Raman spectroscopy[169]. Therefore, we need to transfer the graphene sheet to other substrates, e.g. Si, glass, PMMA, ZnSe and Ge. Various approached have been developed to transfer graphene according to different transfer media, such as thermal release tape (TRT)[174, 175], PMMA[176, 177] and polyethylene terephthalate (PET)[178]. At present, the transfer methods

based on TRT and PMMA are most popular because they can support the graphene film without folding while the Cu substrates are dissolved. However, both of them have disadvantages. The TRT film introduces chemically adhesive contaminations, and this adhesive dramatically influences the performance of graphene in optical and electric regimes[179]. As for the PMMA film, although it will not bring in complicated contaminations since it can be dissolved by solvent easily, it is also easily cracked and torn during the transfer of large-scale graphene (more than 1 cm)[177, 179], due to its terrible strength. Another efficient and low-contamination method to transfer graphene uses PET film. Graphene films attach on the PET film via a pre-coated adhesive layer (silicone) based on physisorption mechanics[180] and this prevents the chemical contamination. Typically, PET films, such as screen protectors for cellphone or iPad, are commercially available and can be easily obtained. Therefore, the PET transfer method is the main approach we used in this work because of its high efficiency. The PMMA transfer method was also used here for some parts of graphene characterisation and other applications.

The PMMA transfer process is first introduced here and shown in Figure 5.7. The graphene/Cu sheet were first flatted by two glass slides (Figure 5.7 (a)) which were cleaned via acetone and IPA ultrasonic bath for 5 minutes each. Then, a PMMA layer (MicroChem, 495 A2) was spun coated on the graphene side of the graphene/Cu sample (Figure 5.7 (b)), at 1000 rpm for 1 minute. To prevent the shrink caused by high temperature baking, the PMMA layer was naturally dried at room temperature for 8 hours, followed by O_2 plasma treating for the other side (Cu) of the sample at the power of 100 W and gas flow of 3 sccm for 1 minutes (Figure 5.7 (c)). This step removed the residual PMMA at the Cu side, to ensure the Cu exposed for reacting with the dissolving solution. The next step is floating the Cu/graphene/PMMA sample on the iron chloride ($FeCl_3$) aqueous solution (1 M) to etch the Cu substrate for about 3 hours (Figure 5.7 (d)). After dissolving the Cu completely, the graphene/PMMA sample was rinsed in deionised (DI) water 3 times to remove residual $FeCl_3$ etchant and transferred onto the desired substrate and dried with nitrogen (N_2). Finally, the graphene was transferred onto the final substrate and the PMMA layer was dissolved in acetone for about 1 hour.

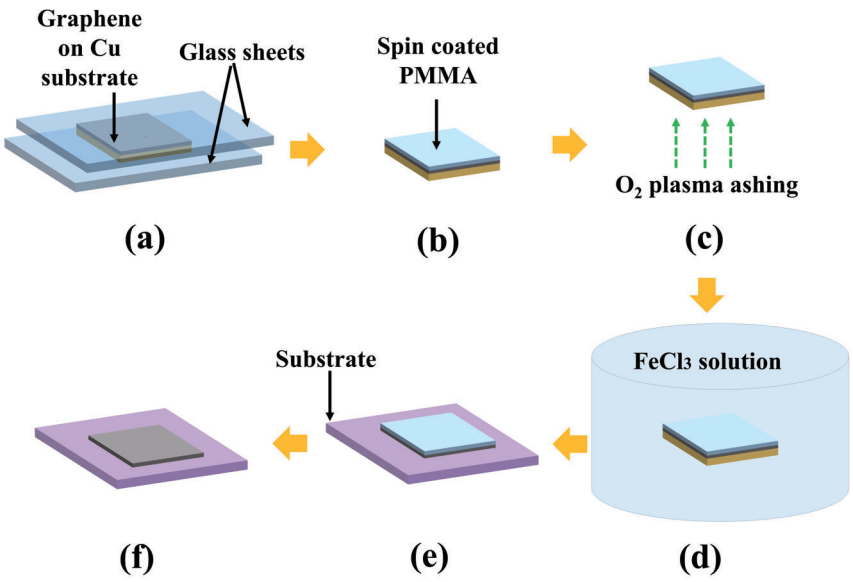

Figure 5.7: Sketch of the graphene transfer procedures using PMMA film. (a) Flattering the graphene/Cu sample. (b) Spin coating the PMMA layer onto the graphene side. (c) Plasma treating in the O_2 atmosphere to remove the residual PMMA at the Cu side. (d) Removing Cu substrate in $FeCl_3$ aqueous solution. (e) Transferring the graphene/PMMA sample onto desired substrate. (f) Removing the PMMA layer in using acetone.

As we discussed and demonstrated, the PMMA transfer method is not suitable for large-area graphene because the thin PMMA layer is easily folded and cracked during the etching process of Cu substrate (Figure 5.8). Additionally, the PMMA transfer approach takes long time, i.e. about 2 days.

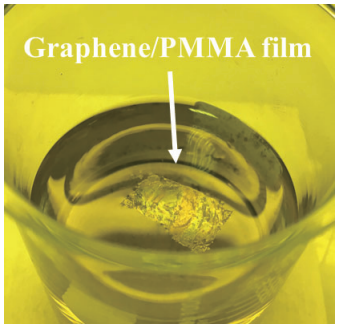

Figure 5.8: Photograph of the graphene/PMMA membrane floating on the $FeCl_3$ aqueous solution, related to the step (d) in Figure 5.7.

Therefore, we prefer another method relied on the PET film, and the process is illustrated in Figure 5.9. The transfer process is similar to the PMMA method, but the total time is much less

because we do not need to treat and dissolve the PET film like the processes of PMMA.

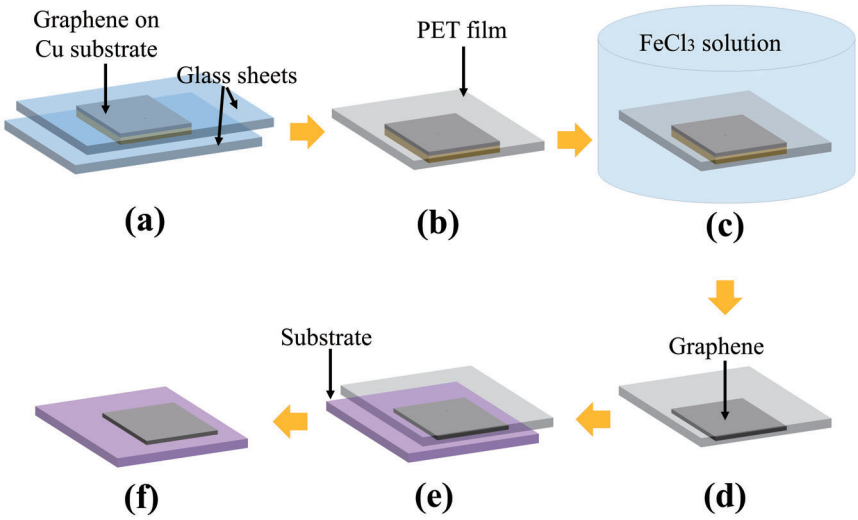

Figure 5.9: Sketch of the graphene transfer procedures using PET film. (a) Flattering the graphene/Cu sample. (b) Attaching the PET film onto the graphene/Cu sample at the graphene side. (c) Removing Cu substrate in $FeCl_3$ aqueous solution. (d) and (e) Washing and transferring the graphene/PET sheet onto desired substrate. (f) Pealing off the PET layer.

The procedures of PET transfer is described here. First, we also flatted the grapnhene/Cu sheet via compressing the sample with two cleaned glass slides (Figure 5.9 (a)). Next, a PET film was attached to the graphene side of the sample via directly contacting (Figure 5.9 (b)), followed by the Cu etching in the $FeCl_3$ aqueous solution (Figure 5.9 (c)). The graphene/PET film was then cleaned with DI water and transferred onto the desired substrate (Figure 5.9 (d) and (e)). After waiting for 3 minutes, the PET film was pealed off to leave the graphene on target substrate.

Figure 5.10 (a) and (b) present the image of graphene transferred onto Si and glass substrates, respectively. We initially tested the quality of transferred graphene via microscope observation and the microscope image in Figure 5.10 (c) indicates a high uniformity of the graphene sample.

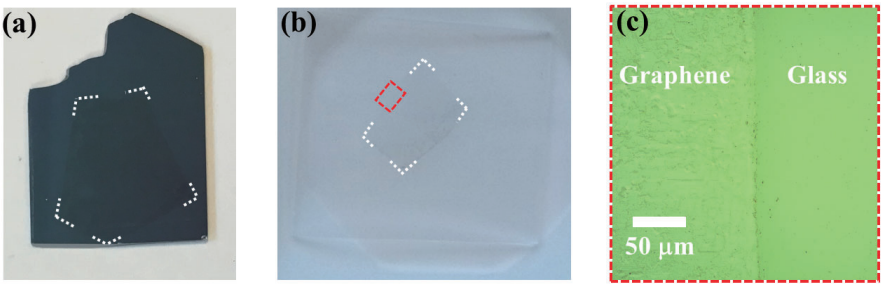

Figure 5.10: Images of transferred graphene sample. (a) and (b) Photographs of graphene samples on Si and glass substrates, respectively. The graphene regions are marked with white dashed lines. (c) The microscope image of the marked region with red dashed frame of the graphene/glass sample shown in (b).

5.4 Characterisation of graphene

Graphene can be considered as single-layer graphite, but its thickness is not only the size of the carbon atoms, i.e. about 0.142 nm[181], due to the roughness and wrinkle. The thickness of monolayer graphene is commonly considered as 0.335 nm, which is the interplanar spacing for graphene sheets stacking to form graphite. This value has been verified by measurement using various methods, such as AFM[182] and surface plasmon resonance (SPR)[183]. Because of the minimal thickness of monolayer graphene, the conventional observation method (e.g. optical microscope, SEM) cannot determine the existence and the number of graphene layers. There are several methods of determining the number of graphene layers, such as Raman spectroscopy method[154, 184, 185], AFM method[32, 186] and optical absorption determination methods[187]. In this section, we characterise graphene films with different layers using these three methods. Additionally, the conductivity measurement of graphene films are also presented here and to help us determine the quality of graphene.

5.4.1 Raman spectroscopy method

Raman spectroscopy is an accurate method for the determination of the number of graphene layers[153, 154]. This method is based on Raman scattering effect[188]. When incident light interacts with a material, most photons undergo elastic Rayleigh scattering, while about only one in a million of them undergo inelastic Raman scattering[189]. The photons which scatter inelastically exhibit energy transfer and thus the Raman scattering light has a frequency shift compared to the incident light. For incident light with different frequencies, by analysing the size and strength of frequency shift (Raman shift) of the scattering light, we can determine the molecular vibration, rotation, and interaction with

phonon of the sample, which means the molecular type of the sample is identified[190]. Raman spectra of graphene well reflect the characteristics of the electronic structure and number of layers of different graphene samples.

A Raman Microscope system (NT-MDT NTEGRA Spectra) was used to characterising graphene samples. The graphene sample was probed by a focused laser with wavelength of 473 nm and diameter of 200 µm. The exposure (integration) time of the laser was set as 1 minute for all samples. The scattered signals were collected, and spectrally analysed, and converted into the Raman spectra. Figure 5.11 present the typical Raman spectra of graphene with different layers. There are three characteristic peaks shown in the Raman spectra of graphene, i.e. D, G and 2D peaks[191]. Peak D locates at about 1360 cm^{-1} and stands for the crystal-defect degree of graphene, and its higher intensity means the higher crystal-defect degree[177]. Peak G presents at about 1580 cm^{-1} and represents the plane vibration of carbon[154]. There will be a frequency shift of peak G to higher frequencies along with the increasing of the number of graphene layers. In addition, the intensity of peak G (I(G)) will increase when the number of graphene layers increases. Peak 2D appears at approximately 2700 cm^{-1} and represents the interactions between the graphene layers. Peak 2D exhibits complicated shaping changing for graphene with different layers. Generally, it becomes broader and higher along with the increasing of the number of graphene layers as the peak is formed by many neighbouring single peaks[154, 192]. The intensity of peak 2D(I(2D)) and the width of it are inversely proportional to the number of graphene layers. This means that the peak 2D will become sharper along with the decreasing number of graphene layers. Hence, the monolayer graphene with good quality should have no peak D and with high intensity of peak 2D and low intensity of peak G. The intensity ratio between peaks 2D and G also indicate the number of graphene layers, i.e. the number of graphene layers is proportional to the ratio of I(2D) to I(G)[154, 192].

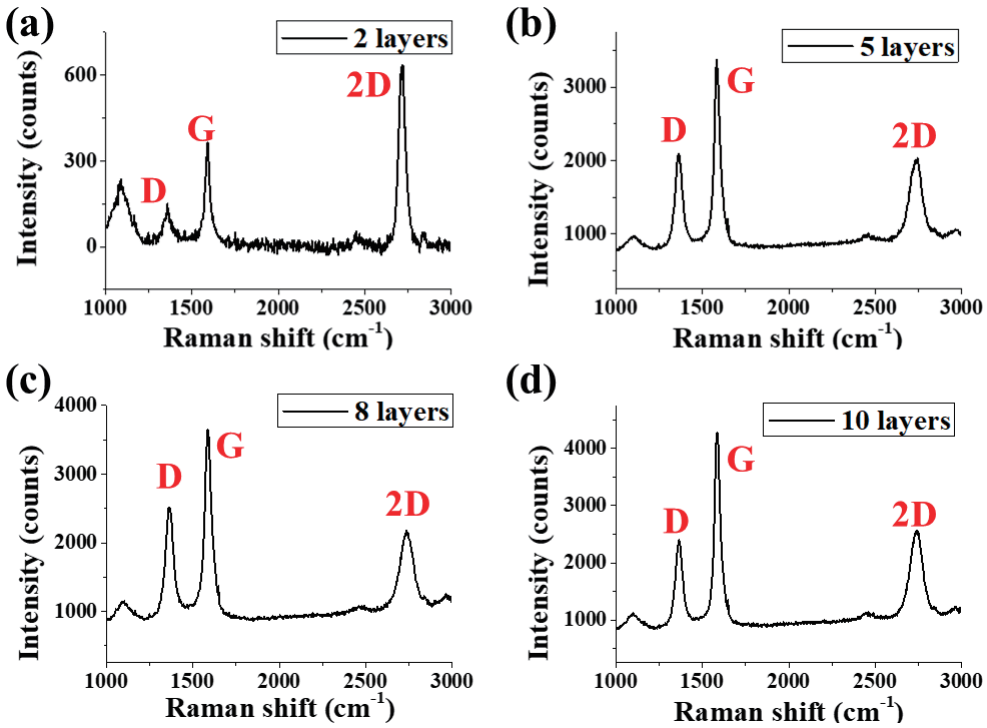

Figure 5.11: Raman spectra of slow-cooling graphene samples with different number of layers: 2 (a), 5 (b), 8 (c) and 10 (d).

The graphene samples with Raman spectra shown in Figure 5.11 were fabricated using CVD process at a condition of slow cooling with a time of more than 8 hours. Using the slow-cooling method, we easily obtained the multilayer graphene by controlling the CH_4 injection (reaction) time. The key parameters of the reaction part of these CVD processes were presented in Table 5.1.

	Reaction parameters			
Sample	Gas	Reaction time	Pressure	Cooling time
Figure 5.11 (a)	CH_4 30 sccm; Ar + 10% H_2 200 sccm	2 minutes	100 mTorr	8 hours
Figure 5.11 (b)	CH_4 30 sccm; Ar + 10% H_2 200 sccm	3 minutes	100 mTorr	8 hours
Figure 5.11 (c)	CH_4 30 sccm; Ar + 10% H_2 200 sccm	5 minutes	100 mTorr	8 hours
Figure 5.11 (d)	CH_4 30 sccm; Ar + 10% H_2 200 sccm	10 minutes	100 mTorr	8 hours

Table 5.1: The reaction parameters used in the slow-cooling CVD process to fabricating the graphene samples with Raman spectra shown in Figure 5.11.

In this case, the CH_4 molecules were first decomposed at 1000 °C and formed the carbon–metal solid solution together with the Cu substrate. When the temperature started dropping down, the graphene layers were synthesised from the carbon–metal solid solution all the time before the

temperature reached 500 °C, even the CH_4 injection was stopped at the start point of cooling[193]. By controlling the reaction time at 3, 5, and 10 minutes, we controlled the injected CH_4 gas amount and thus obtained 5-, 8- and 10-layer graphene, receptively. The number of graphene layers were estimated from the Raman spectra[154, 192] shown in 5.11 (b) - (d). By reducing the reaction time down to 2 minutes, we still obtain the 2-layer graphene film, indicated from the Raman spectrum (I(2D) : I(G) $\approx$ 2) shown in Figure 5.11 (a). The relationship between the number of graphene layers and the ratio of I(2D) : I(G) was presented in Table 5.2

Sample	I(2D) : I(G)	N
Figure 5.11 (a)	1.8	2
Figure 5.11 (b)	0.8	5
Figure 5.11 (c)	0.6	8
Figure 5.11 (d)	0.5	10

Table 5.2: The relationship between the number of graphene layers (N) and the ratio of I(2D) : I(G) of the graphene samples with Raman spectra shown in Figure 5.11.

However, the graphene samples produced using this method always exhibit high defect level, as the peak D in Figure 5.11 (a) - (d) were obvious no matter how thick the graphene sample is. The main reason for this effect was that the synthesis process of graphene at low temperature (< 900 °C) was not stable and the graphene domains were smaller than the normal size.

To reduce the defect level and improve the optical response of graphene films, we managed the fast-cooling CVD process by moving the furnace away from the sample side and expose the sample to room temperature directly. This approach shortened the cooling time into 15 minutes, at a temperature from 1000 °C to room temperature. Table 5.3 showed the parameters for operating the fast-cooling CVD processes.

	Reaction parameters			
Sample	Gas	Reaction time	Pressure	Cooling time
Figure 5.12 (a)	CH_4 30 sccm; Ar + 10% H_2 200 sccm	10 minutes	100 mTorr	15 minutes
Figure 5.12 (b)	CH_4 40 sccm; Ar + 10% H_2 200 sccm	10 minutes	100 mTorr	15 minutes
Figure 5.12 (c)	CH_4 50 sccm; Ar + 10% H_2 200 sccm	10 minutes	100 mTorr	15 minutes
Figure 5.12 (d)	CH_4 60 sccm; Ar + 10% H_2 200 sccm	10 minutes	100 mTorr	15 minutes

Table 5.3: The reaction parameters used in the fast-cooling CVD process to fabricating the graphene samples with Raman spectra shown in Figure 5.12.

Benefiting from the fast cooling approach, we deposited graphene sheets with low defects which were indicated in the Raman spectra shown in Figure 5.12. The D peaks of graphene samples are

much lower, compared to Figure 5.11. In this case, to realise the fabrication of graphene with the different number of layers, we modified the gas ratio here, typically by keeping the flow of Ar and H_2 as a constant (200 sccm) and changing the gas flow of CH_4 from 30 to 60 sccm. The related Raman spectra were illustrated in Figure 5.12. Additionally, the ratio of I(2D) : I(G) for different graphene samples were shown in Table 5.4.

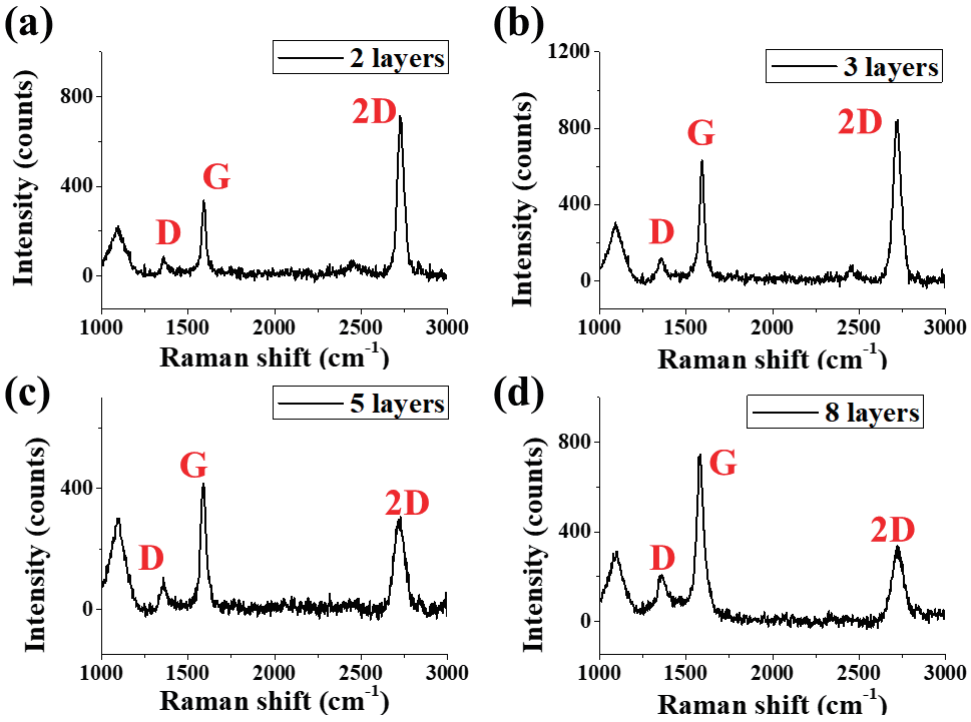

Figure 5.12: Raman spectra of fast-cooling graphene samples with different number of layers: 2 (a), 3 (b), 5 (c) and 8 (d).

Sample	I(2D) : I(G)	*N*
Figure 5.11 (a)	2	2
Figure 5.11 (b)	1.1	3
Figure 5.11 (c)	0.8	5
Figure 5.11 (d)	0.6	8

Table 5.4: The relationship between the number of graphene layers (*N*) and the ratio of I(2D) : I(G) of the graphene samples with Raman spectra shown in Figure 5.12.

5.4.2 AFM method

Another common way to check the surface morphology and the thickness of graphene is using AFM system with a resolution down to the atomic scale. We tested the 5-layer graphene whose Raman

spectra are shown in Figure 5.11 (b) using AFM approach with the help of our collaborators in the School of Chemistry.

Figure 5.13 showed the AFM scanning results of the graphene sample. The cantilever hosting tip scanned from graphene position (A) to the glass position (B), as shown in Figure 5.13 (b). The thickness variation curve (Figure 5.13 (b)) indicated that the average hight difference between A and B was about 2 nm and verified the number of graphene layers (5) estimated from Figure 5.11 (b).

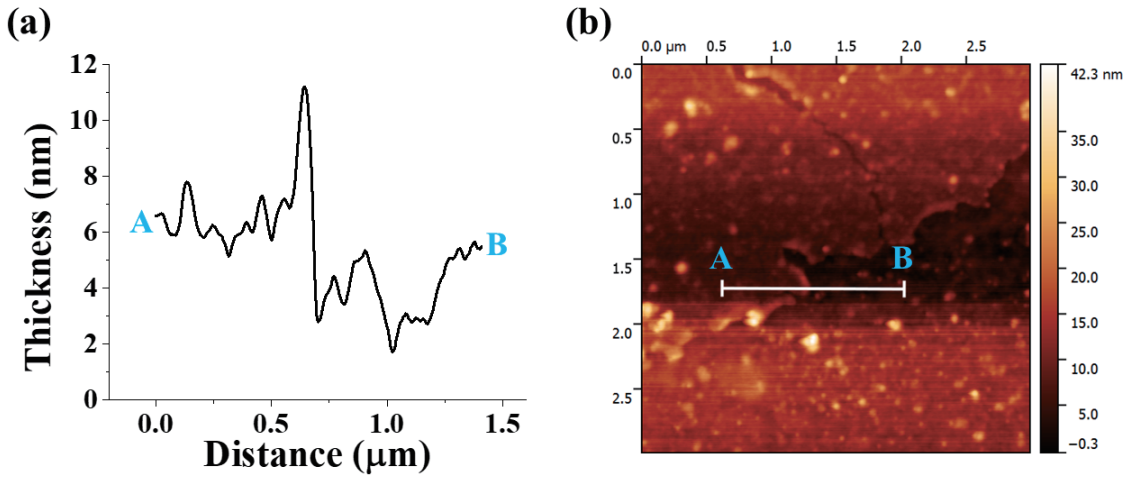

Figure 5.13: The AFM scanning results of a 5-layer graphene film located on a glass substrate. (a) The thickness variation along with the scanning from point A (graphene) to point B (glass). (b) The microscope image of the scanning route from point A to B.

The AFM approach can only qualitatively determine the thickness of the graphene layer, especially for single layer graphene, because of its low thickness. Additionally, the AFM system is in the School of Chemistry, and we do not have enough time to measure all the graphene samples. Therefore, we present this result as an assisted approach to characterise the number of graphene layers.

5.4.3 Absorption characterisation

The other optical characterisation method of graphene was based on the absorption measurement at the visible range. A collimated beam of 5 mm generated by a tungsten halogen light source was used to probe graphene/glass structures at normal incidence to the sample. The transmission (T) and reflection (R) of the samples were obtained by using optical spectrometers. Eventually, the absorption (A) was calculated using the equation of $A = 1 - T - R$.

First, the glass substrate was characterised before the graphene/glass samples. The measured transmission and reflection, and calculated absorption of the glass substrate (1 mm thick) were shown

in Figure 5.14. The absorption of the glass was indicated with a value of about 1%.

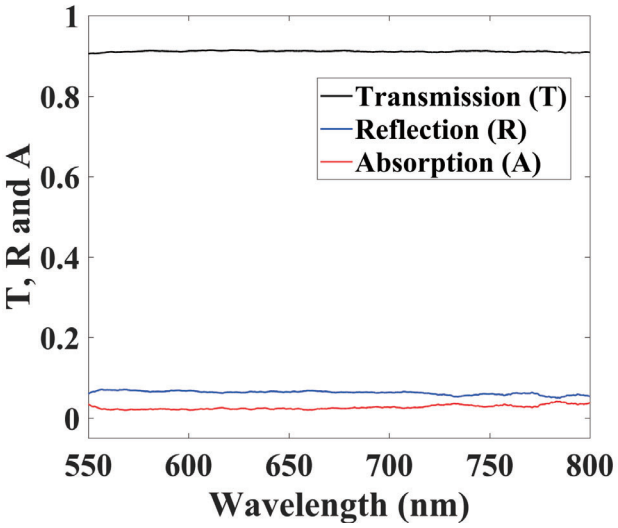

Figure 5.14: Transmission, reflection and absorption characterisation of the glass substrate.

The graphene samples with the number of layers of 2, 5, 8 and 10 were then characterised. They were transferred onto glass substrates, and their transmission and reflection were presented in Figure 5.15. The transmission of graphene samples decreased dramatically along with the number of layers increasing (Figure 5.15 (a)), while the reflection changed at the range of 5% (Figure 5.15 (b)).

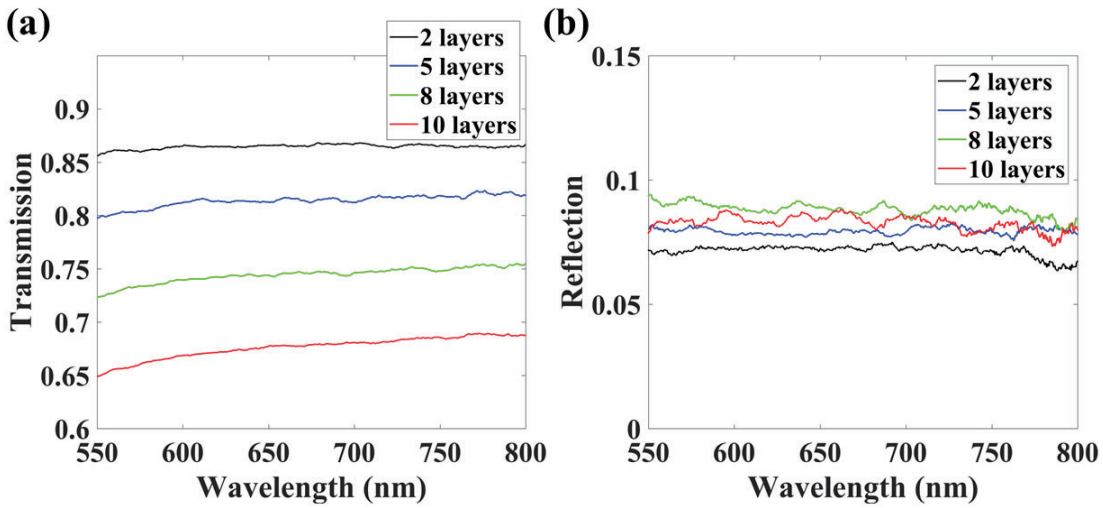

Figure 5.15: Transmission (a) and reflection (b) of the graphene samples with number of layers of 2, 5, 8 and 10, and transferred onto glass substrate.

Figure 5.16 showed the absorption of these graphene/glass samples. After subtracting the

absorption of the glass substrate, the absorption of 2-, 5-, 8- and 10-layer graphene were obtained as 5%, 11%, 17% and 24%. As the single layer graphene exhibited an absorption of 2.3% and the absorption of multilayer graphene can be simply estimated as the number of layers multiplies the single-layer absorption[141], the measured absorption verified the number of graphene layers which were estimated from the Raman spectra (Figure 5.11).

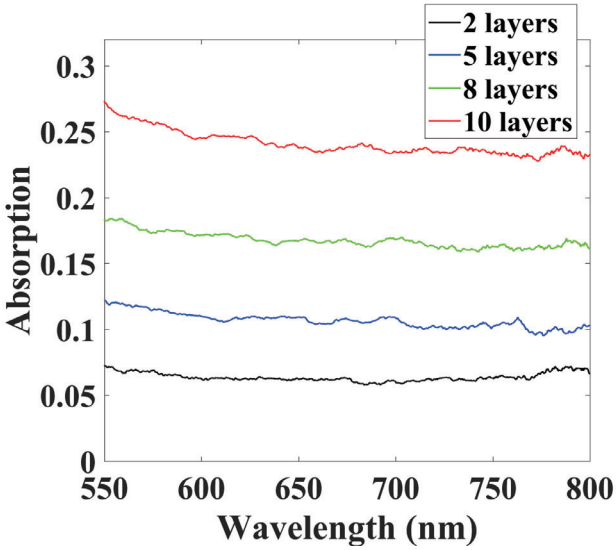

Figure 5.16: Absorption characterisation of the graphene/glass samples with different number of graphene layers of 2, 5, 8 and 10.

5.4.4 Electric characterisation

The electrical properties are important features of graphene, especially for the purpose of tuning graphene/dielectric multilayer structure via the application of voltage.

For this purpose, we deposited two 100-nm thick Au electrodes using e-beam evaporation on a glass substrate to measure the residence of a graphene sheet that placed across the electrodes (Figure 5.17).

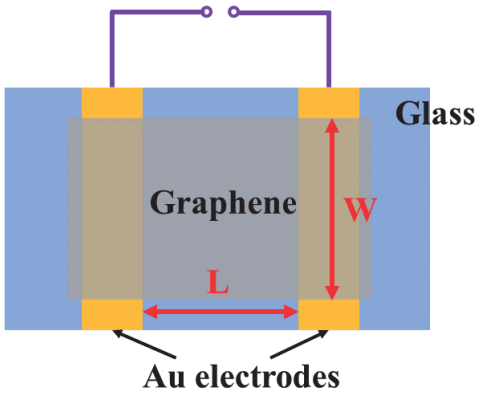

Figure 5.17: Apparatus diagram to measuring the conductivity of graphene samples. Graphene sheet locates on a glass substrate across two Au electrodes.

The resistance (R) of the graphene sheet was measured using a digital multimeter by probing the two electrodes after graphene transferred on the substrate across them. The length (L) and width (W) of the graphene area between the two electrodes were measured using a vernier calliper. Then, the resistivity (ρ) of graphene was determined via $\rho = RWt_g/L$, where t_g was the thickness of the graphene layer. The conductivity (σ) of graphene was the reciprocal of ρ, i.e. $\sigma = L/RWt_g$. As the thickness of graphene, t_g, was extremely thin and could not be determined accurately, a common method to characterise the electrical property of graphene was calculating the sheet resistance (R_s) via $R_s = RW/L$. This approach gives the conduction capability of graphene but not linked with the thickness of graphene. Table 5.5 presented the calculated R_s of the graphene sheets with different layers, and also the estimated σ of graphene using the t_g values obtained from Raman spectra.

Graphene	R_s (k$\Omega/\square$)	σ ($\times 10^3$S/m)
2 layers	123.1±30.2	12.1±3.0
5 layers	13.8±3.3	21.2±5.1
8 layers	9.7±2.0	38.6±6.2
10 layers	7.4±1.8	40.4±9.8

Table 5.5: The measured sheet resistance and conductivity of graphene films with different number of layers.

Along with the number of layers increases, the R_s of graphene reduced, and thus the conductivity increased. The R_s of the 2-layer graphene films we fabricated have a value around 123 k$\Omega/\square$, which is slightly higher than the reported value range (0.1 - 100 k$\Omega/\square$) from literature[194], but R_s of multilayer graphene sheets exhibits dramatical deceasing, down to about 7.4 k$\Omega/\square$, which promises the high electrical quality of the graphene samples for further optoelectronic applications.

5.5 Realisation of graphene/PMMA multilayer structure

This section demonstrates two approaches to realise the graphene/PMMA structure multilayer, via directly stacking and rolling methods, respectively.

Figure 5.18 sketched the directly stacking approach. A glass substrate was first cleaned by acetone and IPA ultrasonic bathing and a sacrificial layer (Omnicoat) was spin coated on the rigid substrate and baked for 1 minutes at 230°C (Figure 5.18 (a)). A 40 nm PMMA layer was then spun coated on top of the Omnicoat layer and baked at 180°C for 5 minutes (Figure 5.18 (b)), followed by a graphene layer transferred, via PET method (Figure 5.18 (c)). Next, the OmniCoat layer was removed using MF319 in a few hours and the graphene/PMMA film was released (Figure 5.18 (d)). Using the steps described above, we obtained several graphene/PMMA bilayer films (Figure 5.18 (e)) and stacked them together on another cleaned glass substrate, and the graphene/PMMA multilayer structure was obtained (Figure 5.18 (f)).

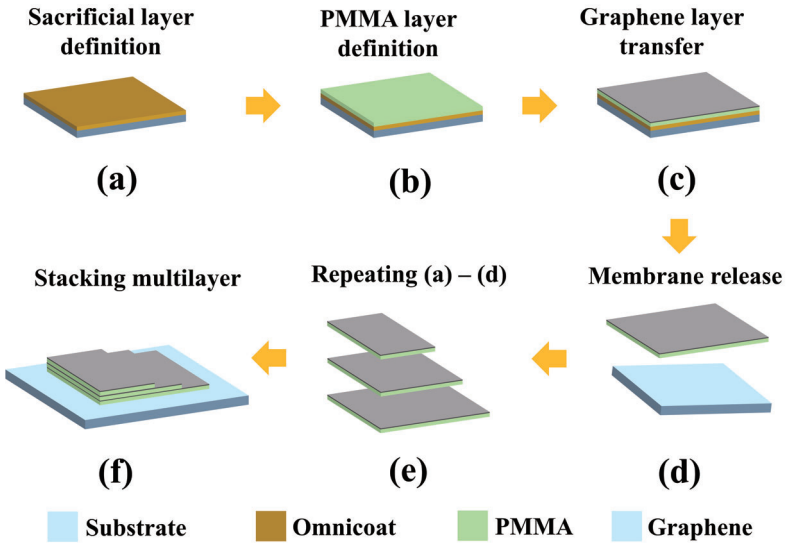

Figure 5.18: Diagram of fabricating graphene/PMMA multilayer structure using directly stacking approach. (a) The deposition of sacrificial layer (Omnicoat) on stiff substrate (glass). (b) and (c) The definition of graphene/PMMA bilayer. (d) Realising the graphene/PMMA bilayer structure via etching the Omnicoat layer. (e) Repeating the depositing and releasing steps of bilayers. (f) Stacking the graphene/PMMA bilayers to create the graphene/PMMA multilayer structure.

The stacking of 2 graphene/PMMA bilayers succeeded, as shown in Figure 5.19 (a). However, due to the poor toughness of thin PMMA film, the stacking structure shows obvious cracks and folds, especially for the second bilayer film, indicated by the microscope image shown in Figure 5.19 (b). Hence, we needed another method to realise the graphene/PMMA multilayer structure.

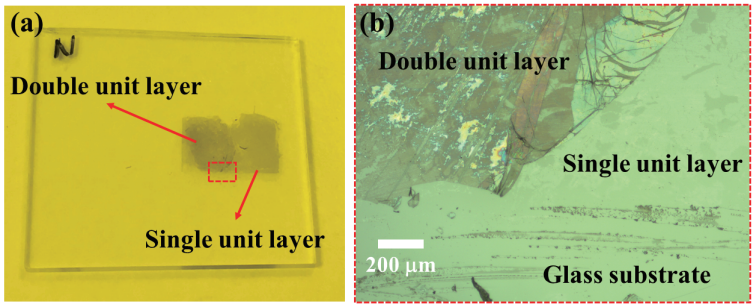

Figure 5.19: Photograph (a) and microscope image (b) of the double bilayer graphene/PMMA structure.

We tried the other method by rolling the single graphene/PMMA bilayer with an optical fibre, inspired by the work presented in Reference [195]. The diagram of the rolling precess was presented in Figure 5.20. First we obtained the free standing graphene/PMMA bilayer via the steps (a) - (d) sketched in Figure 5.19. Then, the bilayer sample was floated on DI water, and rolled on an optical fibre with a diameter of 125 μm (Figure 5.21 (a) and (b)).

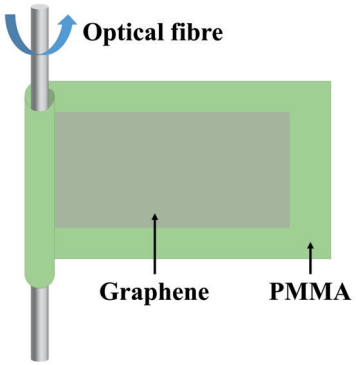

Figure 5.20: Sketch of the optical fibre rolling graphene/PMMA bilayer film.

For the rolling sample shown in Figure 5.21 (c), the rolling process finished six full circles, and the graphene/PMMA multilayer was obtained.

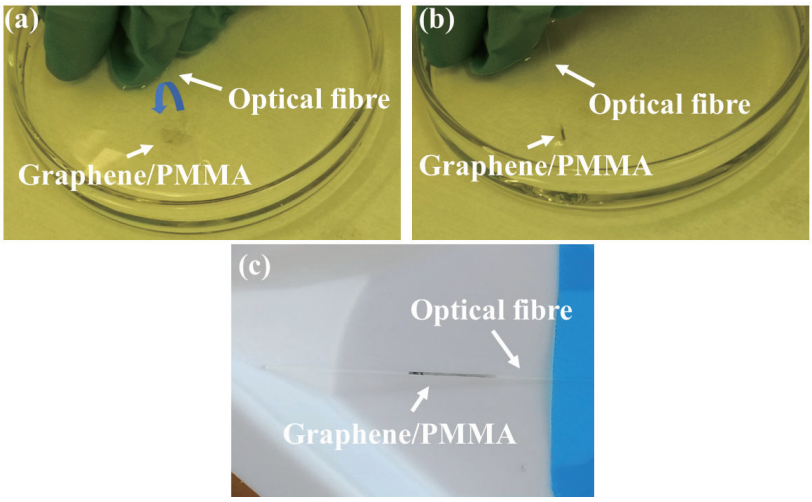

Figure 5.21: (a) and (b) Photographs of the process of the optical fibre rolling graphene/PMMA bilayer film. (c) The free standing rolled graphene/PMMA/optical fibre sample, fixed by blue tapes.

In order to determine the dispersion property of the graphene/PMMA/optical fibre sample, we measured the sample with a supercontinuum laser. The laser was focused onto the optical fibre sample using a 50x objective lens, and the transmitted and reflected signal were collected through an identical objective lens and analysed using two spectrometers. The transmission and reflection results of different parts of the sample were displayed in Figure 5.22.

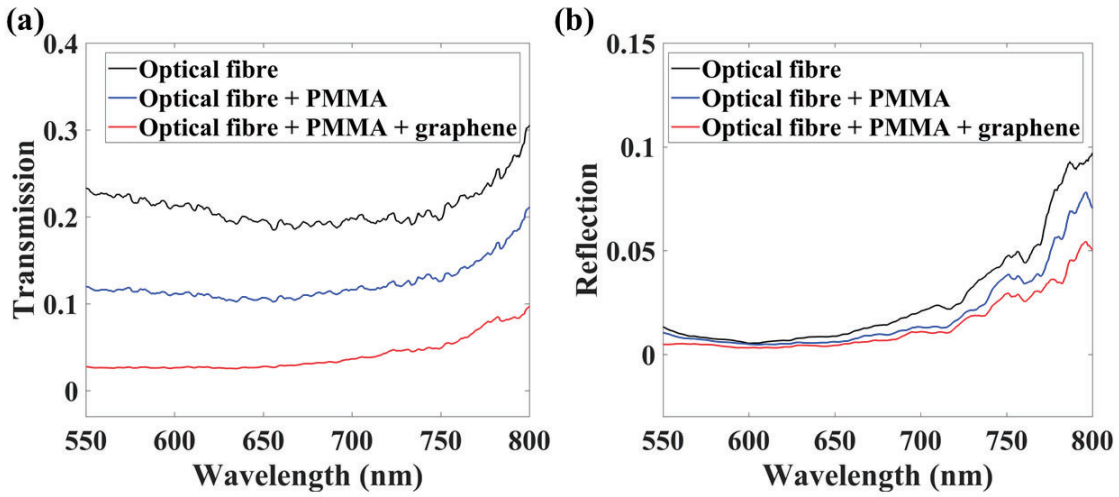

Figure 5.22: Transmission (a) and reflection (b) of different samples: blank optical fibre, optical fibre coated with multilayer PMMA film and optical fibre coated with graphene/PMMA multilayer structure.

The blank optical fibre, optical fibre coated with multilayer PMMA film and optical fibre coated

with graphene/PMMA multilayer structure were tested successively, and the transmission decreased dramatically, from about 25% down to about 3% (Figure 5.22 (a)). The reflection of these three parts are all lower than 10% (Figure 5.22 (b)). This was due to the curved surface of the optical fibre that scattered most of the light, and thus the collection of the spectrometer in the reflection path decreased dramatically. The microscope images of the graphene/PMMA/optical fibre sample shown in Figure 5.23 also verified this. Additionally, the roughness of the graphenePMMA film, caused by the folding and tearing happened in the rolling process, also enhanced the scattering effect.

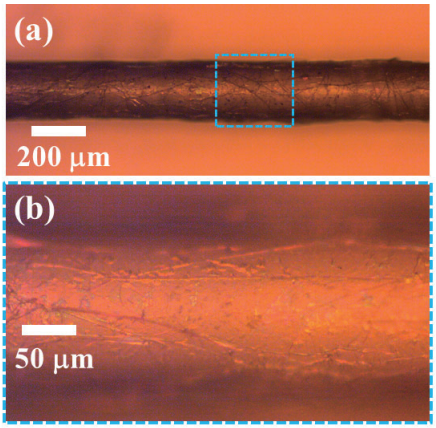

Figure 5.23: (a) Microscope images of the optical fibre coated with graphene/PMMA multilayer structure. (b) The zoomed-in image of the area marked in (a) with a dashed blue frame.

We were aiming to realise the ENZ response using this rolled-up multilayer graphene/PMMA structure, but due to the poor strength and high roughness of the released PMMA layer, we did not manage that and focused onto the rigid graphene/dielectric multilayer structure in the infrared regime.

5.6 Electrical tuning graphene/dielectric structure at infrared range

In this section, we present the other graphene/dielectric model, typically the graphene/ZnSe structure operated at infrared range (i.e. 10.6 μm). The ZnSe thin film can be deposited onto different substrates using e-beam evaporation approach. Figure 5.24 present the 100-nm thick ZnSe film evaporated on glass or Si substrates.

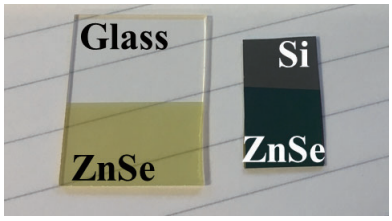

Figure 5.24: Photographs of ZnSe layers with the thickness of 100 nm, deposited on glass and Si substrates, using e-beam evaporation method.

The permittivity of ZnSe (ϵ_{ZnSe}) follows the relationship[196] of

$$\epsilon_{ZnSe} = 1 + \frac{4.45813734\lambda^2}{\lambda^2 - 0.200859853^2} + \frac{0.467216334\lambda^2}{\lambda^2 - 0.391371166^2} + \frac{2.89566290\lambda^2}{\lambda^2 - 47.1362108^2} \tag{5.6}$$

where λ is the wavelength with the unit of μm of the incident light.

Using the optical characterisation method shown in Chapter 3, we measured the transmission and reflection (Figure 5.25 (a)) of the ZnSe thin film on glass substrate shown in Figure 5.24. The refractive index (n+ik) was then retrieved and shown in Figure 5.25 (b), and fitted the reference value very well. Therefore, we estimated the refractive index of ZnSe as the value of 2.4, at the wavelength of 10.6 μm, according to Reference [196].

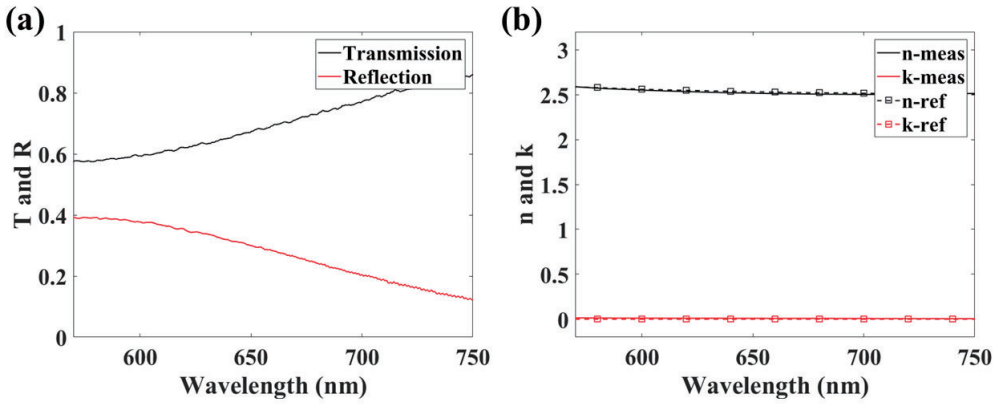

Figure 5.25: Optically characterisation of the 100-nm thick ZnSe layer at visible range. (a) Meaured transmission (T) and reflection (R) of the ZnSe layer. (b) Retrieved refractive index (n-meas, k-meas) of the ZnSe layer, compared to the reference value (n-ref, k-ref)[196].

We considered the thickness of ZnSe unit layer as 100 nm and the effective permittivity of the graphene/ZnSe multilayer structure was simulated along with the changing of applied voltage, based on the EMT. Figure 5.26 illustrated the numerical result of the effective permittivity ($\epsilon_{\perp}$) of the graphene/ZnSe multilayer structure. Here, we focused on the wavelength range around 10.6 μm, and

the zero permittivity condition occurred at the applying voltage equalling to about 1 V. Additionally, the effective permittivity turned from positive to negative and showed obvious value changing when the voltage applied varying from 0 to 5 V. These results offered the chance to tune the ENZ region by applying different voltage onto the graphene/ZnSe multilayer structure.

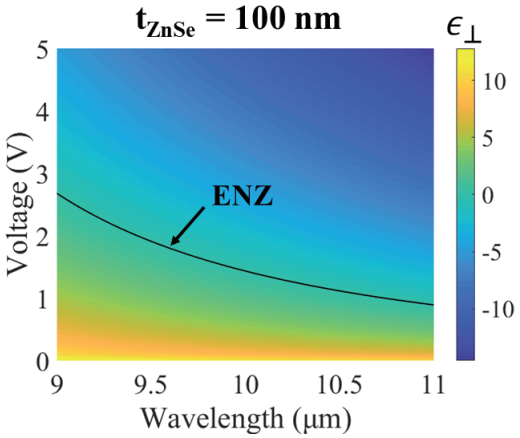

Figure 5.26: The calculated effective permittivity ($\epsilon_\perp$) of the graphene/ZnSe multilayer structure formed by unit layers of single-layer graphene and ZnSe layer with thickness (t_{ZnSe}) of 100 nm. The zero permittivity (ENZ) regions are marked with solid black lines.

At the wavelength range around 10.6 μm, low-loss Si exhibited high transmittance[197] as it absorption is small. Therefore, it was a good candidate for hosting the graphene/ZnSe structure as a substrate. Before realising the multilayer structure, we designed and fabricated an 1-bilayer structure consisted of graphene and ZnSe unit layers, which sketched in Figure 5.27 (a). An 100 nm ZnSe film was first deposited onto a low-loss and high-resistance Si wafer, followed by the definition of Au electrodes with thickness of 50 nm. Finally, the graphene film was transferred onto the ZnSe layer via PET method, across two electrodes as well.

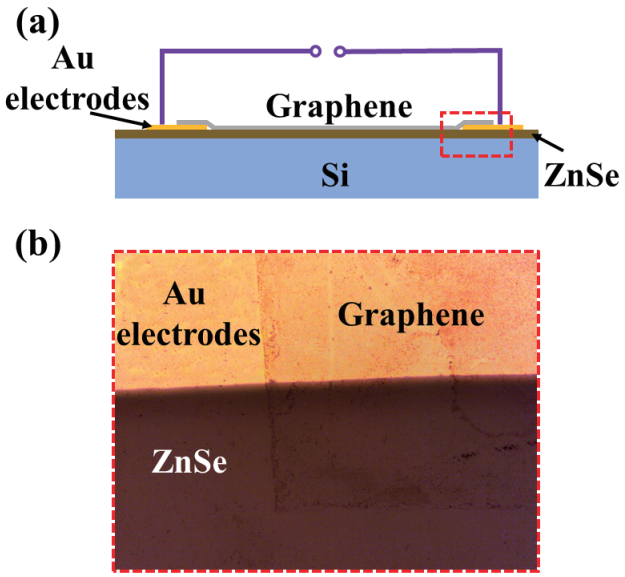

Figure 5.27: Diagram (a) and microscope image (b) of the 1-bilayer graphene/ZnSe structure.

Figure 5.27 (b) showed the microscope image of graphene layer covered on the surface of both the ZnSe layer and Au electrode.

A carbon dioxide (CO_2) laser was used to detect the optical response of the graphene/ZnSe sample. The sample was mounted on a translation stage and probed by the collimated laser beam at normal incidence, with a wavelength of 10.6 µm and beam size of 3 mm. The transmitted signal was collected by a power detector. The setup was sketched in Figure 5.28.

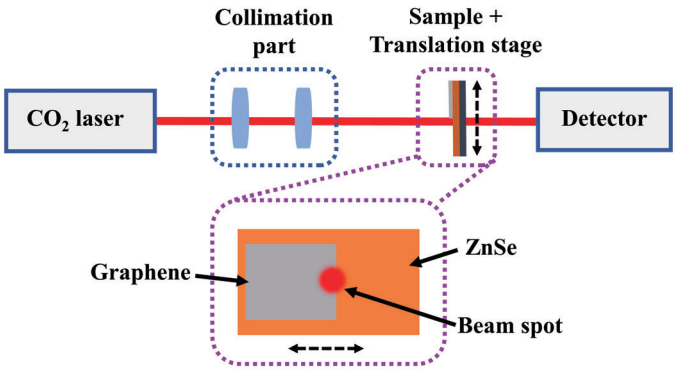

Figure 5.28: Diagram of the optical path used to detect the transmitted power of the graphene/ZnSe sample, and also the diagram of sample stage moving to exposing different parts of the sample to the laser beam.

In order to calibrate the laser stability, we measured the power of the laser transmitting through the air and the blank Si substrate with the thickness of 100 µm at normal incidence. The power of the

laser exhibit unstable oscillation (Figure 5.29 (a)), while the osculation became obvious after the laser transmitted through the Si wafer (Figure 5.29 (b)). We believed that this oscillation effect was caused by two reasons: first, the instability of the laser could be enhanced by the thermal effect of the Si substrate; second, the etalon effect might occur inside the Si wafer. Further investigation would be needed to determine the reason.

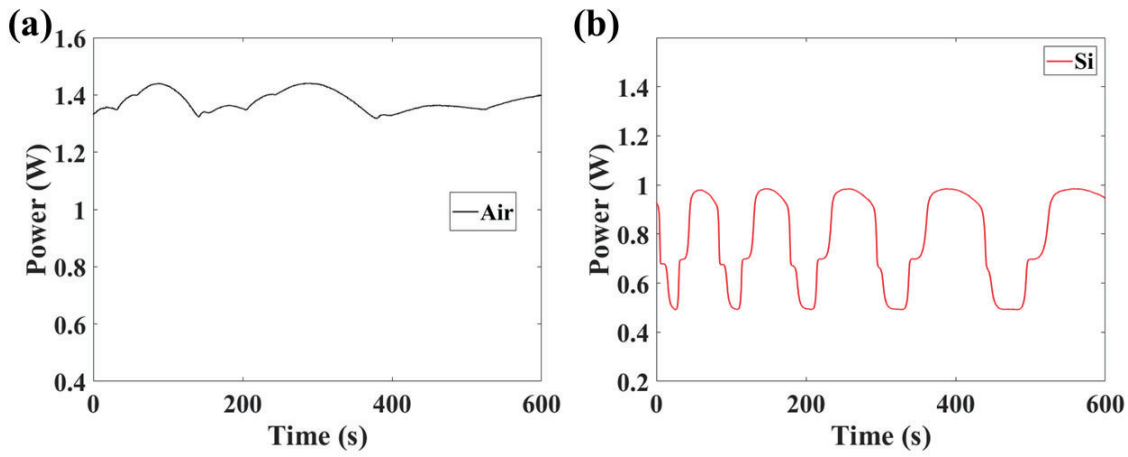

Figure 5.29: The power changing of the CO_2 laser transmitting through air (a) the blank Si substrate (b) at normal incidence along with the time increasing.

Considering the unstable power of the incident laser transmitted the Si substrate, we set the sample stage moving along the direction perpendicular to the laser beam. The moving distance is for one period is 2 cm, and the moving period of the stage is 3 seconds, including a 1 second waiting time at both moving end positions. This approach was designed to collect the transmitted power of the laser propagating through both the graphene and substrates at a stable power period. Using this approach, we tested a graphene/Si sample and the transmitted power changing along with time as illustrated in Figure 5.30. The stage moved fast enough to ensure that the laser propagated through graphene/Si and blank Si structure alternatively at every stable-power period (Figure 5.30 (a)). Additionally, in one stable-power period, we could determine the average power of laser propagating through graphene/Si structure (G) or blank Si substrate (S) (Figure 5.30 (b)). The transmission of the graphene layer was then obtained via the ratio between average power (G) through the graphene/Si structure and average power (S) through blank Si substrate.

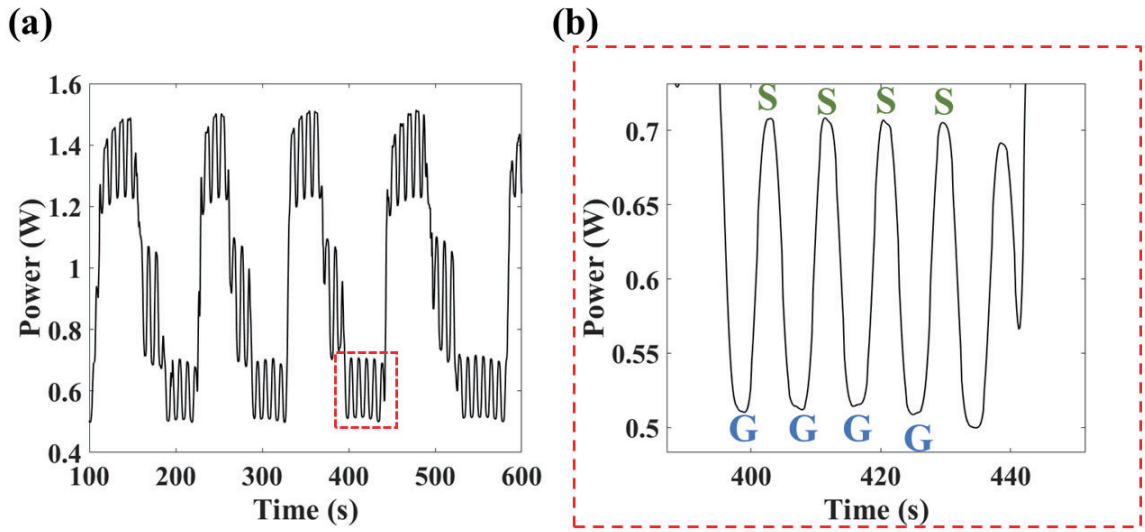

Figure 5.30: (a) Transmitted power of laser propagating through graphene/Si structure and blank Si substrate as a function of time. (b) The transmitted power through graphene/Si structure (G) or blank Si substrate (S), zoomed in from the marked region in (a) by a red dash frame.

Using the same setup and test method, we measured the transmission of bilayer graphene/ZnSe structure and blank ZnSe film on the Si substrate at different applying voltage conditions. Figure 5.31 (a) showed that the transmission of graphene/ZnSe structure decreased when we applied higher voltage, compared to the blank ZnSe film. This phenomenon partly verified that the effective permittivity of the graphene/ZnSe structure decreased along with the increasing voltage, according to the simulated transmission of the graphene/ZnSe/Si structure, using Fresnel's equations demonstrated in Chapter 3.

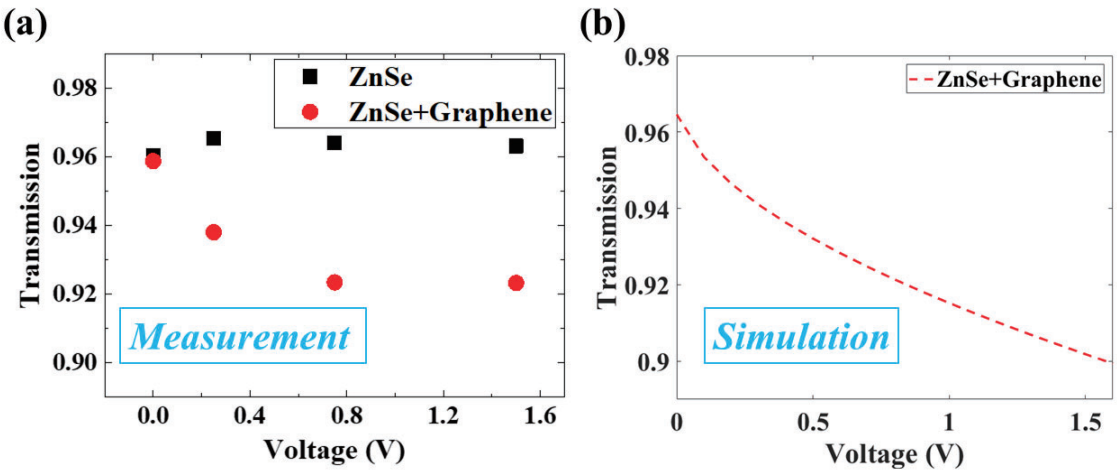

Figure 5.31: (a) Measured transmission of bilayer graphene/ZnSe structure and blank ZnSe film on the Si substrate with different voltage applied. (b) The calculated transmission of the graphene/ZnSe/Si structure at the incident wavelength of 10.6 µm and with different voltage applied.

5.7 Conclusion

We demonstrated the fabrication process of graphene using CVD approach with different parameters and found that the fast cooling process was required to create low-defective graphene sheet. We characterised the number of layers and optical properties of graphene films by using Raman spectroscopy method, AFM method, absorption determination method and electrical approach.

By using directly stacking and optical fibre rolling method, we created graphene/PMMA multilayer membranes, but with high roughness and poor optical response.

In the infrared regime, we designed and fabricated an 1-bilayer grapheneZnSe structure. By applying different voltage, we found that the transmission of this structure decreased along with the voltage increasing. We believe that these results will open a door toward the tunable ENZ MMs and further applications.

Chapter 6

ITO and applications associated with EBID

This chapter presents the works about the fabrication, characterisation and applications of isotropic ENZ material made of ITO. The fabrication of ITO using sputtering approach is demonstrated first, followed by the electrical and optical characterisation of ITO samples fabricated under different conditions. We then present the work about a fabrication technique based on EBID and discuss its use for the enhanced optical chirality based ITO/nanohelix hybrid platforms. Finally, we demonstrate the photonic trimming of the emission of QDs located in different platforms via decorating the QDs using EBID approach, and also summarise the results and further perspectives of the work combining ENZ platform and QDs.

6.1 Fabrication of ITO

There are several methods for fabricating ITO thin films, such as evaporation[198, 199], CVD[200], spray pyrolysis[201], sol-gel approach[202] and magnetron sputtering[203]. Among them, magnetron sputtering is the most popular and reliable approach due to its stable deposition process, high reproducibility and uniformity, especially for large-area deposition[204, 205]. In the magnetron sputtering process, gaseous plasma and high-energy ions (e.g. Ar^+) is generated and eroded onto the target material to produce the free atoms which travel through the vacuum environment and deposit onto a substrate to form a thin film. Additionally, the magnetron sputtering has two kinds of plasma discharge mode, i.e. direct current (DC) and RF. The DC sputtering is a popular approach for depositing materials with low resistivity, for example, metals and TCOs. However, the ITO created by DC sputtering is usually amorphous and shows poor surface morphology, which will lead to unexpected optical responses[206], which is not suitable for our ENZ purpose. On the contrary, the RF sputtering offers an effective approach to deposit low-resistivity and high transparency crystalline

ITO thin films. Hence, we use the RF sputtering method to fabricate ITO layers for our ENZ and other applications.

The RF sputtering process of ITO was completed in a commercial system (ANGSTROM ENGINEERING), sketched in Figure 6.1. The substrate (glass) was first cleaned with ultrasonic bathing of acetone and IPA for 5 minutes each and mounted onto the sample holder in the chamber. The holder was able to heat the substrate and monitor the temperature of the sample. Then the chamber was pumped into an ultra-low pressure (2×10^{-7} Torr), and the substrate was heated to the desired temperature. After that, the required gases (Ar and O_2) were injected and the deposition started. In order to generate plasma, a high voltage was applied between the cathode (connected to target) and the anode (connected to the sample holder and ground). A magnet system was also used to confining the plasma around the surface of target and avoiding the damaging of the sample substrate.

Additionally, with the help of a RF generator with 13.56 MHz, electrons were created in the sputtering gas and accelerated away from the cathode causing collisions with nearby gas atoms. These collisions led to an electrostatic repulsion by knocking off electrons from the sputtering gas atoms, i.e. ionisation. The positive gas ions were then accelerated towards the cathode and hit the surface of the target material, typically the ITO here. The sputtering gas typically had a high molecular weight, such as Ar, to obtain high collision energy. The released target atoms with enough kinetic energy reached the substrate and formed the film. The deposition of ITO was done with a rate of 0.05 nm/s, at the pressure of 3 mTorr. The deposition rate and thickness of the film were monitored by a quartz crystal detector, which was calibrated by modifying its tooling factor. During the sputtering process, the sample holder was rotating to improve the smoothness of the ITO film. Finally, the deposited ITO film was post-annealed for 30 minutes at the temperature the same as the one of the deposition process.

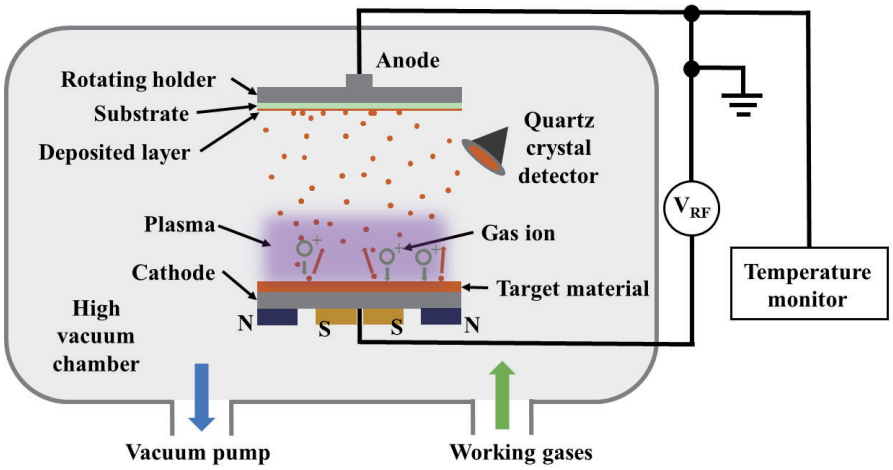

Figure 6.1: Diagram of the RF sputtering system, formed by high vacuum chamber, gas flowing system, target material (ITO), RF electric field generator, magnets for confining electric field, rotating sample holder which can also increase and monitor the temperature of sample, and quartz crystal detector for monitoring the deposition rate and thickness.

The electrical and optical properties of ITO were influenced by the sputtering parameters, typically, the RF power, the gas ratio (Ar:O_2) and sample temperature, etc. We set the RF power at 70 W with different gas ratios and sample temperatures. The relationship between the fabrication conditions and the properties of ITO will be presented and discussed in the characterisation part.

Figure 6.2 shows a typical ITO sample with a thickness of 100 nm, deposited on glass substrate with a gas ratio of Ar:O_2=20:1 and baking temperature of 300 °C. The thickness of the ITO film was measured using a surface profiler. High transparency could be observed by visual inspection.

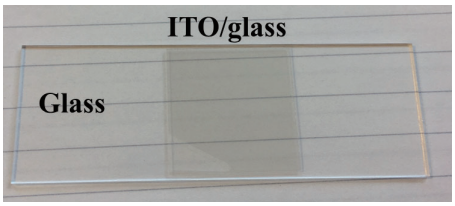

Figure 6.2: Photograph of a 100-nm ITO film deposited on a glass substrate.

6.2 Charaterisation of ITO

The ITO films deposited under different fabrication parameters were characterised using both electrical and optical approaches. The sheet resistance (Rs) and ENZ measurement results of different ITO samples are presented here.

6.2.1 Electrical characterisation

Conductivity (σ) is a significant characteristic of ITO and reflects the carrier density of ITO, which also influences the ENZ region, i.e. the higher carrier density, the shorter ENZ wavelength[62]. Here we used Rs to represent the conductivity of ITO with an inverse relation of $Rs = 1/(t\sigma)$, where t was the thickness of the film. The Rs of a ITO film was also determined using the equation of $Rs = RW/L$ with measured resistance (R), width (W) and length (L) of the film. Therefore, we could quantitatively determine the electrical property of ITO by measuring its Rs.

We set the fabrication conditions as two groups. Group A samples had a constant deposition temperature of 300 °C and Ar flow of 20 sccm. The O_2 flow varied from 0 to 6 sccm. Group B samples had a constant gas ratio of Ar:O_2=20:0 and various deposition temperature from 100 to 450 °C. All samples were deposited at a RF power 70 W and post-baking time of 30 minutes. The parameters of the fabrication were listed in Table 6.1.

	Reaction parameters	
Sample	Deposition temperature	O_2 flow
A-1	300 °C	0 sccm
A-2	300 °C	1 sccm
A-3	300 °C	2 sccm
A-4	300 °C	3 sccm
A-5	300 °C	4 sccm
A-6	300 °C	5 sccm
A-7	300 °C	6 sccm
B-1	100 °C	0 sccm
B-2	150 °C	0 sccm
B-3	200 °C	0 sccm
B-4	250 °C	0 sccm
B-5	300 °C	0 sccm
B-6	350 °C	0 sccm
B-7	400 °C	0 sccm
B-8	450 °C	0 sccm

Table 6.1: The parameters used in the deposition of ITO films with the thickness of 100 nm.

The measured Rs as a function of O_2 flow and deposition temperature was presented in Figure 6.3. All the Rs values were determined as the average of three measurements and the uncertainty of each measurement was shown in the graph.

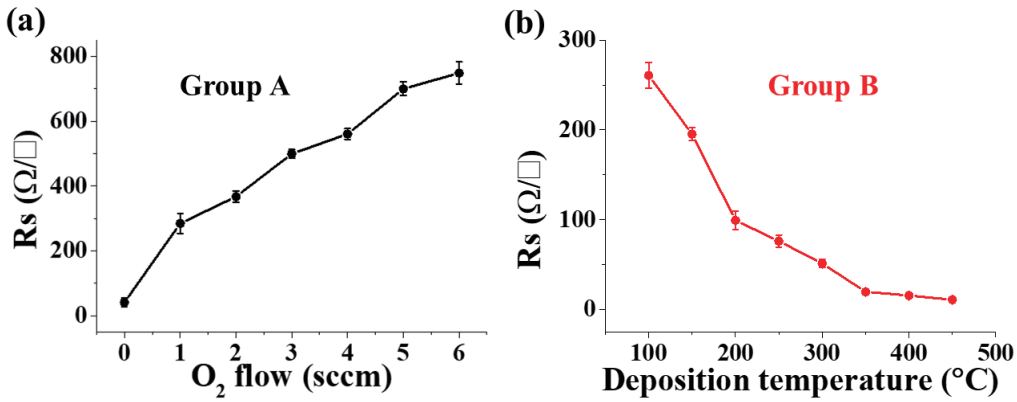

Figure 6.3: The Rs of ITO samples deposited under conditions of different O_2 flows (a) and deposition temperatures (b).

For group A, when the other parameters were fixed, the Rs of ITO increased from 50 to 360 Ω/□, along with the increasing of the O_2 percentage. This was because the high O_2 concentration led to a higher proportion of oxygen element in the ITO molecular and thus reduced the conductivity of ITO[207, 208]. To achieve low Rs and make the ENZ range shorter than 1600 nm, we used the sputtering gas with only 20-sccm Ar at group B. The Rs reduced along with the decreasing of the deposition temperature, with the value down to about 10 Ω/□ at 450 °C.

6.2.2 Optical characterisation

In order to characterise the optical properties of ITO films in the NIR regime and determine the zero-permittivity wavelength, we used a setup similar to the characterisation apparatus used in Chapter 3, but with the elements working at NIR range. A supercontinuum laser with a wavelength range of 300-1600 nm was used to probe samples at normal incidence with s polarisation. The collimated beam propagated through samples and then the transmitted and reflected signals were collected and spectrally analysed with an optical signal analyser (OSA). To determine the influence of the fabrication parameters on the ENZ region of ITO films, all the ITO samples tested in this part had the same thickness of 100 nm.

First, we investigated the effect of the gas ratio on the optical response of ITO films. The gas flow of Ar was fixed at 20 sccm and the flow of O_2 was set as 0, 1 and 2 sccm.The deposition power and temperature were 70 W and 300 °C, respectively. The other fabricated parameters were all the same for different samples as well. The transmission (T) and reflection (R) of these three ITO films were presented in Figure 6.4.

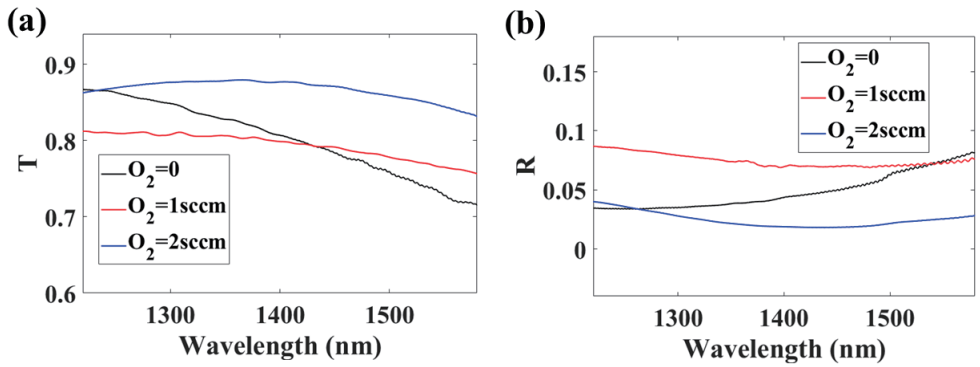

Figure 6.4: The transmission (a) and reflection (b) of different ITO films which were fabricated at different gas atmospheres, i.e. Ar flow of 20 sccm and O_2 flow of 0, 1 and 2 sccm.

As the flow of O_2 increased from 1 to 2 sccm, the transmission of the ITO film increased by about 5%, while the reflection reduced by about 5%. In these conditions, the transmission and reflection did not change much along with the wavelength increasing. These phenomena were due to the oxygen proportion increasing in the ITO molecular, and thus the ITO became more dielectric. This effect was also verified by the decreasing of conductivity, discussed in the electrical characterisation part. When the flow of O_2 decreased into 0, the transmission and reflection of ITO showed high sensitivity to wavelength, i.e. the transmission dropped more than 5% and the reflection increased by about 5% when the wavelength varied from 1200 nm to 1600 nm. This was caused by the presence of the ENZ region.

We obtained the real and imaginary parts of permittivity of the ITO films using the standard retrieval method introduced in Chapter 3, based on the transmission and reflection shown in Figure 6.4 (a) and (b). The retrieved epsilon was plotted in Figure 6.5, as a function of wavelength.

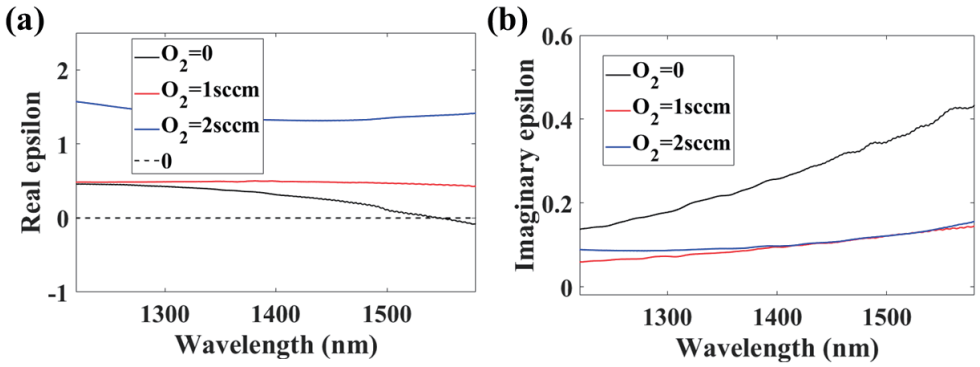

Figure 6.5: The retrieved epsilon (real (a) and imaginary (b) parts) of the ITO samples that retrieved based on the transmission and reflection presented in Figure 6.4.

The real part of epsilon of the ITO samples decreased along with the decreasing of the O_2 flow during the deposition (Figure 6.5 (a)). The ITO samples with 1- and 2-sccm O_2 flow in fabrication had a constant value of the real part of epsilon, at about 0.5 and 1.6, respectively, while the sample fabricated without O_2 had a decreasing value as the function of wavelength and the value crossed zero at the wavelength of about 1550 nm. In addition, the sample fabricated with O_2 flow of 1 and 2 sccm exhibited low optical loss, but the sample with no O_2 flow in fabrication showed the higher value of the imaginary part of the epsilon, which also was highly sensitive to the wavelength (Figure 6.5 (b)). These effects were also due to the dielectric and ENZ response of different samples. Based on this, we estimated that the ITO film fabricated under the condition with higher O_2 flow (>2 sccm) and other same parameters would not show ENZ response at the wavelength shorter than 1600 nm. Additionally, this also requested us to fabricate the ITO films at a low or zero O_2 atmosphere to achieve the ENZ condition at NIR range. Additionally, this is why we did not measure all the ITO samples in group A.

Then, we controlled the gas atmosphere of the only Ar with a flow rate of 20 sccm, and changed the deposition temperature (Tem) during the fabrication of ITO samples. The deposition temperature was set as 100, 200, 300, 350 and 400 °C, respectively. The transmission (T) and reflection (R) of these ITO films were shown in Figure 6.6. The T and R did not change correspondently with the increasing temperature, so we need to check the permittivity of these samples. The retrieved epsilon based on these transmission and reflection results showed clearly relationship between the ENZ range and the deposition temperature, as sketched in Figure 6.7.

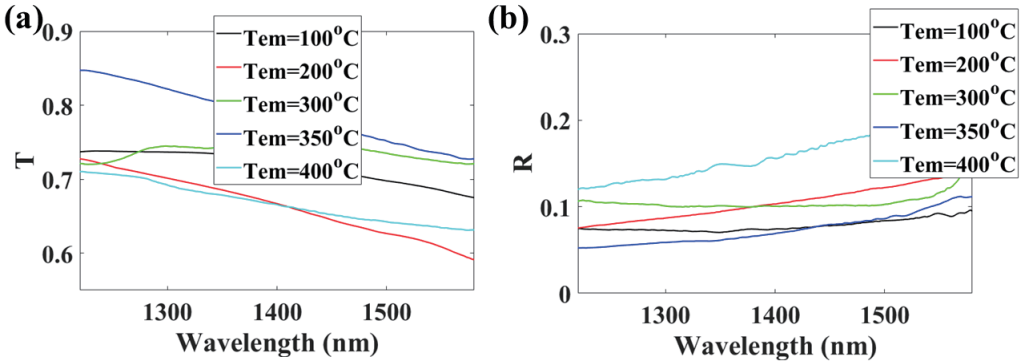

Figure 6.6: The transmission (a) and reflection (b) of different ITO films which were fabricated at different deposition temperatures, varied from 100 to 400 °C, and the gas atmosphere of only 20-sccm Ar.

At the wavelength range from 1200 to 1600 nm, the real part of epsilon of the ITO samples

decreased along with the increasing of the deposition temperature. Additionally, the zero-permittivity wavelength went shorter for higher deposition temperature, for example, the ITO sample with the deposition temperature of 400°C showed zero permittivity (real) at the wavelength of about 1280 nm, while the sample with the deposition temperature of 300°C had a permittivity (real) reaching zero at the wavelength of about 1550 nm. Besides, Figure 6.7 (b) showed the imaginary part of the epsilon of these ITO samples and indicated a general decreasing trend as the deposition temperature increased. This is due to the higher temperature was able to improve the smoothness and uniformity of the ITO thin films[209].

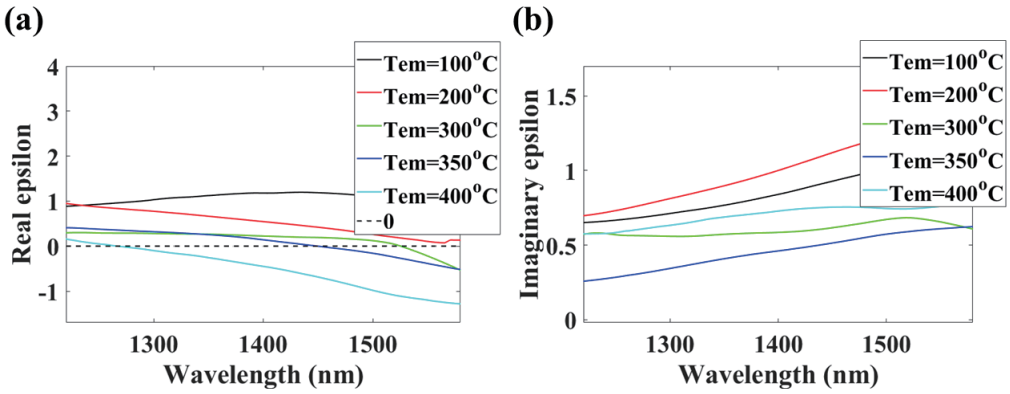

Figure 6.7: The retrieved epsilon (real (a) and imaginary (b) parts) of the ITO samples that had the transmission and reflection presented in Figure 6.6.

These results also promised that the ENZ condition of the ITO film could be manipulated by controlling deposition parameters, such as the gas ratio and deposition temperature, which agreed to the results reported in literature[210–212].

6.3 Applications of ITO associated with EBID

As ITO shows high transparency, low resistivity and ENZ effect, we plan to combine ITO platform with some nanopatterns to realise typical optical response and applications. The ENZ properties of ITO at NIR range promise the possibility to realise the applications such as peculiar light propagation[126, 213, 214] and nonlinear response[215, 216]. Additionally, the manipulating of the optical response can be achieved via introducing nanoplasmonic features[217–219]. By decorating the ENZ ITO film with typical nanopatterns, we can obtain specific optical properties. For instance, the tuning of nanoantenna resonance due to the presence of ITO substrate in the ENZ regime has been reported in literature[220]. The fabrication of these nanofeatures needs nanostructuring approaches,

e.g. the standard EBL technique, which require complex preparation processes and limit the freedom of nanopattern design in some ways. Here we propose a nanostructure fabricating method based on direct EBID. Without wet lithographic steps and exact spatial arrangement, the EBID approach is able to create 3D metal and dielectric features with nanometric resolution and positional accuracy. Using this method, we design a ITO/nanohelix platform to realise the enhancement of optical chirality. The following subsections will first present the EBID process and then the initial results.

6.3.1 EBID process

To fabricate nanofeatures using EBID approach, we used a Raith E-line plus electron beam lithographic system, as sketched in Figure 6.8. We take the deposition of W helix array on ITO substrate as an example.

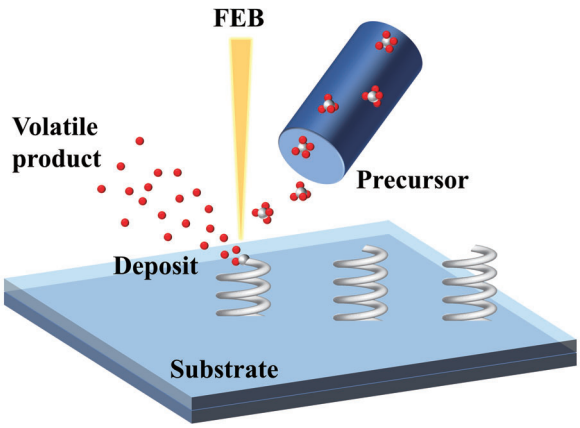

Figure 6.8: Diagram of the EBID process to depositing W nanohelices on top of the ITO substrate.

EBID approach realised the deposition by focusing electron beam onto specific gas precursors, which injected in the chamber in the proximity of the target[221, 222]. The desired gases were injected locally by a gas injection system. When the precursor gases containing target compound is added to the system, gas molecules are cracked by the FEB at the focused point and the free atoms reunion at the patterning area which leads to a deposition structure. To deposit W, a suitable precursor was used here, based on the compound tungsten hexacarbonyl ($W(CO)_6$). The precursor gas molecules split under the probe of the FEB, followed by the reunion and solidification of W and carbon (C) atoms. We used a deposition current of 150 pA, an acceleration voltage of 3 kV, and a dose of 1 C/cm^2, at room temperature.

Using EBID method, we have managed the fabrication of various nanopatterns on different substrates, which presented in Figure 6.9.

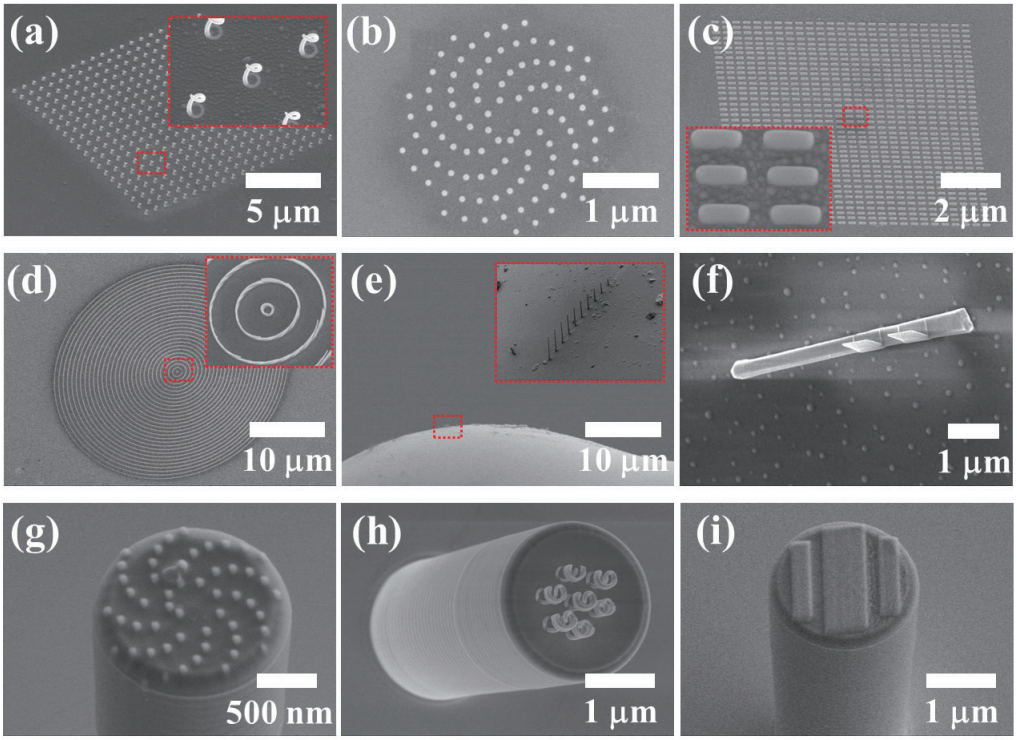

Figure 6.9: SEM images of different nanopatterns deposited on different substrates using EBID approach. (a) W nanohelix array on Si substrate. (b)-(d) Pt spiral dot matrix, nanoattenna and concentric microcircles on ITO substrates. (e) Standing Pt nanoantennas on ITO coated microsphere. (f) Standing Pt nanoantenna on a NW embedding QDs. (g)-(h) Pt spiral dot matrix and nanohelices on micropillars embedding QDs.

6.3.2 Optical chirality of nanohelix on ITO substrate

Here, we show the nanohelix on an ITO substrate fabricated using EBID method, to achieve the chiral response of different circular polarised light.

Chiral response at both photonic and plasmonic regime attracts wide attention nowadays[223, 224]. Specifically, the helical MMs, as 3D chiral features, offers an approach to manipulate the optical behaviour of circularly polarised light[40]. It has been reported in both theory[23, 225] and measurement[40, 226] that the metal helix structures show the circular-polariser phenomenon in broadband, i.e. the helix is able to block the circularly polarised light with same rotation (polarisation), but permit through the light with reversed rotation (polarisation).

We design a structure formed by W nanohelix arrays and the ITO substrate, illustrated in Figure

6.10 (a). A ITO thin film is deposited on a cleaned glass substrate and the W nanohelices are located on the surface of the ITO layer periodically. Figure 6.10 (b) sketched an individual helix with a right-hand rotation. According to refs[225, 227], this helix array shows high transmission for the LHCP light but extremely low transmission for the RHCP light. Additionally, the array period (P), diameter (D), wire diameter (d), pitch hight (H) and pitch number (N) will determine the working wavelength. In general, larger N and H leads to broader working wavelength band, larger P, D and d shifts the centre of the working wavelength to longer range[225, 227].

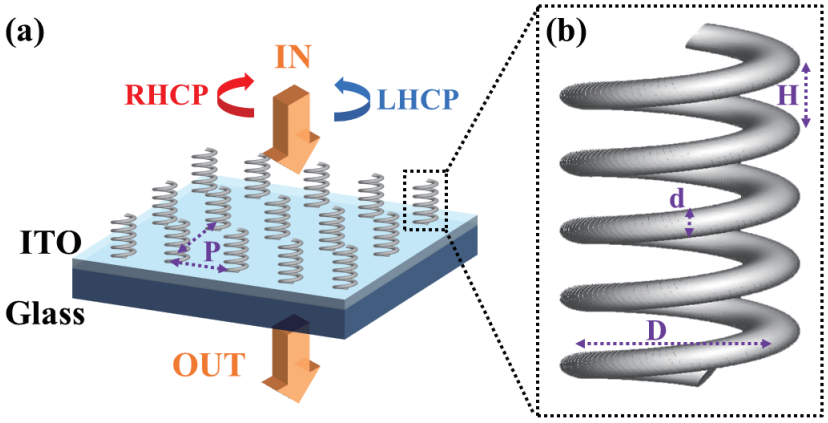

Figure 6.10: (a) Diagram of the W nanohelix array with a period of P locating on ITO/glass substrate. (b) Diagram of an individual W nanohelix with diameter D, wire diameter d and pitch hight (axial period) H.

Figure 6.11 (a) presented the SEM image of the W nanohelix array with an array period of about 1.5 µm. Figure 6.11 (b) showed the magnified SEM image of W nanohelices with the size parameters of D≈600 nm, d≈20 nm, H≈700 nm and N=2.

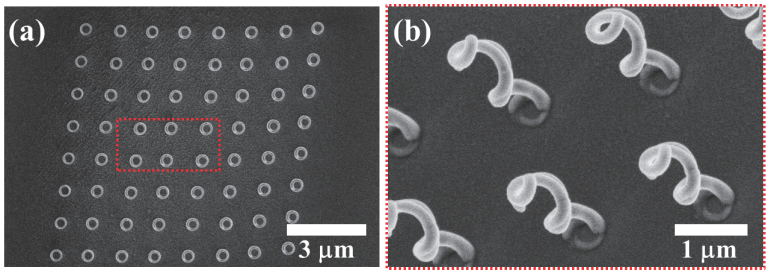

Figure 6.11: (a) SEM image of the W nanohelix array, viewed from top. (b) Magnified side-view SEM image of W nanohelices, marked with red dashed frame in (a).

To test the optical response of this helix/ITO sample, we built a setup sketched in Figure 6.12. The light source was generated by a supercontinuum laser and collimated by two coupled lenses.

Additionally, an adjustable diaphragm was used to control the beam profile of the input light. After that, a linear polariser and a quarter-wave plate were placed with the angle between their optical axes set as +45 and -45 °C to realise the RHCP and LHCP conditions, respectively. The circularly polarised beam probed the sample at normal incidence and the transmitted beam was divided by a beam splitter into two arms: the imaging system formed by a lens and a electron multiplied charge coupled device (EMCCD); the spectrum analysis system consisted of a lens and a spectrometer.

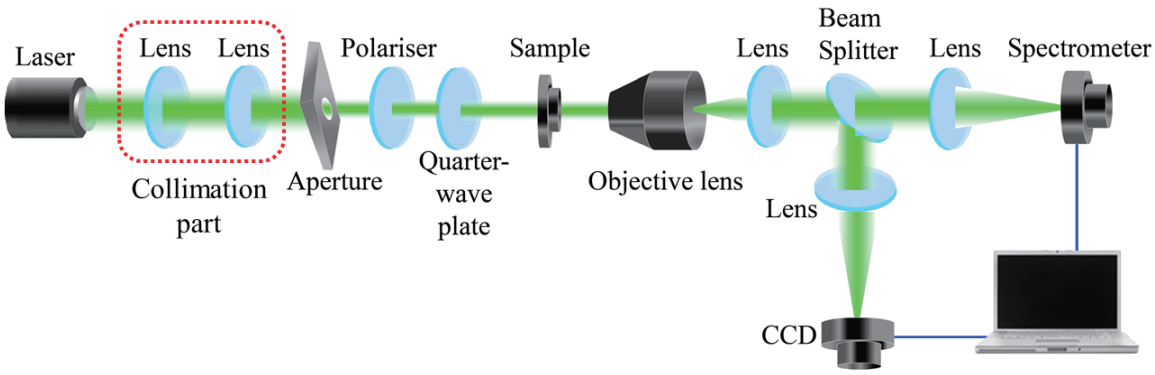

Figure 6.12: Diagram of the apparatus used for determine the transmission of the helix/ITO sample in different circular polarised condition.

By probing the helix/ITO sample with RHCP and LHCP lights, we obtained the transmitted signals at the helix/ITO region (T(helix)) and the blank ITO region (T(substrate)). We defined the transmission of the W helix pattern as T(helix)/T(substrate). Figure 6.13 showed that the LHCP light exhibited higher transmission with an average value of 2.5% than the RHCP light, for the right-hand rotated helix array. The transmission difference between the two circular polarised light was not as high as the results reported by refs[226, 227], which was due to the small pitch number we used here, i.e. the helix rotated only 2 loops. The 2-loop helix was not able to confine all the energy of the circularly polarised light with the same rotation direction.

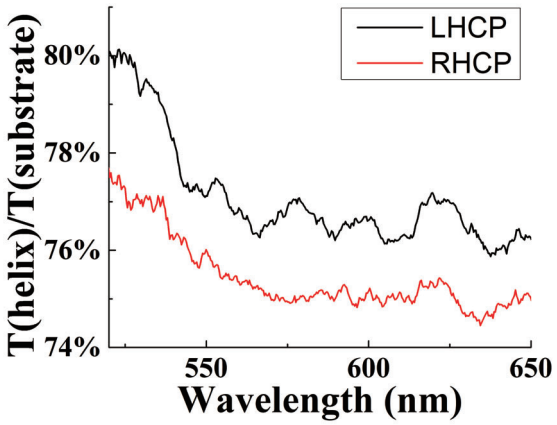

Figure 6.13: The transmission of the W helix pattern probed by RHCP and LHCP lights, respectively.

To investigate the optical behaviour of the nanohelix array on the ITO substrate at the ENZ range, we still need to design and fabricate multi-loop helix array with working wavelength at NIR.

6.3.3 Enhancement of WGM

Another application of the ITO was designed to be combined with the microsphere to enhance the whispering gallery mode (WGM) for the application of lasing[228] and sensing[229].

We designed a structure formed by ITO coated SiO_2 microsphere and Pt antenna to realise the high-quality-factor resonator. Figure 6.14 illustrated the diagram of light coupled into the antenna/ITO/microsphere structure using a prism platform. The Pt antenna was used to increase the coupling efficiency of light from prism to the microsphere. Between the antenna and microsphere, we planned to deposit a thin ITO layer to increase the quality factor of the microsphere cavity due to the low refractive index of ITO, and also modify the wavefront of the coupled light benefiting from the ENZ effect of ITO. This was an initial design, and further numerical and experimental investigations would be needed.

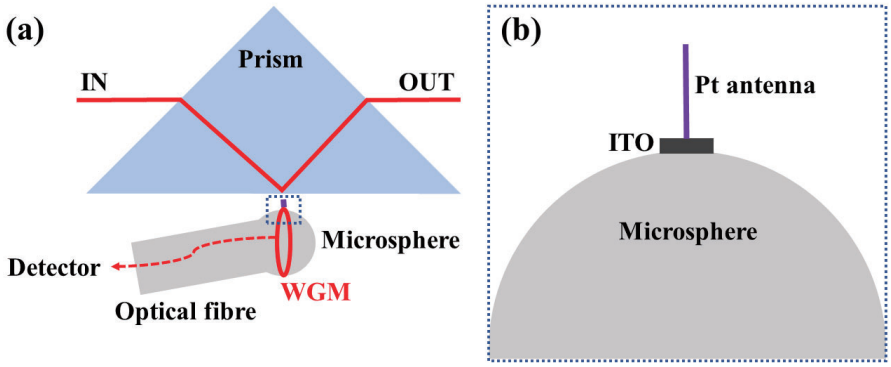

Figure 6.14: Diagram of the light coupled into a microsphere structure with the help of prism platform (a) and the magnified sketch of the antenna/ito/microsphere structure (b). The coupled signal of the microsphere can be collected by a detector via an optical fibre.

Figure 6.15 presented the fabrication process of the microsphere. The SiO_2 microsphere was fabricated using an optical fibre melted by a CO_2 laser with an output power of 3 W. Before the laser probing, the optical fibre with a diameter of 125 µm was cleaved and cleaned with acetone and IPA ultrasonic bathing. Then, the high-power beams were focused onto the end of optical fibre and melted the sharp end into a microsphere.

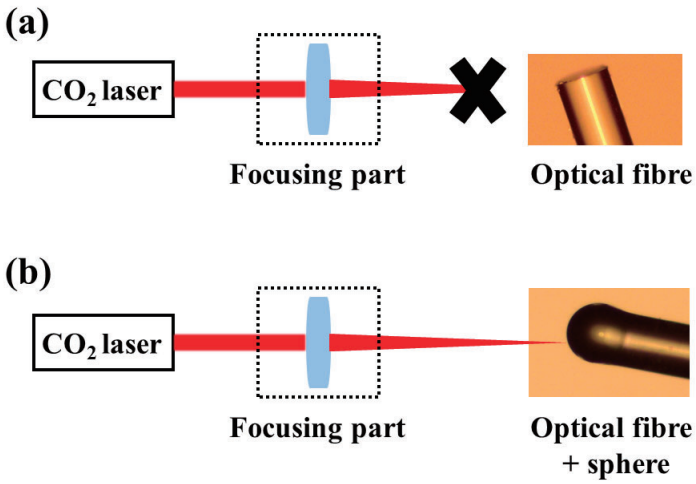

Figure 6.15: Diagram of an optical fibre before (a) and after (b) the probing of the CO_2 laser.

Then, the microsphere was coated with an ITO layer with a thickness of 100 nm, fabricated using the RF sputtering with deposition temperature of 300 °, Ar gas flow of 20 sccm and other parameters same as the ones described in Section 6.1. The Pt antenna was fabricated using EBID method. Figure 6.16 (a) showed the ITO coated microsphere and optical fibre. The ITO was deposited from the top

side, and thus the back bottom side of the sphere remained uncoated. The Pt antenna located on the microsphere where the region marked with red dashed frame in Figure 6.16 (a) and shown in 6.16 (b) clearly.

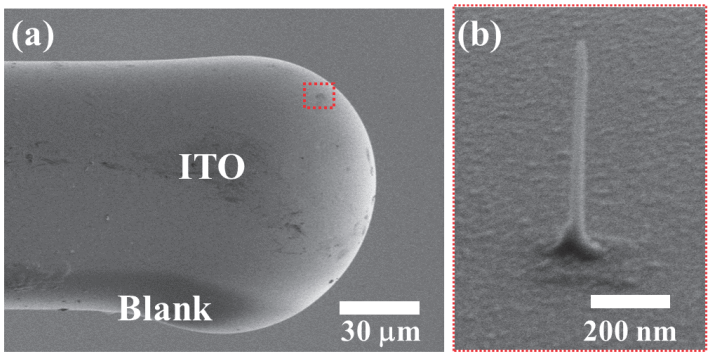

Figure 6.16: SEM images of the ITO coated SiO_2 microsphere and optical fibre (a), and the Pt antenna (b) fabricated on top the microsphere using EBID approach.

This project was just started before the submission of this thesis and needed more investigation about the prism coupling process.

6.4 Photonic trimming of QDs emission using EBID approach

In this section, we demonstrated an approach to conditioning the emission of QDs located in different hosts, via decorating the QDs with plasmonic nanopatterns fabricated using EBID method.

6.4.1 Motivation

The QDs are very sensitive to their photonic environment and their emission behaviours, e.g. lifetime[230] and quantum efficiency[231], can be manipulated via introducing specific nanofeatures[232, 233]. By introducing plasmonic cavities, the single photon emitting can be achieved[234]. The key requirements are the high quality factor and the low modal spatial volume, and these characteristics also benefit the emission threshold minimising and the efficiency increases. Additionally, shortening lifetime will also contribute to the increase of emission efficiency and modulation speed.

There are several platforms occur to engineer the QD emission. One candidate is dielectric resonators[107, 235] that have high quality factor but large modal volumes and long photon lifetimes. This kind coupling structure includes photonic crystal cavities, micropillars and microdisks[236, 237]. The other approach is based on plasmonic nanoresonators[110, 238], which have dramatically smaller modal volumes and photon lifetimes, but at the cost of high absorption losses and low quality

factors. According to the choice of platform, the most promising method to realise the efficient single photon emission is by choosing and designing a suitable photonic environment. During this process, the main limitation, the stringent positioning of QDs, needs to be overcome. For this purpose, there have been several solutions, such as locating and decorating QDs using AFM[239, 240] or photolithographic techniques[241, 242], the realisation of polymeric waveguides around QDs which dispersed in bulk polymers[243, 244], and positioning and post fabricating nanoparticles in proximity to randomly located QDs using hot-tip lithographic patterning and other approaches[245–247].

In this work, we propose another platform to engineering the QD emission based on a new technique, EBID. The EBID approach is able to directly fabricate nanopatterns on top of NWs with the flexibility of design of the plasmonic platform and the relaxation of the alignment requirements. Typically, we design and deposit a sub-wavelength Pt grating on a core-shell GaAs/AlGaAs NW that contains GaAs QDs using EBID method to trim the emission of QDs.

According to the optical plasmon effect in the NW, the emission of QDs is compressed is specific directions as the NW plays as a role of nanoresonator here[248, 249]. In order to manipulate the polarisation of the emission light, we design this sub-wavelength Pt grating because of its directional coupling effect. Typically, the grating structure is able to outcouple the light along its stacking direction and this will be demonstrated in this section. By design the location and orientation of the grating structure, we could tune the polarisation distribution of the emission of QDs.

Using this method, we succeed in the modification of the polarisation state of QD emission and the enhancement of the emission efficiency with an associated reduction in radiative lifetime of QDs. Additionally, we fabricate several Pt nanopatterns on top of GaAs pyramids embedding indium gallium arsenide (InGaAs) QDs and enhance the emission of the QDs.

6.4.2 QDs embedded in NWs

6.4.2.1 Fabrication

The GaAs QDs and core-shell GaAs/AlGaAs NWs were first fabricated using MBE process on GaAs substrate using the same approach described in Chapter 3. Then, the NWs contained QDs were detached and transferred onto a marked SiO_2/Au/Si substrate via direct contact method (Figure 6.17). The SiO_2/Au marks on the Si substrate were fabricated using standard EBL procedure, which formed by first coating the Si substrate with Au and SiO_2 layers and then the back etching of the SiO_2 layer to show the number Au marks. This step helps the deterministic location and measurement of individual NWs.

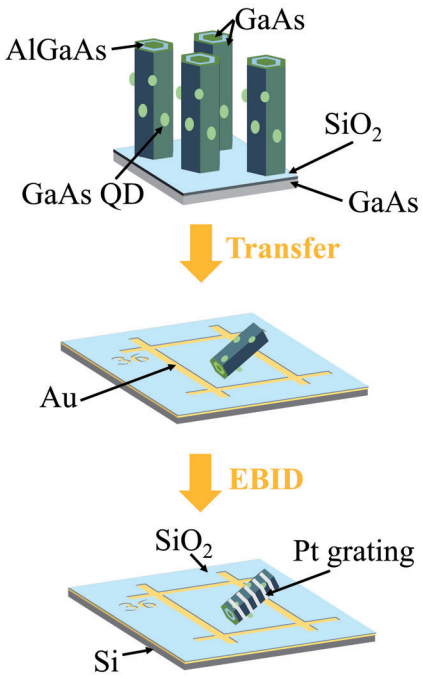

Figure 6.17: Transfer process of core-shell GaAs/AlGaAs NWs embedding GaAs QDs from GaAs substrate to marked SiO_2/Au/Si substrate and the following EBID process.

The final step of fabrication was the decoration of the selected NW with a sub-wavelength Pt grating using EBID technique. To deposit Pt, a suitable precursor was used here, based on the compound methylcyclopentadienyl trimethyl platinum ($MeCpPtMe_3$). The deposited material consists mostly of Pt atoms in a carbon matrix, with dilution percentage that varies from 10% to up to 100% Pt, depending on the specific deposition parameters and post-fabrication procedures[250].

During the EBID process, we used a deposition current of 150 pA, an acceleration voltage of 3 kV, and a dose of 1 C/cm^2, at room temperature, and these parameters produced an expected Pt percentage of 30%[251]. Although the choice of the Pt depended on the precursor availability, this is a simple limitation of our instrument but not of the approach. To extend the choice of depositing materials, suitable precursors and systems are needed, for instance, the deposition of Au can be realised in IBID systems[252].

Figures 6.18 shows SEM images of the NW before (bare) and after (dressed) the deposition of the Pt grating, respectively. The grating was made of Pt wires with the width of 50 nm and thickness of 100 nm, and have a period of 250 nm. We designed the grating based on the parameters to coupling the optical mode in the NW with a guided mode and an effective index of 3.6[108, 253]. As visible in Figure 6.18 (b), every Pt NWs were all perfectly aligned with the designed parameters and only

covering the top surface of the GaAs/AlGaAs NW. The SEM images give the clear viewing of the GaAs/AlGaAs NW that suspends over a SiO_2 trench which is the part of the mark on the substrate. According to the refractive index difference between the NW and the substrate (and/or air), we exclude that this configuration will not show significant effect on the emission of QDs.

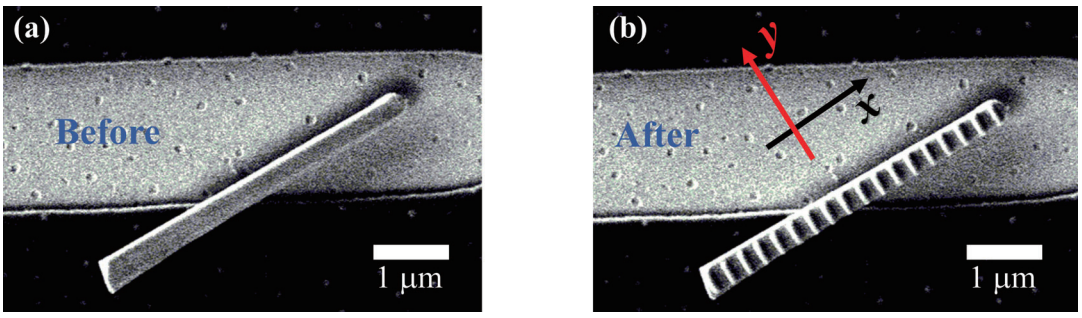

Figure 6.18: The SEM image of the NW on the marked SiO_2/Au/Si substrate before (a) and after (b) the deposition of sub-wavelength Pt grating.

Furthermore, in the measurement part, we compared the signal of the QD emission directly on the bare and dressed NW, without any position changing of the NW based on the alignment marks. This is made to remove any potential minor contribution from the uneven substrate.

6.4.2.2 Results

We used a micro-photoluminescence (MPL) system (Figure 6.19)[254, 255] to measure and analyse the emission of QDs embedded in the NW before and after the Pt grating definition.

The sample was loaded in the cryostat which was the identical one shown in Figure 3.25. The optical measurement setup was divided into three parts. First, the upper arm in Figure 6.19 with EMCCD is able to image the sample. With the help of the motorised stage, halogen source and EMCCD, the selected NW can be illuminated and easily positioned. Second, the sample was pumped with a focused CW laser beam with a wavelength of 405 nm. The emission of QDs were collected using an objective and routed with two beam splitters (BSs) toward a spectrometer for analysis. Prior to the spectrometer, a long-pass filter (LPF) was inserted to removing the pump and illumination signals. Additionally, a linear polariser mounted on a rotating stage could be set prior to the LPF to identify the polarisation state of the QD emission. The third path was formed with a 800 fs pulsed laser (80 MHz) for exciting QDs and a time-resolved photoluminescence (TRPL) system[120] for determining the radiative lifetime of QDs.

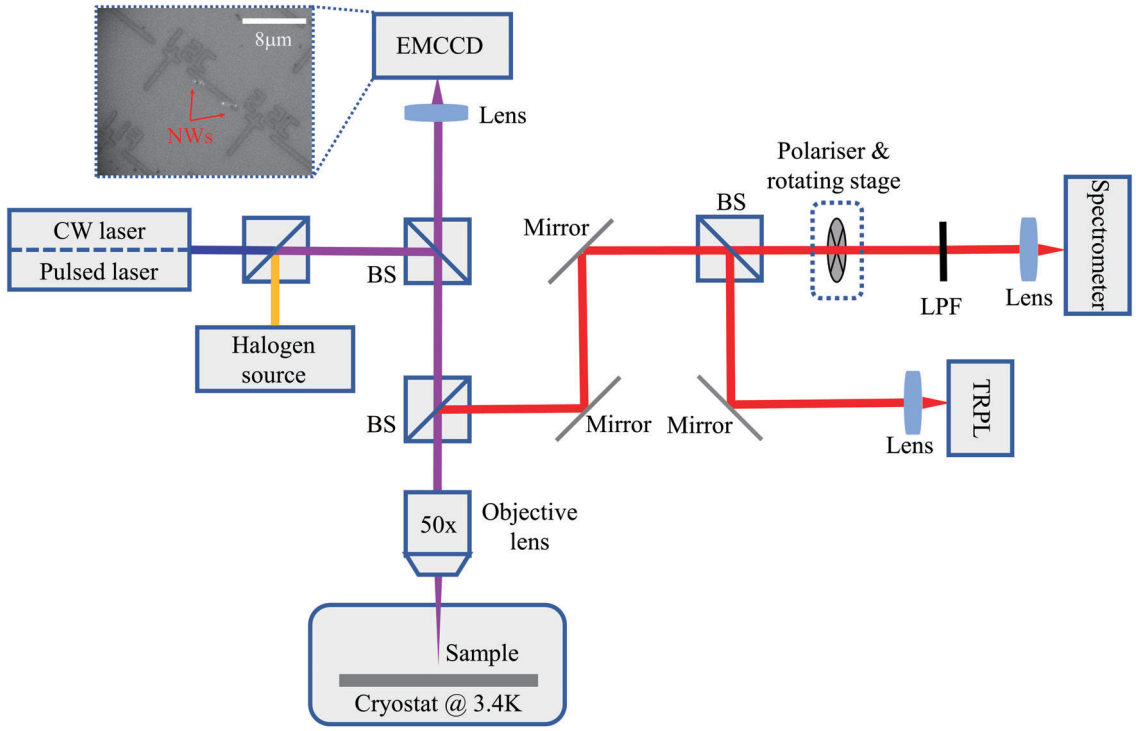

Figure 6.19: The detailed diagram of the measurement optical path of the QD emission. The system is consisted of pump sources(CW laser or pulsed source), illumination source (halogen source), light-matter interaction platform (cryostat), sample position locating path (EMCCD), PL spectrum analysing path (spectrometer), photon lifetime detecting path (TRPL), and other optical elements. The photograph of NWs located on the marked substrate are also attached here. The shiny spots on NWs come from the emission of QDs when pumped with CW laser.[256]

Figure 6.20 (a) and (b) show the emission spectra of QDs pumped with sample power before and after the deposition of Pt grating, respectively. These two spectra were measured without the linear polariser and showed that the emission wavelength of the (single) QD was about 674 nm and did not shift after the introducing of the sub-wavelength metallic pattern. However, the Pt grating showed an effect that reducing the emission intensity greatly, by about 75%. This could be resulted from the high absorption losses introduced by the metallic structures.

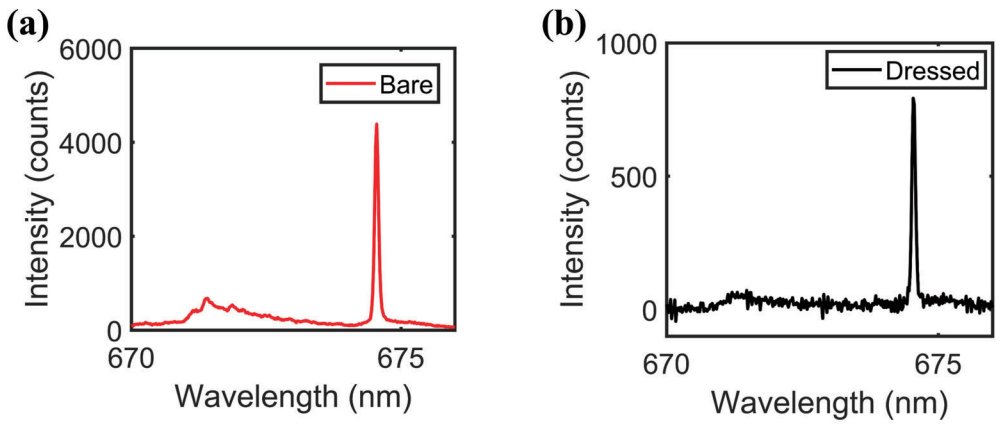

Figure 6.20: Spectra of QD emission collected from the bare (a) and dressed (b) NWs without the polariser before spectrometer.

To determine the effect of the Pt grating to the radiative property of QDs, the pumped source was switched into the pulsed laser with similar pumped power for both bare and dressed samples, shown in Figure 6.21. The QDs before and after the deposition of Pt nanofeature exhibit a similar trend for the curve of emission intensity as a function of pump power. Typically, the gradient of the two curves is almost the same when the pumped power of the laser is around 20 µW.

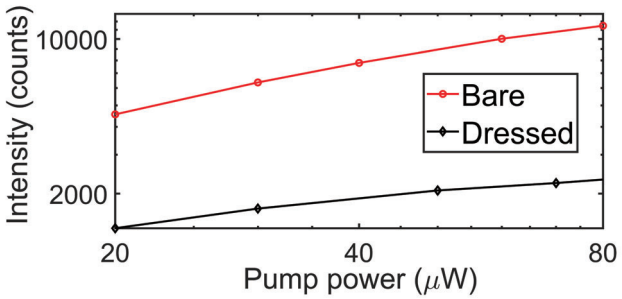

Figure 6.21: The emission intensity of QDs as a function of pump power for both bare and dressed NWs.

By pumping the bare and dressed NWs with the pulsed laser with same power (20 µW), we obtained the photon lifetime of QDs (Figure 6.22) using the TRPL approach. The comparison between Figure 6.22 (a) and (b) indicates that the dressed NW exhibits a 17% reduction in lifetime compared to the bare NW.

From the measurement of emission intensity and lifetime alone, we cannot directly find the reason for the reduction in the lifetime, because we are not sure whether the decreasing results from

a radiative or non-radiative contribution[231, 257], since the metallic grating with high optical losses is able to absorb the emission but also increase the overall efficiency.

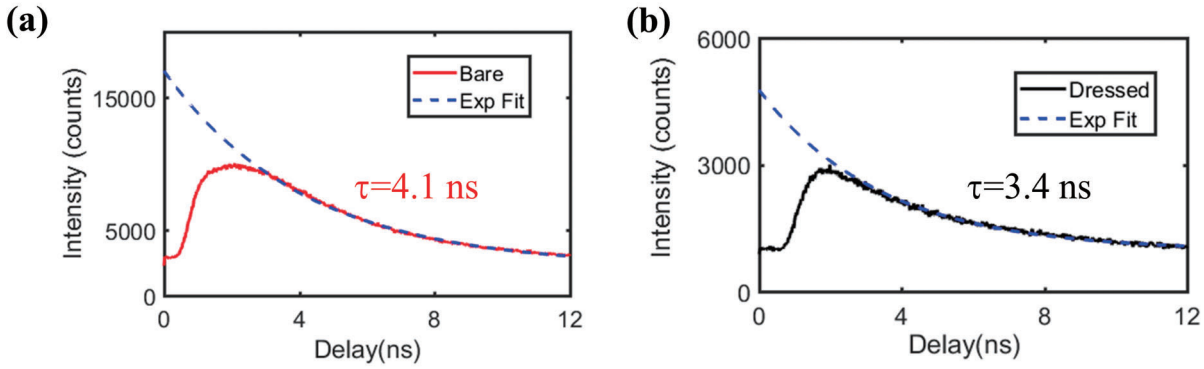

Figure 6.22: The measured radiative lifetime (τ) of QDs before (a) and after (b) the depositing of Pt grating.

To investigate the detailed mechanics of the light-matter interaction between the QD emission and the Pt grating, typically the coupling dynamics, we mounted a linear polariser (Figure 6.19) prior the spectrometer and pumped the bare and dressed NWs with the CW laser (same power). Figure 6.23 (a) and (b) show the emission intensity vs. the polarisation direction before and after the definition of the Pt grating, respectively. Due to the presence of the plasmonic nanopattern, the polarisation shape of the QD emission changed drastically, almost in 90 $^{\circ}$. The dressed NW mostly emits with polarisation along its long axis (x direction in Figure 6.18 (b)), while the bare NW emits photons mostly polarised perpendicular to the long axis (y direction in Figure 6.18 (b)).

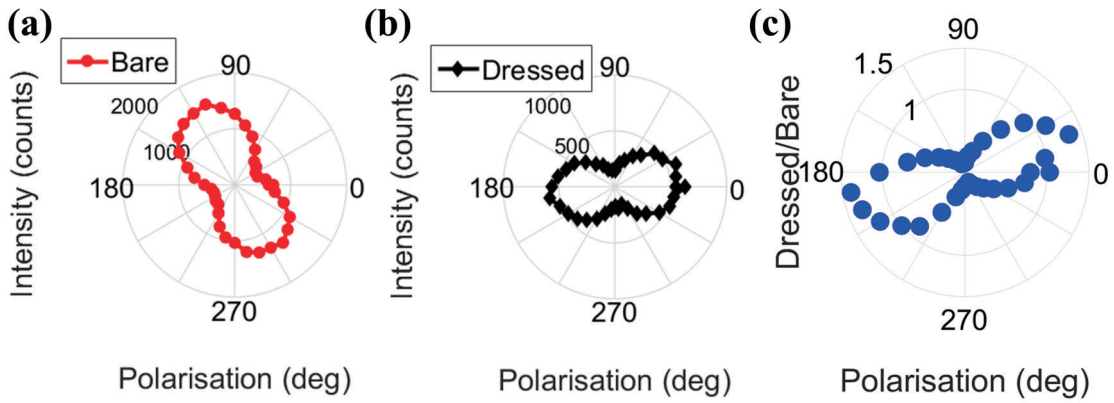

Figure 6.23: Measured results of the polarisation state of QDs emission before (a) and after (b) decorating NWs. (c) The intensity ratio (between dressed and bare NW) vs. the polarisation direction to show the emission enhancement at specific polarised direction.

The quantitative comparison of the polarisation state between the bare and dressed NWs are plotted in Figure 6.23 (c) via displaying the ratio of the emission intensity between them. The comparison shows a maximum enhancement of the collected emission in the order of 45%, along the x direction.

6.4.2.3 Discussion

The QD grown on the facet of NW can be considered as the dipole that oscillate along y direction[108, 258]. The emission of this dipole is coupled to one of the photonic modes of the NW with a high refractive index. By introducing the Pt grating with specific spatial parameters, we are able to suppress the component oscillating perpendicular to the long axis of the NW (y direction), but meanwhile improve the out-coupling of the component along the x direction, with an associated reduction in the photon lifetime.

The coupling mechanics between the emission and Pt grating can be generally analysed based on a couple of assumptions, i.e. a simplified model of the NW[108] and the direct comparison of the emission properties between bare and dressed NWs.

The recent researches into the QD/NW model show that the emission efficiency has strong dependency to the specific position of the QD in the NW and also the orientation of the NW on the substrate[108]. This approach of constructing nanofeartures at the position of QDs directly promises a further dramatic enhancement of the emission, with the ability to tailoring the polarisation state.

The NW embedding QDs with peculiar lasing mode shows excellent potential in the field

of near-field imaging, for example, conjugating with AFM systems[240] or cathodoluminescence techniques[108], and also in the detecting of emission efficiency. Besides, these approaches can be automated and integrated into the workflow process, to scale up the technique[259]. Additionally, in specific procedures, the alignment markers in the substrate will benefit the locating of NWs which and thus make it easier to determine the most suitable plasmonic structures within a library of available geometries, after the topological or photonic characterisation. Both the alignment accuracy and the deposition time are typical of nanolithographic processes; therefore, it is expected that the throughput will be comparable with standard fabrication methods.

6.4.3 QDs embedded in pyramid structure

Here, we used another kind of QDs embedded in a pyramid structure[260, 261], sketched in Figure 6.24. Our collaborators prepared the pyramid samples. The multilayer pyramid structure were deposited using MBE approach and transferred onto GaAs substrate. The bonding process between the pyramid and substrate were realised using two approaches, i.e. the Au-AuSn-Au reflow approach and SU-8 spin-coating approach.

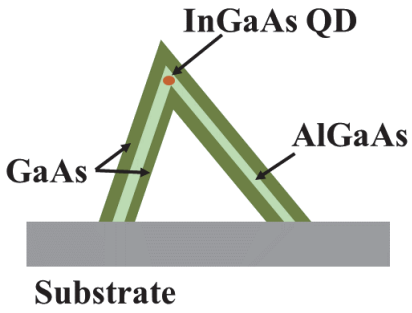

Figure 6.24: Diagram of an InGaAs QD embedded in a GaAs/AlGaAs/GaAs multilayer pyramid structure.

First, the pyramids were bonded onto the GaAs substrate using Au-AuSn-Au reflow approach. We decorated the pyramid with different Pt nanopatterns, such as nanoantenna, nanohelix and nanogratings, using EBID technique. The SEM images of these patterns were shown in Figure 6.25.

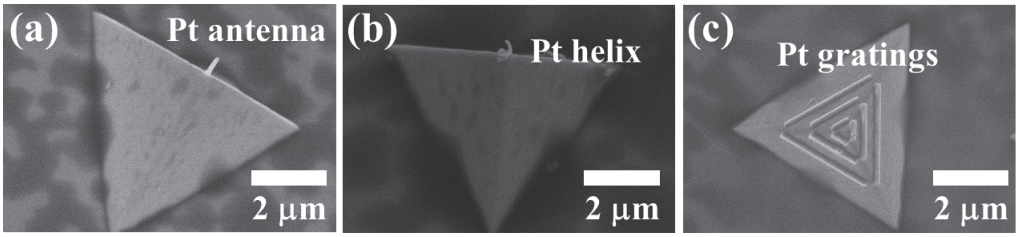

Figure 6.25: SEM images of Pt nanoantenna (a), Pt nanohelix (b) and Pt nanogratings deposited on the pyramid structure using EBID approach.

We pumped these samples before and after the definition of Pt nanopatterns, found that the bleaching effect occurred in their emission. This problem may due to the damage of the QDs or their environment during the fabrication process. Hence, we used another approach to bonding the pyramid and substrate via SU-8 spin coating. Figure 6.26 (a) sketched the bonding diagram. The SU-8 coated most of the pyramid except for the top end, which could be seen in the SEM image shown in Figure 6.26 (b). By introducing the SU-8 layer, we prevented the bleaching issue.

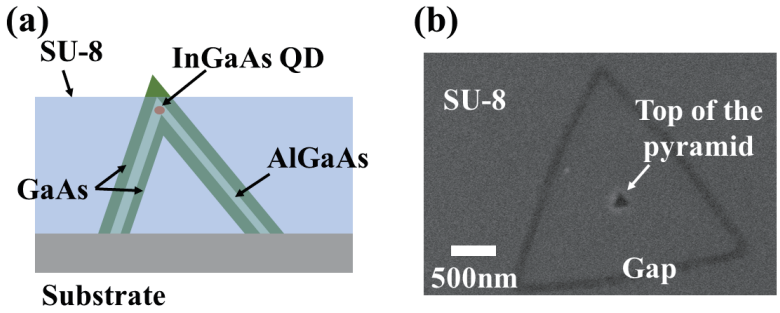

Figure 6.26: (a) Diagram of the pyramid structure bonded onto the GaAs substrate using SU-8 spin coating approach. (b) SEM image of the SU-8 bonded pyramid, viewed from top.

Using EBID approach, we designed and fabricated various nanopatterns with different materials and sizes, to decorating the pyramid and manipulating the emission of the QDs inside. Figure 6.27 presented these patterns, such as Pt and SiO_2 nanoantennas and SiO_2 nanodooms.

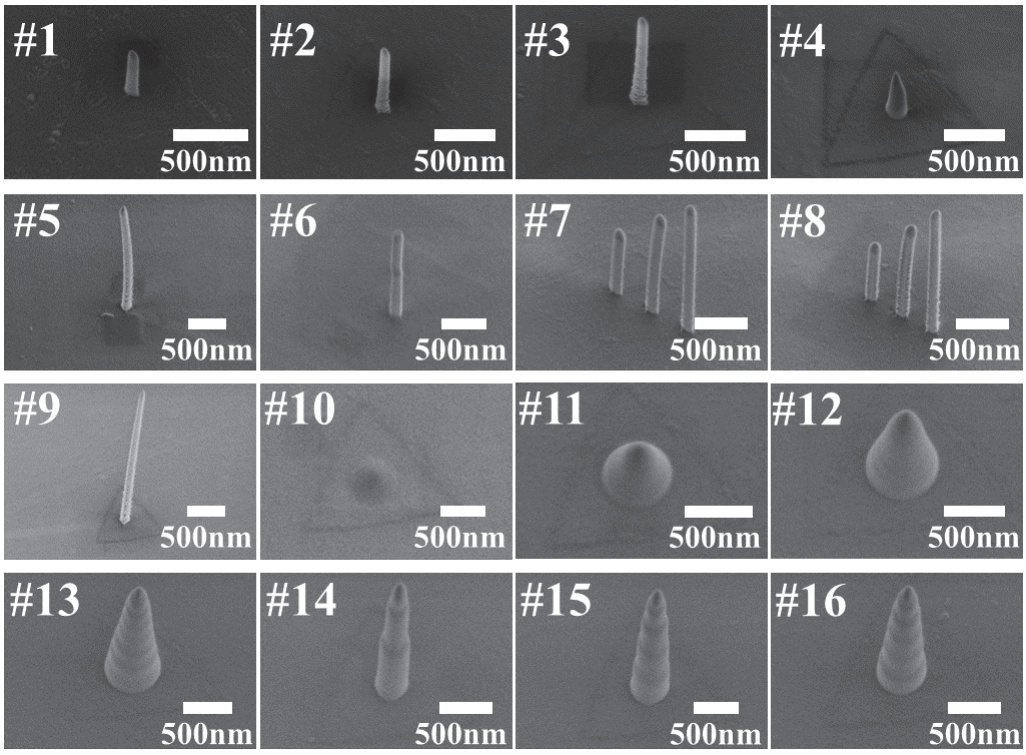

Figure 6.27: SEM images of various nanopatterns deposited on the SU-8 coated pyramids: (#1)-(#3) Pt nanoantennas; (#4)-(#9) SiO_2 nanoantennas; (#10)-(#16) SiO_2 nanodooms.

The emission of these samples was obtained and shown in Figure 6.28. The introducing of nanopatterns indeed enhanced the emission of QDs embedded in the pyramid structures. Additionally, the SiO_2 patterns showed a more significant enhancement of the emission of QDs. To determine the relationship between the nanopattern and the QD emission, we needed to deposit more patterns on pyramid/QD structures with controlled parameters, and also measure the emission before and after the decoration.

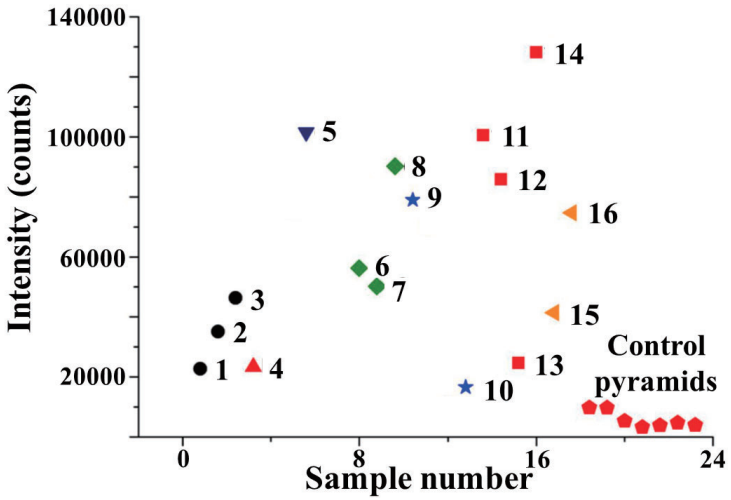

Figure 6.28: Emission of pyramid/QD samples decorated with different nanopatterns compared to the emission of control pyramids (no decoration).

6.5 Conclusion

We have demonstrated the fabrication of ITO thin films using RF magnetron sputtering approach under different gas atmospheres and deposition temperatures. As the O_2 gas concentration decreases, the Rs of ITO film drops down, i.e. the conductivity increases, and the ENZ effect starts to present at the wavelength range varied from 1200 to 1600 nm. Along with the deposition temperature increasing, the conductivity of ITO film increase as well and the zero-permittivity wavelength tends to short range. By combining ITO with nanohelix array and microsphere, we propose the approaches to enhance or manipulate the optical response of circularly polarised light or the WGM.

With the help of EBID technique, we directly fabricated nanopatterns to decorate the QDs embedded in different hosts and manipulated the emission properties of QDs. Typically, we deposited a sub-wavelength Pt grating on top of a core-shell GaAs/AlGaAs NW hosting GaAs QDs and realised the photonic trimming of the emission property of QDs. The presence of Pt grating enhance the collection efficiency of the QD emission by 45% at the polarisation along the long axis of the NW, with an overall reduction in the photon lifetime of 17%. In addition, the SiO_2 nanoantenna and nanodooms also exhibited dramatic enhancement of the emission of InGaAs QDs embedded in GaAs/AlGaAs/GaAs multilayer pyramid structure.

The EBID fabrication approach, based on the post-fabrication and alignment-free advantages, is able to deposit various nanopatterns on different substrates to photonic engineering of quantum emitters and manipulating optical responses. We believe that these approaches will open the door to

realising new efficient quantum sources even at the single photon level and create new platforms of quantum sources at further applications.

Chapter 7

Conclusion

7.1 Thesis summary

This thesis has shown two methods to design and fabricate ENZ MMs. One is using the multilayer structure formed by sub-wavelength unit layers with positive (dielectric) and negative (metal or graphene) permittivities. This structure has the effective permittivity with a vanishing real part at desired frequency ranges and has been combined with flexibility using a sacrificial-layer assisted transfer method. The other approach is to operate ITO close to its plasma frequency. The permittivity of ITO is determined by the fabrication parameters and can be manipulated into zero in the NIR regime. Using these ENZ platforms, we can obtain peculiar optical response, such as the emission enhancement. Furthermore, by depositing specific nanofeatures on ENZ substrate using EBID technique, we propose different designs to realise typical optical behaviour.

The motivation of this work was introduced in chapter 1 and 2, which was corresponded to the exotic photonic properties of ENZ MMs. The artificial materials with vanishing permittivity supported unique optical behaviours, for example, the diverging wavelength and constant phase occurring at the light-matter interaction. Different approaches had been developed to achieve the ENZ response, including tuning the modal dispersion in narrow plasmonic channels, exploiting the natural dispersion of TCOs and creating a composite structure with metals and dielectrics. Additionally, ENZ media also exhibited enormous potentials in the photonic and plasmonic regimes, such as asymmetry transmission, non-diffraction imaging, enhanced directive emission and enhanced non-resonant optical nonlinearity.

To realise the ENZ structure, a typical fabrication and characterisation protocol of the metal/dielectric multilayer model were demonstrated in Chapter 3. The e-beam evaporation approach was utilised to deposit Ag and SiO_2 nanolayers. In order to optically characterise the component materials

and multilayer structures, we developed a retrieval method which was able to obtain the effective permittivity of a target film using measured transmission, reflection and total thickness. This chapter also showed that the characterised multilayer ENZ media could enhance the emission of QDs.

The fabrication of the sub-wavelength multilayer structure usually required nanofabrication techniques developed for flat and rigid substrates, which were not always applicable to arbitrary-shaped optoelectronic devices. To break these limitations, we design and experimentally demonstrate an optical free-standing and low-loss ENZ membrane in Chapter 4, by stacking polymer (SU-8) and Ag nano-layers periodically. The flexible ENZ MM exhibited almost unchanged optical properties after repeated macroscopic and sustained mechanical deformations (up to 10000 cycles), and also fitted surfaces with a radius of curvature of the order of few microns. Additionally, in Chapter 5, we proposed a method to introduce both flexibility and electrical tunability into ENZ media by replacing the metal layer with graphene in the multilayer model. The multilayer graphene/PMMA membrane was fabricated, but due to its weak strength and uniformity, we could not obtain the ENZ responses from this structure. Then, in order to electrically tuning the permittivity of graphene-based ENZ media, Chapter 5 also presented the initial test of the optical response of graphene/ZnSe structure with the different voltage applied. This result offered the possibility of tuning the graphene-based ENZ media via modifying gate voltages.

Finally, the other ENZ platform, ITO, was fabricated and optically characterised in Chapter 6. By controlling the gas ratio and deposition temperature in the RF magnetron sputtering process, we managed to manipulate the ENZ region of ITO thin films at NIR range. The ENZ ITO was designed to be combined with different photonic features, including nanoantenna and nanohelix, to realise enhanced optical coupling and chirality. The nanopatterns were fabricated directly utilising a new approach, EBID. Using this technique, we fabricated various metallic and dielectric nanofeatures on different substrates, typically randomly distributed NWs and nanopyramids, to realising the photonic trimming of quantum emitters.

7.2 Outlook

The primary goal of this thesis, i.e. the design, fabrication and typical applications of ENZ MMs, has been achieved. The fabrication and characterisation approaches offer us great potentials to manipulate the optical properties of ENZ media, while there are various research areas need to be investigated and accomplished. The following part of this section will outline the most promising applications in further research procedures.

7.2.1 Superlensing

In Chapter 1, we discussed that the ENZ media could realising the superlensing, i.e. the non-diffraction imaging. This application is based on the lack of spatial dispersion while light travelled through the ENZ medium.

To realise this, we have first obtained the free-standing ENZ membrane, which is demonstrated in Chapter 4. The flexible ENZ membrane can be curved and conformed onto different substrates and irregular objects. The next step is coating this flexible ENZ membrane onto emitters or light sources. The curved ENZ structure is able to separate the emission of two light sources located with a distance smaller than the diffraction limit. Then, in the farfield, the two sources can be recognised, and thus the non-diffraction imaging is achieved. Using this approach, we are possible to realise the superlensing in practice.

7.2.2 Graphene based ENZ MMs with electrical tunability

Our initial result shows that the transmission of graphene/ZnSe bilayer structure is manipulated by applying different voltages. This also promises that the effective permittivity of the graphene/dielectric structure can be electronically tuned.

In the following, we need to realise the multilayer graphene/dielectric structure by stacking the bilayer structure periodically to achieve effective zero permittivity based on EMT. Additionally, by applying voltage to the whole structure, we can realise the tuning of the effective permittivity. This is a new way to realise low-loss ENZ media. Due to the high flexibility of graphene and also the electrical tunability of the multilayer structure, we can manipulate the optical response of this structure in both mechanical and electronic ways.

Furthermore, the phase of the unit layer in the multilayer structure can be modified by applying different voltages in each graphene layer. This approach is able to realise the 3D imaging.

7.2.3 Enhanced optical coupling using antenna/ITO structure

We have shown the initial design of the WGM that can be launched by coupling light from a prism to the microsphere, made form the melting optical fibre. To realise this, we first deposit Pt nanoantennas onto the ITO coated microsphere using EBID approach. We aimed to increasing both the coupling efficiency and quality factor by using this structure. Further measurements are need to be launched to test this design.

If this model worked, we would be able to enhance the coupling efficiency using ENZ platform and find a alternative technique for scanning near-field optical microscopy (SNOM).

7.2.4 Enhanced emission of QDs using directive fabricated SiO_2 nanoantenna

The enhancement of the emission of QDs using nanoscale dielectric lens or antenna is important for the applications of quantum emitters. Benefiting from the direct fabrication method, EBID, we have realised the design and deposition of various SiO_2 nanoantennas on QDs hosted by micro-pyramids. The initial results qualitativelyshow that the SiO_2 nanoantennas do have the capability to enhance and trim the emission of QDs, which is encouraging for the following tests.

The further investigation of the QDs emission before and after the antenna coating need to be processed. We believe that the size of the SiO_2 antennas will be the key parameters to control the enhancement of the QDs emission.

Bibliography

[1]W. Cai and V. Shalaev, *Optical metamaterials: fundamentals and applications* (Springer Science & Business Media, 2009).

[2]J. B. Pendry, D. Schurig and D. R. Smith, 'Controlling electromagnetic fields', science **312**, 1780–1782 (2006).

[3]A. Sihvola, 'Electromagnetic emergence in metamaterials', in *Advances in electromagnetics of complex media and metamaterials* (Springer, 2002), pp. 3–17.

[4]S. Zouhdi, A. Sihvola and A. P. Vinogradov, *Metamaterials and plasmonics: fundamentals, modelling, applications* (Springer Science & Business Media, 2008).

[5]I. Freestone, N. Meeks, M. Sax and C. Higgitt, 'The lycurgus cup-a roman nanotechnology', Gold bulletin **40**, 270–277 (2007).

[6]U. Leonhardt, 'Optical metamaterials: invisibility cup', Nature photonics **1**, 207 (2007).

[7]S. A. Maier and H. A. Atwater, 'Plasmonics: localization and guiding of electromagnetic energy in metal/dielectric structures', Journal of applied physics **98**, 10 (2005).

[8]H. A. Atwater, 'The promise of plasmonics', Scientific American **296**, 56–62 (2007).

[9]L. I. Mandelstam, *Lectures on some problems of the theory of oscillations (1944), in complete collection of works* (Moscow: Academy of Sciences, 1950).

[10]V. G. Veselago, 'The electrodynamics of substances with simultaneously negative values of and μ', Soviet physics uspekhi **10**, 509 (1968).

[11]J. B. Pendry, A. Holden, W. Stewart and I Youngs, 'Extremely low frequency plasmons in metallic mesostructures', Physical review letters **76**, 4773 (1996).

[12]J. B. Pendry, A. J. Holden, D. J. Robbins and W. Stewart, 'Magnetism from conductors and enhanced nonlinear phenomena', IEEE transactions on microwave theory and techniques **47**, 2075–2084 (1999).

[13]D. R. Smith, W. J. Padilla, D. Vier, S. C. Nemat-Nasser and S. Schultz, 'Composite medium with simultaneously negative permeability and permittivity', Physical review letters **84**, 4184 (2000).

[14]R. A. Shelby, D. R. Smith and S. Schultz, 'Experimental verification of a negative index of refraction', science **292**, 77–79 (2001).

[15]G. A. Niklasson, C. Granqvist and O Hunderi, 'Effective medium models for the optical properties of inhomogeneous materials', Applied Optics **20**, 26–30 (1981).

[16]C. Wenshan and V. Shalaev, 'Optical metamaterials. fundamentals and applications', Springer. pp. xi **3**, 9 (2010).

[17]P. Moitra, Y. Yang, Z. Anderson, I. I. Kravchenko, D. P. Briggs and J. Valentine, 'Realization of an all-dielectric zero-index optical metamaterial', Nature Photonics **7**, 791 (2013).

[18]A. Alù and N. Engheta, 'Achieving transparency with plasmonic and metamaterial coatings', Physical Review E **72**, 016623 (2005).

[19]N. I. Landy, S Sajuyigbe, J. J. Mock, D. R. Smith and W. J. Padilla, 'Perfect metamaterial absorber', Physical review letters **100**, 207402 (2008).

[20]N. I. Zheludev, 'The road ahead for metamaterials', Science **328**, 582–583 (2010).

[21]S. Enoch, G. Tayeb, P. Sabouroux, N. Guérin and P. Vincent, 'A metamaterial for directive emission', Physical Review Letters **89**, 213902 (2002).

[22]H.-X. Xu, G.-M. Wang and T. Cai, 'Miniaturization of 3-d anistropic zero-refractive-index metamaterials with application to directive emissions', IEEE Transactions on Antennas and Propagation **62**, 3141–3149 (2014).

[23]M. Silveirinha and N. Engheta, 'Design of matched zero-index metamaterials using nonmagnetic inclusions in epsilon-near-zero media', Physical Review B **75**, 075119 (2007).

[24]A. D. Neira, N. Olivier, M. E. Nasir, W. Dickson, G. A. Wurtz and A. V. Zayats, 'Eliminating material constraints for nonlinearity with plasmonic metamaterials', Nature communications **6**, 7757 (2015).

[25]R. Maas, J. Parsons, N. Engheta and A. Polman, 'Experimental realization of an epsilon-near-zero metamaterial at visible wavelengths', Nature Photonics **7**, nphoton–2013 (2013).

[26]G. V. Naik and A. Boltasseva, 'A comparative study of semiconductor-based plasmonic metamaterials', Metamaterials **5**, 1–7 (2011).

[27]M. Silveirinha and N. Engheta, 'Tunneling of electromagnetic energy through subwavelength channels and bends using ε-near-zero materials', Physical review letters **97**, 157403 (2006).

[28]R. Liu, Q. Cheng, T. Hand, J. J. Mock, T. J. Cui, S. A. Cummer and D. R. Smith, 'Experimental demonstration of electromagnetic tunneling through an epsilon-near-zero metamaterial at microwave frequencies', Physical review letters **100**, 023903 (2008).

[29]B. Edwards, A. Alù, M. E. Young, M. Silveirinha and N. Engheta, 'Experimental verification of epsilon-near-zero metamaterial coupling and energy squeezing using a microwave waveguide', Physical review letters **100**, 033903 (2008).

[30]J. Luo, P. Xu, H. Chen, B. Hou, L. Gao and Y. Lai, 'Realizing almost perfect bending waveguides with anisotropic epsilon-near-zero metamaterials', Applied Physics Letters **100**, 221903 (2012).

[31]J. Luo and Y. Lai, 'Anisotropic zero-index waveguide with arbitrary shapes', Scientific reports **4**, 5875 (2014).

[32]H. Feng Ma, J. Hui Shi, W. Xiang Jiang and T. Jun Cui, 'Experimental realization of bending waveguide using anisotropic zero-index materials', Applied Physics Letters **101**, 253513 (2012).

[33]J. Luo, W. Lu, Z. Hang, H. Chen, B. Hou, Y. Lai and C. T. Chan, 'Arbitrary control of electromagnetic flux in inhomogeneous anisotropic media with near-zero index', Physical review letters **112**, 073903 (2014).

[34]A. Salandrino and N. Engheta, 'Far-field subdiffraction optical microscopy using metamaterial crystals: theory and simulations', Physical Review B **74**, 075103 (2006).

[35]M. E. Nasir, W. Dickson, G. A. Wurtz, W. P. Wardley and A. V. Zayats, 'Hydrogen detected by the naked eye: optical hydrogen gas sensors based on core/shell plasmonic nanorod metamaterials', Advanced Materials **26**, 3532–3537 (2014).

[36]C. Rizza, A. Di Falco, M. Scalora and A. Ciattoni, 'One-dimensional chirality: strong optical activity in epsilon-near-zero metamaterials', Physical review letters **115**, 057401 (2015).

[37]R. W. Ziolkowski, 'Propagation in and scattering from a matched metamaterial having a zero index of refraction', Physical Review E **70**, 046608 (2004).

[38]A. Alu, M. G. Silveirinha, A. Salandrino and N. Engheta, 'Epsilon-near-zero metamaterials and electromagnetic sources: tailoring the radiation phase pattern', Physical review B **75**, 155410 (2007).

[39]I. Liberal and N. Engheta, 'Near-zero refractive index photonics', Nature Photonics **11**, 149 (2017).

[40]J. K. Gansel, M. Thiel, M. S. Rill, M. Decker, K. Bade, V. Saile, G. von Freymann, S. Linden and M. Wegener, 'Gold helix photonic metamaterial as broadband circular polarizer', Science **325**, 1513–1515 (2009).

[41]A. S. Karimullah, C. Jack, R. Tullius, V. M. Rotello, G. Cooke, N. Gadegaard, L. D. Barron and M. Kadodwala, 'Disposable plasmonics: plastic templated plasmonic metamaterials with tunable chirality', Advanced Materials **27**, 5610–5616 (2015).

[42]V. Fedotov, P. Mladyonov, S. Prosvirnin, A. Rogacheva, Y Chen and N. Zheludev, 'Asymmetric propagation of electromagnetic waves through a planar chiral structure', Physical review letters **97**, 167401 (2006).

[43]M Decker, M. Klein, M Wegener and S Linden, 'Circular dichroism of planar chiral magnetic metamaterials', Optics letters **32**, 856–858 (2007).

[44]Z. Wang, Y. Chong, J. D. Joannopoulos and M. Soljačić, 'Observation of unidirectional backscattering-immune topological electromagnetic states', Nature **461**, 772 (2009).

[45]M. Memarian and G. V. Eleftheriades, 'Dipole radiation near anisotropic low-permittivity media', Progress In Electromagnetics Research **142**, 437–462 (2013).

[46]A. Alù and N. Engheta, 'Boosting molecular fluorescence with a plasmonic nanolauncher', Physical review letters **103**, 043902 (2009).

[47]J. Kim, A. Dutta, G. V. Naik, A. J. Giles, F. J. Bezares, C. T. Ellis, J. G. Tischler, A. M. Mahmoud, H. Caglayan, O. J. Glembocki et al., 'Role of epsilon-near-zero substrates in the optical response of plasmonic antennas', Optica **3**, 339–346 (2016).

[48]Y. Ma, P Wang, X Chen and C. Ong, 'Near-field plane-wave-like beam emitting antenna fabricated by anisotropic metamaterial', Applied Physics Letters **94**, 044107 (2009).

[49]R. Terhune, P. Maker and C. Savage, 'Optical harmonic generation in calcite', Physical Review Letters **8**, 404 (1962).

[50]R. G. Brewer and E. Hahn, 'Coherent two-photon processes: transient and steady-state cases', Physical review A **11**, 1641 (1975).

[51]P. Kelley, 'Self-focusing of optical beams', Physical Review Letters **15**, 1005 (1965).

[52]J. Eilbeck and R. Bullough, 'The method of characteristics in the theory of resonant or nonresonant nonlinear optics', Journal of Physics A: General Physics **5**, 820 (1972).

[53]Y. Wang, 'Nonlinear optical properties of nanometer-sized semiconductor clusters', Accounts of Chemical Research **24**, 133–139 (1991).

[54]D. Hall, M. A. Newhouse, N. F. Borrelli, W. H. Dumbaugh and D. Weidman, 'Nonlinear optical susceptibilities of high-index glasses', Applied Physics Letters **54**, 1293–1295 (1989).

[55]D. Ricard, P. Roussignol and C. Flytzanis, 'Surface-mediated enhancement of optical phase conjugation in metal colloids', Optics letters **10**, 511–513 (1985).

[56]R. W. Boyd, Z. Shi and I. De Leon, 'The third-order nonlinear optical susceptibility of gold', Optics Communications **326**, 74–79 (2014).

[57]L. Caspani, R. Kaipurath, M. Clerici, M. Ferrera, T. Roger, J Kim, N. Kinsey, M. Pietrzyk, A. Di Falco, V. M. Shalaev et al., 'Enhanced nonlinear refractive index in ε-near-zero materials', Physical review letters **116**, 233901 (2016).

[58]S. Campione, D. de Ceglia, M. A. Vincenti, M. Scalora and F. Capolino, 'Electric field enhancement in -near-zero slabs under tm-polarized oblique incidence', Physical Review B **87**, 035120 (2013).

[59]A. Ciattoni, C. Rizza and E. Palange, 'Transmissivity directional hysteresis of a nonlinear metamaterial slab with very small linear permittivity', Optics letters **35**, 2130–2132 (2010).

[60]M. Vincenti, D De Ceglia, A Ciattoni and M Scalora, 'Singularity-driven second-and third-harmonic generation at ε-near-zero crossing points', Physical Review A **84**, 063826 (2011).

[61]A Ciattoni and E Spinozzi, 'Efficient second-harmonic generation in micrometer-thick slabs with indefinite permittivity', Physical Review A **85**, 043806 (2012).

[62]Y. Wang, A. Capretti and L. Dal Negro, 'Wide tuning of the optical and structural properties of alternative plasmonic materials', Optical Materials Express **5**, 2415–2430 (2015).

[63]T. V. Shahbazyan and M. I. Stockman, *Plasmonics: theory and applications* (Springer, 2013).

[64]R. Kaipurath, M. Pietrzyk, L Caspani, T Roger, M Clerici, C Rizza, A Ciattoni, A. Di Falco and D Faccio, 'Optically induced metal-to-dielectric transition in epsilon-near-zero metamaterials', Scientific reports **6**, 27700 (2016).

[65]A. R. Davoyan, A. M. Mahmoud and N. Engheta, 'Optical isolation with epsilon-near-zero metamaterials', Optics Express **21**, 3279–3286 (2013).

[66]A. Ciesielski, L. Skowronski, M. Trzcinski and T. Szoplik, 'Controlling the optical parameters of self-assembled silver films with wetting layers and annealing', Applied Surface Science **421**, 349–356 (2017).

[67]I. Malitson, 'Interspecimen comparison of the refractive index of fused silica', Josa **55**, 1205–1209 (1965).

[68]H. H. Sheinfux, I. Kaminer, Y. Plotnik, G. Bartal and M. Segev, 'Subwavelength multilayer dielectrics: ultrasensitive transmission and breakdown of effective-medium theory', Physical review letters **113**, 243901 (2014).

[69]O. Kidwai, S. V. Zhukovsky and J. Sipe, 'Effective-medium approach to planar multilayer hyperbolic metamaterials: strengths and limitations', Physical Review A **85**, 053842 (2012).

[70]F. Forstmann and R. R. Gerhardts, *Metal optics near the plasma frequency*, Vol. 109 (Springer, 2006).

[71]D. S. Ginley and C. Bright, 'Transparent conducting oxides', MRS bulletin **25**, 15–18 (2000).

[72]T. Taubner, D. Korobkin, Y. Urzhumov, G. Shvets and R. Hillenbrand, 'Near-field microscopy through a sic superlens', Science **313**, 1595–1595 (2006).

[73]Z. Lu, W. Zhao and K. Shi, 'Ultracompact electroabsorption modulators based on tunable epsilon-near-zero-slot waveguides', IEEE Photonics Journal **4**, 735–740 (2012).

[74]S. Ishii, A. V. Kildishev, E. Narimanov, V. M. Shalaev and V. P. Drachev, 'Sub-wavelength interference pattern from volume plasmon polaritons in a hyperbolic medium', Laser & Photonics Reviews **7**, 265–271 (2013).

[75]A. Poddubny, I. Iorsh, P. Belov and Y. Kivshar, 'Hyperbolic metamaterials', Nature photonics **7**, 948 (2013).

[76]V. P. Drachev, V. A. Podolskiy and A. V. Kildishev, 'Hyperbolic metamaterials: new physics behind a classical problem', Optics express **21**, 15048–15064 (2013).

[77]Z. Liu, H. Lee, Y. Xiong, C. Sun and X. Zhang, 'Far-field optical hyperlens magnifying sub-diffraction-limited objects', science **315**, 1686–1686 (2007).

[78]I. I. Smolyaninov, Y.-J. Hung and C. C. Davis, 'Magnifying superlens in the visible frequency range', science **315**, 1699–1701 (2007).

[79]L. Verslegers, P. B. Catrysse, Z. Yu and S. Fan, 'Deep-subwavelength focusing and steering of light in an aperiodic metallic waveguide array', Physical review letters **103**, 033902 (2009).

[80]M. Born and E. Wolf, *Principles of optics: electromagnetic theory of propagation, interference and diffraction of light* (Elsevier, 2013).

[81]C. Pfeiffer, C. Zhang, V. Ray, L. J. Guo and A. Grbic, 'High performance bianisotropic metasurface: asymmetric transmission of light', Physical review letters **113**, 023902 (2014).

[82]A Papakostas, A Potts, D. Bagnall, S. Prosvirnin, H. Coles and N. Zheludev, 'Optical manifestations of planar chirality', Physical review letters **90**, 107404 (2003).

[83]L Jelinek, R Marqués, F Mesa and J. Baena, 'Periodic arrangements of chiral scatterers providing negative refractive index bi-isotropic media', Physical Review B **77**, 205110 (2008).

[84]A Ciattoni, C Rizza and E. Palange, 'Extreme nonlinear electrodynamics in metamaterials with very small linear dielectric permittivity', Physical Review A **81**, 043839 (2010).

[85]C. Argyropoulos, P.-Y. Chen, G. D'Aguanno, N. Engheta and A. Alu, 'Boosting optical nonlinearities in ε-near-zero plasmonic channels', Physical Review B **85**, 045129 (2012).

[86]R. Pollard, A Murphy, W. Hendren, P. Evans, R Atkinson, G. Wurtz, A. Zayats and V. A. Podolskiy, 'Optical nonlocalities and additional waves in epsilon-near-zero metamaterials', Physical review letters **102**, 127405 (2009).

[87]A Ciattoni and E Spinozzi, 'Optical resonances and angular filtering functionality of subwavelength hyperbolic etalons', Optik-International Journal for Light and Electron Optics **124**, 3623–3626 (2013).

[88]C. Menzel, C. Rockstuhl and F. Lederer, 'Advanced jones calculus for the classification of periodic metamaterials', Physical Review A **82**, 053811 (2010).

[89]C. Rizza, X. Li, A. Di Falco, E. Palange, A. Marini and A. Ciattoni, 'Enhanced asymmetric transmission in hyperbolic epsilon-near-zero slabs', Journal of Optics **20**, 085001 (2018).

[90]M. Moharam, E. B. Grann, D. A. Pommet and T. Gaylord, 'Formulation for stable and efficient implementation of the rigorous coupled-wave analysis of binary gratings', JOSA a **12**, 1068–1076 (1995).

[91]S. A. Maier, *Plasmonics: fundamentals and applications* (Springer Science & Business Media, 2007).

[92]P. B. Johnson and R.-W. Christy, 'Optical constants of the noble metals', Physical review B **6**, 4370 (1972).

[93]V. P. Drachev, U. K. Chettiar, A. V. Kildishev, H.-K. Yuan, W. Cai and V. M. Shalaev, 'The ag dielectric function in plasmonic metamaterials', Optics express **16**, 1186–1195 (2008).

[94]P. Walley and A. Jonscher, 'Electrical conduction in amorphous germanium', Thin Solid Films **1**, 367–377 (1968).

[95]D. C. Paine, T Whitson, D Janiac, R Beresford, C. O. Yang and B. Lewis, 'A study of low temperature crystallization of amorphous thin film indium–tin–oxide', Journal of Applied Physics **85**, 8445–8450 (1999).

[96]X. Liu, E. Jiang and D. Zhang, 'Electrical transport properties in indium tin oxide films prepared by electron-beam evaporation', Journal of Applied Physics **104**, 073711 (2008).

[97]V. Logeeswaran, N. P. Kobayashi, M. S. Islam, W. Wu, P. Chaturvedi, N. X. Fang, S. Y. Wang and R. S. Williams, 'Ultrasmooth silver thin films deposited with a germanium nucleation layer', Nano letters **9**, 178–182 (2008).

[98]W. Chen, M. D. Thoreson, S. Ishii, A. V. Kildishev and V. M. Shalaev, 'Ultra-thin ultra-smooth and low-loss silver films on a germanium wetting layer', Optics express **18**, 5124–5134 (2010).

[99]A Hilger, M Tenfelde and U Kreibig, 'Silver nanoparticles deposited on dielectric surfaces', Applied Physics B **73**, 361–372 (2001).

[100]V. M. Shalaev, *Optical properties of nanostructured random media*, Vol. 82 (Springer Science & Business Media, 2002).

[101]L. Gao, F Lemarchand and M Lequime, 'Refractive index determination of sio2 layer in the uv/vis/nir range: spectrophotometric reverse engineering on single and bi-layer designs', Journal of the European Optical Society-Rapid publications **8** (2013).

[102]A. P. Alivisatos, 'Semiconductor clusters, nanocrystals, and quantum dots', science **271**, 933–937 (1996).

[103]J. H. Davies, *The physics of low-dimensional semiconductors: an introduction* (Cambridge university press, 1998).

[104]F. Koyama, 'Recent advances of vcsel photonics', Journal of Lightwave Technology **24**, 4502–4513 (2006).

[105]P. Harrison and A. Valavanis, *Quantum wells, wires and dots: theoretical and computational physics of semiconductor nanostructures* (John Wiley & Sons, 2016).

[106]P Michler, A Kiraz, C Becher, W. Schoenfeld, P. Petroff, L. Zhang, E Hu and A Imamoglu, 'A quantum dot single-photon turnstile device', science **290**, 2282–2285 (2000).

[107]J. P. Reithmaier, 'Strong exciton–photon coupling in semiconductor quantum dot systems', Semiconductor Science and Technology **23**, 123001 (2008).

[108]Y. Yu, X.-M. Dou, B. Wei, G.-W. Zha, X.-J. Shang, L. Wang, D. Su, J.-X. Xu, H.-Y. Wang, H.-Q. Ni et al., 'Self-assembled quantum dot structures in a hexagonal nanowire for quantum photonics', Advanced Materials **26**, 2710–2717 (2014).

[109]H. J. Fan, P. Werner and M. Zacharias, 'Semiconductor nanowires: from self-organization to patterned growth', small **2**, 700–717 (2006).

[110]S. I. Bozhevolnyi and N. A. Mortensen, 'Plasmonics for emerging quantum technologies', Nanophotonics **6**, 1185–1188 (2017).

[111]R. Wagner and W. Ellis, 'Vapor-liquid-solid mechanism of single crystal growth', Applied Physics Letters **4**, 89–90 (1964).

[112]K. A. Dick, S. Kodambaka, M. C. Reuter, K. Deppert, L. Samuelson, W. Seifert, L. R. Wallenberg and F. M. Ross, 'The morphology of axial and branched nanowire heterostructures', Nano letters **7**, 1817–1822 (2007).

[113]A. Taflove and S. C. Hagness, *Computational electrodynamics: the finite-difference time-domain method* (Artech house, 2005).

[114]H. Philipp and E. D. Palik, 'Handbook of optical constants of solids', Palik (Ed.)(Academic, Orlando 1985) p **749**, 74 (1985).

[115]D. Burge, H. Bennett and E. Ashley, 'Effect of atmospheric exposure on the infrared reflectance of silvered mirrors with and without protective coatings', Applied optics **12**, 42–47 (1973).

[116]A O'hara, J. Hannah, I Underwood, D. G. Vass and R. Holwill, 'Mirror quality and efficiency improvements of reflective spatial light modulators by the use of dielectric coatings and chemical-mechanical polishing', Applied Optics **32**, 5549–5556 (1993).

[117]B. Soffer and B. McFarland, 'Continuously tunable, narrow-band organic dye lasers', Applied physics letters **10**, 266–267 (1967).

[118]J. L. Chilla, S. D. Butterworth, A. Zeitschel, J. P. Charles, A. L. Caprara, M. K. Reed and L. Spinelli, 'High-power optically pumped semiconductor lasers', in Solid state lasers xiii: technology and devices, Vol. 5332 (International Society for Optics and Photonics, 2004), pp. 143–151.

[119]J. Clark and G. Lanzani, 'Organic photonics for communications', Nature photonics **4**, 438 (2010).

[120]S. Liu, Y. Wei, R. Su, R. Su, B. Ma, Z. Chen, H. Ni, Z. Niu, Y. Yu, Y. Wei et al., 'A deterministic quantum dot micropillar single photon source with> 65% extraction efficiency based on fluorescence imaging method', Scientific Reports **7**, 13986 (2017).

[121]D. Schurig, J. Mock, B. Justice, S. A. Cummer, J. B. Pendry, A. Starr and D. Smith, 'Metamaterial electromagnetic cloak at microwave frequencies', Science **314**, 977–980 (2006).

[122]J. Hao, W. Yan and M. Qiu, 'Super-reflection and cloaking based on zero index metamaterial', Applied Physics Letters **96**, 101109 (2010).

[123]J. B. Pendry, 'Negative refraction makes a perfect lens', Physical review letters **85**, 3966 (2000).

[124]R. B. Nielsen, M. D. Thoreson, W. Chen, A. Kristensen, J. M. Hvam, V. Shalaev and A. Boltasseva, 'Toward superlensing with metal–dielectric composites and multilayers', Applied Physics B **100**, 93–100 (2010).

[125]Y. C. Jun, J. Reno, T. Ribaudo, E. Shaner, J.-J. Greffet, S. Vassant, F. Marquier, M. Sinclair and I. Brener, 'Epsilon-near-zero strong coupling in metamaterial-semiconductor hybrid structures', Nano letters **13**, 5391–5396 (2013).

[126]A. Capretti, Y. Wang, N. Engheta and L. Dal Negro, 'Enhanced third-harmonic generation in si-compatible epsilon-near-zero indium tin oxide nanolayers', Optics letters **40**, 1500–1503 (2015).

[127]A. Di Falco, M. Ploschner and T. F. Krauss, 'Flexible metamaterials at visible wavelengths', New Journal of Physics **12**, 113006 (2010).

[128]S. Walia, C. M. Shah, P. Gutruf, H. Nili, D. R. Chowdhury, W. Withayachumnankul, M. Bhaskaran and S. Sriram, 'Flexible metasurfaces and metamaterials: a review of materials and fabrication processes at micro-and nano-scales', Applied Physics Reviews **2**, 011303 (2015).

[129]S. M. Kamali, A. Arbabi, E. Arbabi, Y. Horie and A. Faraon, 'Decoupling optical function and geometrical form using conformal flexible dielectric metasurfaces', Nature communications **7**, 11618 (2016).

[130]J. Burch, D. Wen, X. Chen and A. D. Falco, 'Conformable holographic metasurfaces', Scientific Reports **7**, 4520 (2017).

[131]J. Burch and A. D. Falco, 'Surface topology specific metasurface holograms', Acs Photonics **5**, acsphotonics.7b01449 (2018).

[132]G. X. Li, S. M. Chen, W. H. Wong, E. Y. Pun and K. W. Cheah, 'Highly flexible near-infrared metamaterials', Optics Express **20**, 397–402 (2012).

[133]A. D. Falco, A. Ricciardi, P. Readerharris and T. Krauss, 'Optical guided mode resonance filter on a flexible substrate', Optics Express **21**, 1002–1007 (2013).

[134]P. Readerharris and A. D. Falco, 'Nanoplasmonic filters for hollow core photonic crystal fibers', Acs Photonics **1**, 985–989 (2014).

[135]G. Bo, M. M. F. Yuen and T. T. Ye, 'Flexible frequency selective metamaterials for microwave applications', Scientific Reports **7**, 45108 (2017).

[136]H. I. Lin, K. C. Shen, S. Y. Lin, G. Haider, Y. H. Li, S. W. Chang and Y. F. Chen, 'Transient and flexible hyperbolic metamaterials on freeform surfaces.', Scientific Reports **8**, 9469– (2018).

[137]T. Sum, A. Bettiol, J. Van Kan, F Watt, E. Pun and K. Tung, 'Proton beam writing of low-loss polymer optical waveguides', Applied Physics Letters **83**, 1707–1709 (2003).

[138]G. F. Chen, X. Zhao, Y. Sun, C. He, M. C. Tan and D. T. Tan, 'Low loss nanostructured polymers for chip-scale waveguide amplifiers', Scientific Reports **7**, 3366 (2017).

[139]C. Rizza, A. Di Falco and A. Ciattoni, 'Gain assisted nanocomposite multilayers with near zero permittivity modulus at visible frequencies', Applied Physics Letters **99**, 221107 (2011).

[140]T. Tao, J. Ro, J. Melngailis, Z. Xue and H. D. Kaesz, 'Focused ion beam induced deposition of platinum', Journal of Vacuum Science & Technology B: Microelectronics Processing and Phenomena **8**, 1826–1829 (1990).

[141]W. Zhao, K. Shi and Z. Lu, 'Greatly enhanced ultrabroadband light absorption by monolayer graphene.', Optics Letters **38**, 4342–4345 (2013).

[142]K. S. Novoselov, A. K. Geim, S. V. Morozov, D. Jiang, Y. Zhang, S. V. Dubonos, I. V. Grigorieva and A. A. Firsov, 'Electric field effect in atomically thin carbon films', Science **306**, 666–669 (2004).

[143]A. K. Geim, 'Graphene: status and prospects.', Science **324**, 1530–1534 (2009).

[144]M. Liu, X. Yin, E Ulinavila, B. Geng, T Zentgraf, L. Ju, F. Wang and X. Zhang, 'A graphene-based broadband optical modulator.', Nature **474**, 64–67 (2011).

[145]Z. Sun, A. Martinez and F. Wang, 'Optical modulators with 2d layered materials', Nature Photonics **10**, 227 (2016).

[146]Y. C. Chang, C. H. Liu, C. H. Liu, S. Zhang, S. R. Marder, E. E. Narimanov, Z. Zhong and T. B. Norris, 'Realization of mid-infrared graphene hyperbolic metamaterials', Nature Communications **7**, 10568 (2016).

[147]M. A. Othman, C. Guclu and F. Capolino, 'Graphene–dielectric composite metamaterials: evolution from elliptic to hyperbolic wavevector dispersion and the transverse epsilon-near-zero condition', Journal of Nanophotonics **7**, 073089 (2013).

[148]L. Zhang, Z. Zhang, C. Kang, B. Cheng, L. Chen, X. Yang, J. Wang, W. Li and B. Wang, 'Tunable bulk polaritons of graphene-based hyperbolic metamaterials', Optics express **22**, 14022–14030 (2014).

[149]B. Janaszek, A. Tyszka-Zawadzka and P. Szczepański, 'Tunable graphene-based hyperbolic metamaterial operating in sclu telecom bands', Optics express **24**, 24129–24136 (2016).

[150]X. Li, P. Wang, F. Xing, X. D. Chen, Z. B. Liu and J. G. Tian, 'Experimental observation of a giant goos-hanchen shift in graphene using a beam splitter scanning method.', Optics Letters **39**, 5574–5577 (2014).

[151]P. Y. Chen and A. Alù, 'Atomically thin surface cloak using graphene monolayers', Acs Nano **5**, 5855–5863 (2011).

[152]C. Mattevi, H. Kim and M. Chhowalla, 'A review of chemical vapour deposition of graphene on copper', Journal of Materials Chemistry **21**, 3324–3334 (2011).

[153]F. Tuinstra and J. L. Koenig, 'Raman spectrum of graphite', Journal of Chemical Physics **53**, 1126–1130 (1970).

[154]A. C. Ferrari, J. Meyer, V Scardaci, C Casiraghi, M. Lazzeri, F. Mauri, S Piscanec, D. Jiang, K. Novoselov, S Roth et al., 'Raman spectrum of graphene and graphene layers', Physical review letters **97**, 187401 (2006).

[155]M. N. Polyanskiy, *Refractive index database*, `https://refractiveindex.info`, Accessed on 2019-04-26.

[156]R. Ning, S. Liu, H. Zhang, B. Bian and X. Kong, 'Tunable absorption in graphene-based hyperbolic metamaterials for mid-infrared range', Physica B Condensed Matter **457**, 144–148 (2015).

[157]L. A. Falkovsky and A. A. Varlamov, 'Space-time dispersion of graphene conductivity', European Physical Journal B – Condensed Matter **56**, 281–284 (2007).

[158]B. Guo, L. Fang, B. Zhang and J. R. Gong, 'Graphene doping: a review', Insciences J. **1**, 80–89 (2011).

[159]C. Xu, Y. Jin, L. Yang, J. Yang and X. Jiang, 'Characteristics of electro-refractive modulating based on graphene-oxide-silicon waveguide', Optics express **20**, 22398–22405 (2012).

[160]M. Liu, X. Yin, E. Ulin-Avila, B. Geng, T. Zentgraf, L. Ju, F. Wang and X. Zhang, 'A graphene-based broadband optical modulator', Nature **474**, 64 (2011).

[161]Z. Ni, H. Wang, J Kasim, H. Fan, T Yu, Y. Wu, Y. Feng and Z. Shen, 'Graphene thickness determination using reflection and contrast spectroscopy', Nano letters **7**, 2758–2763 (2007).

[162]M. Yi and Z. Shen, 'A review on mechanical exfoliation for the scalable production of graphene', Journal of Materials Chemistry A **3**, 11700–11715 (2015).

[163]S. Stankovich, D. A. Dikin, R. D. Piner, K. A. Kohlhaas, A. Kleinhammes, Y. Jia, Y. Wu, S. T. Nguyen and R. S. Ruoff, 'Synthesis of graphene-based nanosheets via chemical reduction of exfoliated graphite oxide', carbon **45**, 1558–1565 (2007).

[164]S Hagstrom, H. Lyon and G. Somorjai, 'Surface structures on the clean platinum (100) surface', Physical Review Letters **15**, 491 (1965).

[165]A. Morgan and G. Somorjai, 'Low energy electron diffraction studies of gas adsorption on the platinum (100) single crystal surface', Surface Science **12**, 405–425 (1968).

[166]J. C Shelton, H. R Patil and J. M Blakely, 'Equilibrium segregation of carbon to a nickel (111) surface: a surface phase transition', Surface Science **43**, 493–520 (1974).

[167]H. J. Grabke, W. Paulitschke, G. Tauber and H. Viefhaus, 'Equilibrium surface segregation of dissolved nonmetal atoms on iron(100) faces', Surface Science **63**, 377–389 (1977).

[168]A. Reina, X. Jia, J. Ho, D. Nezich, H. Son, V. Bulovic, M. S. Dresselhaus and J. Kong, 'Large area, few-layer graphene films on arbitrary substrates by chemical vapor deposition', Nano Letters **9**, 30–35 (2009).

[169]X. Li, W. Cai, J. An, S. Kim, J. Nah, D. Yang, R. Piner, A. Velamakanni, I. Jung and E. Tutuc, 'Large-area synthesis of high-quality and uniform graphene films on copper foils', Science **324**, 1312–1314 (2009).

[170]S. Chen, W. Cai, R. D. Piner, J. W. Suk, Y. Wu, Y. Ren, J. Kang and R. S. Ruoff, 'Synthesis and characterization of large-area graphene and graphite films on commercial cu-ni alloy foils.', Nano Letters **11**, 3519 (2011).

[171]A. Mohsin, L. Liu, P. Liu, W. Deng, I. N. I. §, G. Li, O. E. Dyck, G. Duscher, J. R. Dunlap and X. Kai, 'Synthesis of millimeter-size hexagon-shaped graphene single crystals on resolidified copper', Acs Nano **7**, 8924–8931 (2013).

[172]S. Chen, H. Ji, H Chou, Q. Li, H. Li, J. W. Suk, R Piner, L. Liao, W. Cai and R. S. Ruoff, 'Millimeter-size single-crystal graphene by suppressing evaporative loss of cu during low pressure chemical vapor deposition', Advanced Materials **25**, 2062–2065 (2013).

[173]X. Wang, H. You, F. Liu, M. Li, L. Wan, S. Li, Q. Li, Y. Xu, R. Tian, Z. Yu et al., 'Large-scale synthesis of few-layered graphene using cvd', Chemical Vapor Deposition **15**, 53–56 (2009).

[174]S. Bae, H. Kim, Y. Lee, X. Xu, J. S. Park, Y. Zheng, J. Balakrishnan, T. Lei, H. R. Kim and Y. I. Song, 'Roll-to-roll production of 30-inch graphene films for transparent electrodes', Nature Nanotechnology **5**, 574–578 (2010).

[175]J. Kang, S. Hwang, J. H. Kim, H. K. Min, J. Ryu, J. S. Sang, B. H. Hong, M. K. Kim and J. B. Choi, 'Efficient transfer of large-area graphene films onto rigid substrates by hot pressing', Acs Nano **6**, 5360–5365 (2012).

[176]A. Reina, H. Son, L. Jiao, B. Fan, M. S. Dresselhaus, Z. F. Liu and J. Kong, 'Transferring and identification of single- and few-layer graphene on arbitrary substrates', Journal of Physical Chemistry C **112**, 17741–17744 (2008).

[177]X. Li, Y. Zhu, W. Cai, M Borysiak, B. Han, D. Chen, R. D. Piner, L Colombo and R. S. Ruoff, 'Transfer of large-area graphene films for high-performance transparent conductive electrodes', Nano Letters **9**, 4359 (2009).

[178]CHEN, XuDong, LIU, ZhiBo, ZHENG, ChaoYi, F. Xing, YAN, XiaoQing and Y. Chen, 'High-quality and efficient transfer of large-area graphene films onto different substrates', Carbon **56**, 271–278 (2013).

[179]X. Liang, B. A. Sperling, I Calizo, G. Cheng, C. A. Hacker, Q. Zhang, Y Obeng, K. Yan, H. Peng and Q. Li, 'Toward clean and crackless transfer of graphene.', Acs Nano **5**, 9144–9153 (2011).

[180]D. Bodas and C. Khan-Malek, 'Formation of more stable hydrophilic surfaces of pdms by plasma and chemical treatments', Microelectronic Engineering **83**, 1277–1279 (2006).

[181]R. Heyrovska, 'Atomic structures of graphene, benzene and methane with bond lengths as sums of the single, double and resonance bond radii of carbon', arXiv preprint arXiv:0804.4086 (2008).

[182]T. L. Burnett, R. Yakimova and O. Kazakova, 'Identification of epitaxial graphene domains and adsorbed species in ambient conditions using quantified topography measurements', Journal of Applied Physics **112**, 054308 (2012).

[183]H. Jussila, H. Yang, N. Granqvist and Z. Sun, 'Surface plasmon resonance for characterization of large-area atomic-layer graphene film', Optica **3**, 151–158 (2016).

[184]D. Graf, F. Molitor, K. Ensslin, C. Stampfer, A. Jungen, C. Hierold and L. Wirtz, 'Spatially resolved raman spectroscopy of single-and few-layer graphene', Nano letters **7**, 238–242 (2007).

[185]Y. K. Koh, M. H. Bae, D. G. Cahill and E Pop, 'Reliably counting atomic planes of few-layer graphene (n > 4)', Acs Nano **5**, 269–74 (2011).

[186]Z.-S. Wu, W. Ren, L. Gao, B. Liu, C. Jiang and H.-M. Cheng, 'Synthesis of high-quality graphene with a pre-determined number of layers', Carbon **47**, 493–499 (2009).

[187]J. M. Dawlaty, S. Shivaraman, J. Strait, P. George, M. Chandrashekhar, F. Rana, M. G. Spencer, D. Veksler and Y. Chen, 'Measurement of the optical absorption spectra of epitaxial graphene from terahertz to visible', Applied Physics Letters **93**, 131905 (2008).

[188]D. J. Gardiner and P. R. Graves, *Practical raman spectroscopy* (1989).

[189]P. Vandenabeele, 'Practical raman spectroscopy - an introduction', Materials & Manufacturing Processes **29** (2013).

[190]N. Colthup, *Introduction to infrared and raman spectroscopy* (Elsevier, 2012).

[191]L. M. Malard, M. A. Pimenta, G. Dresselhaus and M. S. Dresselhaus, 'Raman spectroscopy in graphene', Physics Reports **473**, 51–87 (2009).

[192]W. Yan, D. C. Alsmeyer and R. L. Mccreery, 'Raman spectroscopy of carbon materials: structural basis of observed spectra', Chemistry of Materials **2**, 557–563 (2002).

[193]J. Seo, J. Lee, A.-R. Jang, Y. Choi, U. Kim, H. S. Shin and H. Park, 'Study of cooling rate on the growth of graphene via chemical vapor deposition', Chemistry of Materials **29**, 4202–4208 (2017).

[194]S De and J. N. Coleman, 'Are there fundamental limitations on the sheet resistance and transmittance of thin graphene films?', Acs Nano **4**, 2713–2720 (2010).

[195]M. Kolle, B. Zheng, N. Gibbons, J. J. Baumberg and U. Steiner, 'Stretch-tuneable dielectric mirrors and optical microcavities', Optics express **18**, 4356–4364 (2010).

[196]B. Tatian, 'Fitting refractive-index data with the sellmeier dispersion formula', Applied Optics **23**, 4477 (1984).

[197]D. Chandler-Horowitz and P. M. Amirtharaj, 'High-accuracy, midinfrared (450 cm-1<=<=4000 cm-1) refractive index values of silicon', Journal of Applied Physics **97**, 615–211 (2005).

[198]P. Nath, R. F. Bunshah, B. Basol and O. Staffsud, 'Electrical and optical properties of in2o3: sn films prepared by activated reactive evaporation', Thin Solid Films **72**, 463–468 (1980).

[199]S Laux, N Kaiser, A Zöller, R Götzelmann, H Lauth and H Bernitzki, 'Room-temperature deposition of indium tin oxide thin films with plasma ion-assisted evaporation', Thin Solid Films **335**, 1–5 (1998).

[200]T. Maruyama and K. Fukui, 'Indium-tin oxide thin films prepared by chemical vapor deposition', Journal of Applied Physics **70**, 3848–3851 (1991).

[201]J.-C. Manifacier, L Szepessy, J. Bresse, M Perotin and R Stuck, 'In2o3:(sn) and sno2:(f) films—application to solar energy conversion; part 1—preparation and characterization', Materials Research Bulletin **14**, 109–119 (1979).

[202]M. Brett, R. McMahon, J Affinito and R. Parsons, 'High rate planar magnetron deposition of transparent, conducting, and heat reflecting films on glass and plastic', Journal of Vacuum Science & Technology A: Vacuum, Surfaces, and Films **1**, 352–355 (1983).

[203]S. Ray, R. Banerjee, N. Basu, A. Batabyal and A. K. Barua, 'Properties of tin doped indium oxide thin films prepared by magnetron sputtering', Journal of Applied Physics **54**, 3497–3501 (1983).

[204]H. C. Lee, J. Y. Seo, Y. W. Choi and D. W. Lee, 'The growth of indium-tin-oxide thin films on glass substrates using dc reactive magnetron sputtering', Vacuum **72**, 269–276 (2003).

[205]J. O. Park, J. H. Lee, J. J. Kim, S. H. Cho and Y. K. Cho, 'Crystallization of indium tin oxide thin films prepared by rf-magnetron sputtering without external heating', Thin Solid Films **474**, 127–132 (2005).

[206]V. Teixeira, H. N Cui, L. J Meng, E. Fortunato and R. Martins, 'Amorphous ito thin films prepared by dc sputtering for electrochromic applications', Thin Solid Films **420-421**, 70–75 (2002).

[207]T Karasawa and Y Miyata, 'Electrical and optical properties of indium tin oxide thin films deposited on unheated substrates by dc reactive sputtering', Thin Solid Films **223**, 135–139 (1993).

[208]H Kim, a. C. Gilmore, A Pique, J. Horwitz, H Mattoussi, H Murata, Z. Kafafi and D. Chrisey, 'Electrical, optical, and structural properties of indium–tin–oxide thin films for organic light-emitting devices', Journal of Applied Physics **86**, 6451–6461 (1999).

[209]Y. S. Jung, D. W. Lee and D. Y. Jeon, 'Influence of dc magnetron sputtering parameters on surface morphology of indium tin oxide thin films', Applied surface science **221**, 136–142 (2004).

[210]P. R. West, S. Ishii, G. V. Naik, N. K. Emani, V. M. Shalaev and A. Boltasseva, 'Searching for better plasmonic materials', Laser & Photonics Reviews **4**, 795–808 (2010).

[211]G. V. Naik, V. M. Shalaev and A. Boltasseva, 'Alternative plasmonic materials: beyond gold and silver', Advanced Materials **25**, 3264–3294 (2013).

[212]Y. Wang, A. C. Overvig, S. Shrestha, R. Zhang, R. Wang, N. Yu and L. Dal Negro, 'Tunability of indium tin oxide materials for mid-infrared plasmonics applications', Optical Materials Express **7**, 2727–2739 (2017).

[213]H. Aouani, M. Rahmani, M. Navarro-Cía and S. A. Maier, 'Third-harmonic-upconversion enhancement from a single semiconductor nanoparticle coupled to a plasmonic antenna', Nature nanotechnology **9**, 290 (2014).

[214]T. S. Luk, D. De Ceglia, S. Liu, G. A. Keeler, R. P. Prasankumar, M. A. Vincenti, M. Scalora, M. B. Sinclair and S. Campione, 'Enhanced third harmonic generation from the epsilon-near-zero modes of ultrathin films', Applied Physics Letters **106**, 151103 (2015).

[215]A. Capretti, Y. Wang, N. Engheta and L. Dal Negro, 'Comparative study of second-harmonic generation from epsilon-near-zero indium tin oxide and titanium nitride nanolayers excited in the near-infrared spectral range', Acs Photonics **2**, 1584–1591 (2015).

[216]M. Z. Alam, I. De Leon and R. W. Boyd, 'Large optical nonlinearity of indium tin oxide in its epsilon-near-zero region', Science **352**, 795–797 (2016).

[217]N. Yu and Z. Gaburro, 'Light propagation with phase discontinuities: generalized laws of reflection and refraction', Science **334**, 333–337 (2011).

[218]D. Lin, P. Fan, E Hasman and M. L. Brongersma, 'Dielectric gradient metasurface optical elements.', Science **345**, 298–302 (2016).

[219]S. A. Schulz, J. Upham, F. Bouchard, I. De Leon, E. Karimi and R. W. Boyd, 'Quantifying the impact of proximity error correction on plasmonic metasurfaces', Optical Materials Express **5**, 2798–2803 (2015).

[220]S. A. Schulz, A. A. Tahir, M. Z. Alam, J. Upham, I. D. Leon and R. W. Boyd, 'Optical response of dipole antennas on an epsilon-near-zero substrate', Phys.rev.a **93**, 063846 (2016).

[221]W. Van Dorp and C. W. Hagen, 'A critical literature review of focused electron beam induced deposition', Journal of Applied Physics **104**, 10 (2008).

[222]F De Angelis, C Liberale, M. Coluccio, G Cojoc and E Di Fabrizio, 'Emerging fabrication techniques for 3d nano-structuring in plasmonics and single molecule studies', Nanoscale **3**, 2689–2696 (2011).

[223]M. D. Turner, M. Saba, Q. Zhang, B. P. Cumming, G. E. Schröder-Turk and M. Gu, 'Miniature chiral beamsplitter based on gyroid photonic crystals', Nature Photonics **7**, 801 (2013).

[224]M. Esposito, V. Tasco, F. Todisco, M. Cuscunà, A. Benedetti, D. Sanvitto and A. Passaseo, 'Triple-helical nanowires by tomographic rotatory growth for chiral photonics', Nature communications **6**, 6484 (2015).

[225]J. K. Gansel, M. Wegener, S. Burger and S. Linden, 'Gold helix photonic metamaterials: a numerical parameter study', Optics express **18**, 1059–1069 (2010).

[226]V. Tasco, M. Esposito, F. Todisco, A. Benedetti, M. Cuscunà, D. Sanvitto and A. Passaseo, 'Three-dimensional nanohelices for chiral photonics', Applied Physics A **122**, 280 (2016).

[227]M. Esposito, V. Tasco, F. Todisco, A. Benedetti, D. Sanvitto and A. Passaseo, 'Chirality: three dimensional chiral metamaterial nanospirals in the visible range by vertically compensated focused ion beam induced-deposition (advanced optical materials 2/2014)', Advanced Optical Materials **2**, 198–198 (2014).

[228]V. Sandoghdar, F Treussart, J Hare, V Lefevre-Seguin, J.-M. Raimond and S Haroche, 'Very low threshold whispering-gallery-mode microsphere laser', Physical review A **54**, R1777 (1996).

[229]S Arnold, M Khoshsima, I Teraoka, S Holler and F Vollmer, 'Shift of whispering-gallery modes in microspheres by protein adsorption', Optics letters **28**, 272–274 (2003).

[230]K. Hennessy, A. Badolato, M Winger, D Gerace, M. Atatüre, S Gulde, S Fält, E. L. Hu and A Imamoğlu, 'Quantum nature of a strongly coupled single quantum dot–cavity system', Nature **445**, 896 (2007).

[231]P. Anger, P. Bharadwaj and L. Novotny, 'Enhancement and quenching of single-molecule fluorescence', Physical review letters **96**, 113002 (2006).

[232]T. B. Hoang, G. M. Akselrod and M. H. Mikkelsen, 'Ultrafast room-temperature single photon emission from quantum dots coupled to plasmonic nanocavities', Nano letters **16**, 270–275 (2015).

[233]R. Chikkaraddy, B. de Nijs, F. Benz, S. J. Barrow, O. A. Scherman, E. Rosta, A. Demetriadou, P. Fox, O. Hess and J. J. Baumberg, 'Single-molecule strong coupling at room temperature in plasmonic nanocavities', Nature **535**, 127 (2016).

[234]J. Claudon, J. Bleuse, N. S. Malik, M. Bazin, P. Jaffrennou, N. Gregersen, C. Sauvan, P. Lalanne and J.-M. Gérard, 'A highly efficient single-photon source based on a quantum dot in a photonic nanowire', Nature Photonics **4**, 174 (2010).

[235]A Löffler, J. Reithmaier, G Sęk, C Hofmann, S Reitzenstein, M Kamp and A Forchel, 'Semiconductor quantum dot microcavity pillars with high-quality factors and enlarged dot dimensions', Applied Physics Letters **86**, 111105 (2005).

[236]J. P. Reithmaier, G Sęk, A Löffler, C Hofmann, S Kuhn, S Reitzenstein, L. Keldysh, V. Kulakovskii, T. Reinecke and A Forchel, 'Strong coupling in a single quantum dot–semiconductor microcavity system', Nature **432**, 197 (2004).

[237]D. Press, S. Götzinger, S. Reitzenstein, C. Hofmann, A. Löffler, M. Kamp, A. Forchel and Y. Yamamoto, 'Photon antibunching from a single quantum-dot-microcavity system in the strong coupling regime', Physical Review Letters **98**, 117402 (2007).

[238]M. S. Tame, K. McEnery, Ş. Özdemir, J Lee, S. Maier and M. Kim, 'Quantum plasmonics', Nature Physics **9**, 329 (2013).

[239]R. Stomp, Y. Miyahara, S. Schaer, Q. Sun, H. Guo, P. Grutter, S. Studenikin, P. Poole and A. Sachrajda, 'Detection of single-electron charging in an individual inas quantum dot by noncontact atomic-force microscopy', Physical review letters **94**, 056802 (2005).

[240]L. Sapienza, J. Liu, J. D. Song, S. Fält, W. Wegscheider, A. Badolato and K. Srinivasan, 'Combined atomic force microscopy and photoluminescence imaging to select single inas/gaas quantum dots for quantum photonic devices', Scientific Reports **7**, 6205 (2017).

[241]J.-H. Song, T. Atay, S. Shi, H. Urabe and A. V. Nurmikko, 'Large enhancement of fluorescence efficiency from cdse/zns quantum dots induced by resonant coupling to spatially controlled surface plasmons', Nano letters **5**, 1557–1561 (2005).

[242]P. Pompa, L Martiradonna, A Della Torre, F Della Sala, L Manna, M De Vittorio, F Calabi, R Cingolani and R Rinaldi, 'Metal-enhanced fluorescence of colloidal nanocrystals with nanoscale control', Nature nanotechnology **1**, 126 (2006).

[243]S. Strauf, N. G. Stoltz, M. T. Rakher, L. A. Coldren, P. M. Petroff and D. Bouwmeester, 'High-frequency single-photon source with polarization control', Nature photonics **1**, 704 (2007).

[244]A. W. Schell, H. Takashima, T. T. Tran, I. Aharonovich and S. Takeuchi, 'Coupling quantum emitters in 2d materials with tapered fibers', ACS Photonics **4**, 761–767 (2017).

[245]O. Kulakovich, N. Strekal, A. Yaroshevich, S. Maskevich, S. Gaponenko, I. Nabiev, U. Woggon and M. Artemyev, 'Enhanced luminescence of cdse quantum dots on gold colloids', Nano Letters **2**, 1449–1452 (2002).

[246]Y.-P. Hsieh, C.-T. Liang, Y.-F. Chen, C.-W. Lai and P.-T. Chou, 'Mechanism of giant enhancement of light emission from au/cdse nanocomposites', Nanotechnology **18**, 415707 (2007).

[247]D. Pires, J. L. Hedrick, A. De Silva, J. Frommer, B. Gotsmann, H. Wolf, M. Despont, U. Duerig and A. W. Knoll, 'Nanoscale three-dimensional patterning of molecular resists by scanning probes', Science, 1187851 (2010).

[248]A. Akimov, A Mukherjee, C. Yu, D. Chang, A. Zibrov, P. Hemmer, H Park and M. Lukin, 'Generation of single optical plasmons in metallic nanowires coupled to quantum dots', Nature **450**, 402 (2007).

[249]Z. Li, K. Bao, Y. Fang, Y. Huang, P. Nordlander and H. Xu, 'Correlation between incident and emission polarization in nanowire surface plasmon waveguides', Nano letters **10**, 1831–1835 (2010).

[250]M. Esposito, V. Tasco, M. Cuscuna, F. Todisco, A. Benedetti, I. Tarantini, M. D. Giorgi, D. Sanvitto and A. Passaseo, 'Nanoscale 3d chiral plasmonic helices with circular dichroism at visible frequencies', ACS Photonics **2**, 105–114 (2014).

[251]S. Frabboni, G. Gazzadi, L Felisari and A Spessot, 'Fabrication by electron beam induced deposition and transmission electron microscopic characterization of sub-10-nm freestanding pt nanowires', Applied physics letters **88**, 213116 (2006).

[252]G. Seniutinas, A. Balčytis, I. Reklaitis, F. Chen, J. Davis, C. David and S. Juodkazis, 'Tipping solutions: emerging 3d nano-fabrication/-imaging technologies', Nanophotonics **6**, 923–941 (2017).

[253]R. Yan, D. Gargas and P. Yang, 'Nanowire photonics', Nature photonics **3**, 569 (2009).

[254]S. Cao, X. Ji, K. Qiu, Y. Gao, Y. Zhao, J. Tang, Z. Xu, K. Jin and X. Xu, 'Resolving exciton diffusion in ingaas quantum wells using micro-photoluminescence mapping with a lateral excitation', Semiconductor Science and Technology **28**, 125004 (2013).

[255]J. Wang, Y. Yu, Y.-M. Wei, S.-F. Liu, J. Li, Z.-K. Zhou, Z.-C. Niu, S.-Y. Yu and X.-H. Wang, 'High-efficiency broadband second harmonic generation in single hexagonal gaas nanowire', Scientific reports **7**, 2166 (2017).

[256]X. Li, R.-L. Su, Z.-K. Zhou, Y. Yu and A. Di Falco, 'Photonic trimming of quantum emitters via direct fabrication of metallic nanofeatures', APL Photonics **3**, 071301 (2018).

[257]M. Pfeiffer, K. Lindfors, P. Atkinson, A. Rastelli, O. G. Schmidt, H. Giessen and M. Lippitz, 'Positioning plasmonic nanostructures on single quantum emitters', physica status solidi (b) **249**, 678–686 (2012).

[258]M Heiss, Y Fontana, A. Gustafsson, G Wüst, C Magen, D. O'regan, J. Luo, B Ketterer, S Conesa-Boj, A. Kuhlmann et al., 'Self-assembled quantum dots in a nanowire system for quantum photonics', Nature materials **12**, 439 (2013).

[259]J. A. Alanis, D. Saxena, S. Mokkapati, N. Jiang, K. Peng, X. Tang, L. Fu, H. H. Tan, C. Jagadish and P. Parkinson, 'Large-scale statistics for threshold optimization of optically pumped nanowire lasers', Nano letters **17**, 4860–4865 (2017).

[260]G. Juska, E Murray, V. Dimastrodonato, T.-H. Chung, S. T. Moroni, A Gocalinska and E. Pelucchi, 'Conditions for entangled photon emission from (111) b site-controlled pyramidal quantum dots', Journal of Applied Physics **117**, 134302 (2015).

[261]T. Chung, G Juska, S. Moroni, A Pescaglini, A Gocalinska and E Pelucchi, 'Selective carrier injection into patterned arrays of pyramidal quantum dots for entangled photon light-emitting diodes', Nature Photonics **10**, 782 (2016).

List of Figures

List of Tables

Acronyms and Initialisms

0D zero-dimensional. 45

1D one-dimensional. 2, 5, 12, 18, 19, 22, 45

2D two-dimensional. 2, 7, 10, 11, 18, 22, 44, 69, 151

3D three-dimensional. 7, 22, 107, 108, 128

AENZ anisotropic epsilon-near-zero. 4–7, 10, 15, 17, 18, 21, 25, 151

AFM atomic force microscope. 70, 80, 84, 85, 98, 114, 121, 157

Ag silver. 1, 9, 13, 14, 19, 21, 22, 27–31, 36–42, 45–49, 51, 54, 57–60, 62, 63, 67, 68, 126, 127, 152–155, 161

Al aluminium. 2

Al_2O_3 aluminium oxide. 10

AlGaAs aluminium gallium arsenide. 45, 50–52, 54, 114–116, 121, 124, 154, 159, 160

Ar argon. 74, 75, 82–84, 100–105, 112, 158, 159

Au gold. 1, 27, 87, 88, 94, 95, 114–116, 121, 157, 159

AZO Al-doped zinc oxide. 5, 14

BCs bending cycles. 65, 66, 155

BS beam splitter. 36

BSs beam splitters. 116

C carbon. 107

CH_4 methane. 70, 73–75, 82–84

CO_2 carbon dioxide. 95, 96, 112, 158, 159

Cu copper. 70, 74–79, 82, 156

CVD chemical vapour deposition. 9, 70, 73–76, 82, 83, 98, 99, 156, 161

CW continuous-wave. 52, 116, 117, 119, 160

DC direct current. 99

DI deionised. 77, 79, 90

e-beam electron beam. 9, 26, 28, 51, 54, 55, 58, 59, 68, 87, 92, 93, 126, 152, 157

EBID electron beam induced deposition. 9, 99, 107, 108, 112–115, 121, 122, 124, 126–129, 159, 160

EBL electron beam lithography. 28, 107, 114

EMCCD electron multiplied charge coupled device. 110, 116

EMT effective medium theory. 2–4, 9, 10, 12–14, 22, 25–27, 29, 36, 40, 41, 54, 63, 65, 68, 70, 93, 128, 151, 152

ENZ epsilon-near-zero. 1, 3–12, 14–20, 22–27, 29–33, 37, 40–43, 45–60, 62–73, 92, 94, 98–106, 111, 124, 126–129, 151–156, 158, 161

FDTD Finite-Difference Time-Domain. 45–48, 51, 154

Fe iron. 74

FEB focused electron beam. 28, 107

$FeCl_3$ iron chloride. 77–79, 156

FIB focused ion beam. 67

FlexENZ flexible ENZ membrane. 59–61, 65–68, 155

Ga gallium. 50

GaAs gallium arsenide. 26, 27, 45, 50–52, 54, 114–116, 121, 122, 124, 154, 159, 160

Ge germanium. 27, 29–31, 38–42, 54, 57–59, 62, 68, 76, 152–155

GZO gallium zinc oxide. 5

H_2 hydrogen. 70, 74, 75, 82–84

HF hydrofluoric acid. 50

HfO_2 hafnium dioxide. 57

IBID ion beam-induced deposition. 67, 115

IENZ isotropic epsilon-near-zero. 4, 5, 17, 25

In_2O_3 indium oxide. 14

InGaAs indium gallium arsenide. 114, 121, 124, 160

IPA propan-2-ol. 31, 59, 77, 89, 100, 112

ITO indium tin oxide. 5, 9, 11, 14, 15, 29, 36, 99–113, 124, 126–128, 152, 158, 159, 161

LHCP left-handed circular polarised. 19, 109–111, 159

LPF long-pass filter. 116

MBE molecular beam epitaxy. 45, 50, 114, 121, 154

$MeCpPtMe_3$ methylcyclopentadienyl trimethyl platinum. 115

MM metamaterial. 1, 3, 4, 41, 56, 57, 62, 65–68, 127, 151

MMs metamaterials. 1–8, 10, 15–18, 25, 26, 43, 45, 54–56, 69, 70, 98, 108, 126, 127, 151, 152

MNZ mu-near-zero. 3

MPL micro-photoluminescence. 116

N_2 nitrogen. 77

Ni nickel. 70, 74

NIMs negative-index materials. 2

NIR near-infrared. 1, 5, 9, 11, 15, 36, 103, 105, 106, 111, 126, 127

NW nanowire. 51, 108, 114–116, 118–120, 124, 154, 159, 160

NWs nanowires. 45, 50–54, 114, 115, 117–121, 127, 154, 159, 160

O_2 oxygen. 58, 59, 77, 78, 100–105, 124, 155, 156, 158

OSA optical signal analyser. 103

Pd palladium. 74

PET polyethylene terephthalate. 76–79, 89, 94, 156

PL photoluminescence. 117, 160

PMMA polymethyl methacrylate. 71–73, 76–79, 89–92, 98, 127, 156, 157

Pt platinum. 67, 74, 108, 111–124, 128, 159, 160

QD quantum dot. 47, 52–55, 113, 114, 116–121, 123, 124, 160

QDs quantum dots. 9, 26, 27, 42–45, 48, 50–54, 99, 108, 113–124, 127, 129, 154, 159, 160

RF radio frequency. 9, 99–102, 112, 124, 127, 158

RHCP right-handed circular polarised. 19, 109–111, 159

Rs sheet resistance. 101–103, 124, 158

SEM scanning electron microscope. 29, 30, 51, 59, 66, 67, 80, 108, 109, 113, 115, 116, 121–123, 153–155, 159, 160

Si silicon. 51, 57, 59, 60, 66, 76, 79, 80, 92–98, 108, 114–116, 156–159

SiO_2 silicon dioxide. 9, 13, 14, 27, 28, 31, 36, 37, 39–42, 45–51, 54, 57, 111–116, 122–124, 126, 129, 152–154, 159–161

Sn stannum. 14, 121

SNOM scanning near-field optical microscopy. 129

SPR surface plasmon resonance. 80

TCOs transparent conductive oxides. 5, 9, 11, 14, 99, 126, 151

TiN titanium nitride. 14

TMAH tetramethylammonium hydroxide. 59

TRPL time-resolved photoluminescence. 116, 118

TRT thermal release tape. 76, 77

UV ultraviolet. 14, 59

VLS vapor-liquid-solid. 45

W tungsten. 28, 36, 37, 107–111, 152, 153, 159

$W(CO)_6$ tungsten hexacarbonyl. 107

WGM whispering gallery mode. 111, 124, 128

ZIM zero-index material. 5, 6, 151

ZIMs zero-index materials. 3, 4

ZnSe zinc selenide. 27, 76, 92–95, 97, 98, 127, 128, 157, 158